



# POLITECNICO DI TORINO

DEPARTMENT OF MECHANICAL AND AEROSPACE ENGINEERING

Master of Science program in Mechanical Engineering

Master Thesis

## **Analysis and testing of an alignment monitoring system for PIP-II superconducting cryomodules at Fermilab**

**Supervisor**

Prof. Teresa Maria BERRUTI

**Candidate**

Gianluca BOLOGNA

ACADEMIC YEAR 2022 - 2023



## **Abstract**

Proton Improvement Plan II (PIP-II) is Fermilab's plan to upgrade the particle accelerator complex. The linear accelerator (linac) consists of superconductive cavities, which accelerate the protons, and solenoids, needed to focus the beamline. Cavities and solenoids (also called string assembly) are inserted into a unit called cryomodule (CM). CMs cool and insulate the coldmass assembly from the external environment at room temperature. Superconducting cryomodules use an optical monitoring system to check the alignment of internal components during assembly, testing and operation. This system consists of cameras, known as Boston CCD Angle Monitor "type H" (H-BCAM), and highly reflective targets installed on cavities and solenoids. H-BCAMs track the targets, tracing translations and rotations of the string assembly, which must not exceed design constraints to not affect the cryomodules ability to increase the particles energy. In this thesis, the integration of the H-BCAMs and targets into the prototype High Beta 650 cryomodule (pHB650 CM) is discussed, along with the analysis of the data acquired to monitor the alignment.

H-BCAMs and targets were also used during the test of a Single Spoke Resonator "type 2" cavity (SSR2), which takes place in the Spoke Test Cryostat (STC) facility at Fermilab. The test aims at checking the cavity functionality under nominal working conditions before its insertion into the CM. This contribution presents the integration of the H-BCAMs into the STC, tested for the first time under cryogenic conditions. Thermal and structural analyses were used, with Finite Element Method (FEM), to predict the cavity displacements, and to evaluate the power to supply to two film heaters to ensure that the H-BCAMs would be at room temperature during the test. Furthermore, thermal and structural analyses were performed to assess the behavior of the SSR2 CM.

Results showed that H-BCAMs need a proper installation and calibration to be a reliable instrument to check the alignment of superconductive cryomodules. Further development is needed to improve the cameras measurements for future cryomodules assembly.



# Acknowledgements

I would like to express my deepest appreciation to Professor Berruti and Donato, who gave me this amazing opportunity, and Jacopo, who helped me through these months. Without them, I could not make it on my own.

Special thanks to my American friends, Giorgio, Jamie, Suyash, Nicolò and Nate, who made this experience special. You are incredible people, and I hope I'll see you any time soon.

I would like to greet my friends back at home, Federico, Rosario, Chiara A, Martina and Chiara G and André. Even though it was hard to reach you, you always made me feel your love every time you had the chance.

Finally, thanks to my family for believing in me. You have been a great support even during the rough times.

*Gianluca*



---

# Contents

<b>List of Tables</b>	III
<b>List of Figures</b>	IV
<b>1 Introduction</b>	1
1.1 Fermi National Accelerator Laboratory . . . . .	1
1.2 PIP-II . . . . .	2
1.2.1 Ions source and early stages of acceleration . . . . .	2
1.2.2 Linear Accelerator . . . . .	3
1.3 Importance of the Alignment Monitoring . . . . .	5
<b>2 Optical Alignment Monitoring System</b>	7
2.1 Targets . . . . .	8
2.2 H-BCAM Working Principle . . . . .	9
<b>3 Spoke Test Cryostat</b>	13
3.1 H-BCAMs Stand . . . . .	15
3.1.1 Model and Scope of the Analysis . . . . .	18
3.1.2 Material properties for the Finite Element Analysis . . . . .	19
3.1.3 Steady-State Thermal Analysis . . . . .	20
3.1.4 Static Structural Analysis . . . . .	22
3.1.5 Sensitivity Analysis . . . . .	24
3.1.6 Comparison between experimental test and numerical model . . . . .	27
3.2 SSR2 Cavity . . . . .	30
3.2.1 Model and Scope of the Analysis . . . . .	33
3.2.2 Steady-State Thermal Analysis . . . . .	34
3.2.3 Static Structural Analysis . . . . .	35
3.2.4 Case Study 1: Thermal Load . . . . .	35
3.2.5 Case Study 2: Thermal Load and Bolts Pretension . . . . .	38
<b>4 Single Spoke Resonator "type 2" Cryomodule</b>	41

---

4.1	Model and Scope of the Analysis . . . . .	44
4.2	Steady-State Thermal Analysis . . . . .	45
4.3	Static Structural Analysis . . . . .	47
4.3.1	Case Study 1: Thermal Load . . . . .	48
4.3.2	Case Study 2: Thermal Load and Bolts Pretension . . . . .	50
4.4	Influence of the HTTS . . . . .	50
4.5	Influence of the Helium Flow Rate . . . . .	52
<b>5</b>	<b>Prototype High Beta 650 Cryomodule Data Acquisition</b>	<b>53</b>
5.1	H-BCAMs and Targets Installation . . . . .	54
5.2	MATLAB Script . . . . .	56
5.3	Reference Data Acquisition . . . . .	58
5.4	Insertion Data Acquisition . . . . .	59
5.5	Transport Data Acquisition . . . . .	60
5.6	Pump-down Data Acquisition . . . . .	64
5.7	Cooldown Data Acquisition . . . . .	68
<b>6</b>	<b>Conclusion</b>	<b>74</b>
<b>A</b>	<b>Material Data</b>	<b>76</b>
<b>B</b>	<b>Numerical Results</b>	<b>81</b>
B.1	H-BCAMs Stand - STC . . . . .	81
B.2	SSR2 Cavity - STC . . . . .	83
B.3	SSR2 CM . . . . .	84
<b>C</b>	<b>pHB650 Data Acquisition</b>	<b>90</b>
C.1	Insertion . . . . .	90
C.2	Transport . . . . .	92
C.3	Pump-Down . . . . .	93
C.4	Cooldown . . . . .	94
	<b>Bibliography</b>	<b>VII</b>

---

# List of Tables

1.1	Alignment requirements for an SSR1 CM. . . . .	5
3.1	Friction coefficients . . . . .	18
3.2	Axial preload calculation. . . . .	19
3.3	Emissivity coefficients . . . . .	20
3.4	Static structural analysis results with no heat applied. . . . .	23
3.5	Theoretical vertical displacements of the H-BCAMs stand components.	23
3.6	Comparison between numerical and experimental temperature, sensor 2.	28
3.7	Comparison between numerical and experimental temperature, sensor 3.	29
3.8	Displacements along $x$ , $y$ and $z$ of the points reported in Figure 3.25, case study 1 . . . . .	37
3.9	Theoretical vertical displacements of the SSR2 cavity assembly. . . . .	37
3.10	Displacements along $x$ , $y$ and $z$ of the points reported in Figure 3.25, case study 2. . . . .	38
3.11	Tilting moments about $z$ as a result of the preload applied. . . . .	40
4.1	Beamline displacements of the coldmass assembly, case study 1. . . . .	49
4.2	Theoretical vertical displacements of a cavity inside the SSR2 CM. . . . .	49
4.3	Theoretical vertical displacements of a solenoid inside the SSR2 CM. . . . .	50
4.4	Influence of the HTTS on the vertical displacements of SSR2 cavities. . . . .	51
4.5	Influence of the HTTS on the vertical displacements of SSR2 solenoids. . . . .	51
5.1	Corrections and new vertical displacements of the first six targets of BCAM1. . . . .	63
5.2	Main rotation angles of the HB650 cavities, from upstream to downstream.	73
B.1	Numerical results of the sensitivity analysis. . . . .	82
B.2	Displacements of the couplers external flange, case study 1. . . . .	86
B.3	Target displacements of the string assembly, case study 1. . . . .	87
B.4	Beamline displacements of the coldmass assembly, case study 2. . . . .	88
B.5	Displacements of the couplers external flange, case study 2. . . . .	88
B.6	Target displacements of the string assembly, case study 2. . . . .	89
C.1	Numerical results of the cooldown test. . . . .	95

---

# List of Figures

1.1	Aerial view of the PIP-II complex <sup>11</sup> . . . . .	2
1.2	Half Wave Resonator module installed at Fermilab <sup>12</sup> . . . . .	4
1.3	Prototype SSR1 Cryomodule assembled and tested at Fermilab <sup>12</sup> . . . . .	4
1.4	PIP-II Scheme, from H- Source to booster. . . . .	5
2.1	H-BCAM. The front lens is visible, with two laser diodes on either sides. Above and below the lens are the four LED flashes <sup>13</sup> . . . . .	7
2.2	On the left, the bottom surface of a blue H-BCAM. On the right, its mounting plate with SS316 spheres <sup>13</sup> . . . . .	8
2.3	Target frame assembly with all its components. It is blocked on top of either cavities or solenoids thanks to the bolts and nuts. . . . .	9
2.4	Working principle of a H-BCAM. The length $h$ is proportional to the laser ray angle $\alpha$ . . . . .	10
2.5	Simplified working principle of a H-BCAM in its field of view. . . . .	10
3.1	Spoke Test Cryostat facility at Fermilab <sup>11</sup> . . . . .	13
3.2	STC configuration: SSR2 cavity with targets installed and H-BCAMs stand. . . . .	14
3.3	Internal environment of the STC with the H-BCAMs aluminum stand installed. . . . .	15
3.4	H-BCAMs stand main components description, isometric view. . . . .	16
3.5	H-BCAMs stand main components description, side view. . . . .	16
3.6	Close-up of the stand. Position adjuster, vertical and horizontal adjustable plates are visible. . . . .	17
3.7	Boundary Conditions set for the steady-state thermal analysis. . . . .	21
3.8	Result of the Steady-State Thermal Analysis: H-BCAMs stand temperature distribution. . . . .	21
3.9	Results of the Static Structural Analysis: H-BCAMs stand displacements along $z$ . . . . .	22
3.10	Reference points to evaluate the H-BCAM stand static structural analysis results. . . . .	23
3.11	Film heaters position on the aluminum stand. . . . .	24
3.12	Plot of the vertical displacements as a function of Power and Temperature. . . . .	25

---

3.13	Result of the Steady-State Thermal Analysis: H-BCAMs stand temperature distribution when $P = 18.07$ W is applied. . . . .	26
3.14	Results of the Static Structural Analysis: H-BCAMs stand displacements along $z$ when $P = 18.07$ W is applied. . . . .	26
3.15	Position of the temperature sensors on the aluminum stand for the test held in the STC. . . . .	27
3.16	Comparison between numerical and experimental results. . . . .	28
3.17	Comparison between numerical and experimental results. . . . .	29
3.18	SSR2 Cavity main components, front view. . . . .	30
3.19	SSR2 Cavity main components, isometric view. . . . .	31
3.20	SSR2 Cavity main components, section view. . . . .	31
3.21	SSR2 Cavity, wrapped around MLI, installed inside the STC. . . . .	32
3.22	Boundary Conditions set for the steady-state thermal analysis. . . . .	34
3.23	Results of the Steady-State Thermal Analysis: SSR2 cavity temperature distribution. . . . .	35
3.24	Results of the Static Structural Analysis: SSR2 cavity displacements along $x$ . . . . .	36
3.25	Reference points to evaluate the SSR2 cavity Static Structural analysis results. . . . .	36
3.26	Forces applied along $x$ as a result of the bolts preload. . . . .	39
4.1	SSR2 CM main components description, side view. . . . .	41
4.2	SSR2 CM main components description, front view. . . . .	42
4.3	Boundary Conditions applied for the steady-state thermal analysis. . . . .	46
4.4	HTTS Steady-State Thermal Analysis solution. . . . .	46
4.5	SSR2 CM Steady-State Thermal Analysis solution. . . . .	47
4.6	Results of the Static Structural Analysis: SSR2 displacements along $y$ , isometric view. . . . .	48
4.7	Results of the Static Structural Analysis: SSR2 displacements along $y$ , side view. . . . .	48
4.8	Reference points to evaluate the SSR2 cavity Static Structural analysis results, side view. . . . .	49
4.9	G11 Coefficient of Thermal Expansion, normal direction. . . . .	51
4.10	HTTS Steady-State Thermal Analysis solution, $\dot{m} = 7$ g/s. . . . .	52
5.1	pHB650 CM main components description, side view. . . . .	53
5.2	Insertion of the coldmass assembly into the pHB650 vacuum vessel. . . . .	54
5.3	H-BCAMs and targets installed on the pHB650 string assembly. . . . .	55
5.4	Scheme representing the position and name of both H-BCAMs and targets installed on pHB650. . . . .	55
5.5	View field of H-BCAM1. The first six targets, as well as H-BCAM3 on the opposite side, are clearly visible. . . . .	56
5.6	Data cleaning function working scheme. . . . .	57

---

5.7	On the left, raw data acquired from the H-BCAM. On the right, the same data after the cleaning function has deleted the outliers. . . . .	58
5.8	BCAM3 displacement after the insertion. Acquisition made by BCAM1 with both laser diodes. . . . .	59
5.9	BCAM1 first six targets displacements after the insertion, with both laser diodes. . . . .	60
5.10	Downstream H-BCAMs installed on their permanent plates on pHB650 CM. . . . .	61
5.11	BCAM3 displacement after the transport. . . . .	61
5.12	BCAM1 first six targets displacements after the transport. . . . .	62
5.13	BCAM1 first six targets vertical displacement as a function of their distance from the camera. . . . .	62
5.14	BCAM1 first six targets horizontal displacement as a function of their distance from the camera. . . . .	63
5.15	Corrected vertical displacements of the first twelve targets seen by BCAM1. . . . .	64
5.16	Horizontal displacements of the first twelve targets seen by BCAM1. . . . .	64
5.17	BCAM3 vertical displacement during the pump-down test. . . . .	65
5.18	BCAM1 first twelve vertical displacement during the pump-down test. . . . .	66
5.19	BCAM1 first twelve corrected vertical displacement during the pump-down test. . . . .	67
5.20	BCAM3 horizontal displacement during the pump-down test. . . . .	67
5.21	BCAM1 first twelve vertical displacement during the pump-down test. . . . .	68
5.22	First twelve targets vertical displacement during the cooldown test. . . . .	69
5.23	BCAM4 vertical displacement during the cooldown test. . . . .	70
5.24	BCAM4 horizontal displacement during the cooldown test. . . . .	71
5.25	First twelve targets horizontal displacement during the cooldown test. . . . .	71
5.26	Close up of the HB650 cavities. . . . .	72
A.1	Tightening torque values from F.E.D.S. . . . .	77
A.2	Thermal conductivity Al 6061-T6. . . . .	78
A.3	Young's Modulus Al 6061-T6. . . . .	78
A.4	CTE Al 6061-T6. . . . .	78
A.5	Thermal conductivity Ti Grade 2. . . . .	78
A.6	Young's Modulus Ti Grade 2. . . . .	78
A.7	CTE Ti Grade 2. . . . .	78
A.8	Thermal conductivity Ni RRR300. . . . .	79
A.9	Young's Modulus Ni RRR300. . . . .	79
A.10	CTE Ni RRR300. . . . .	79
A.11	Thermal conductivity PTFE. . . . .	79
A.12	Young's Modulus PTFE. . . . .	79
A.13	CTE PTFE. . . . .	79
A.14	Thermal Conductivity SS 316L. . . . .	80
A.15	Young's Modulus SS 316L. . . . .	80

---

A.16 CTE SS 316L. . . . .	80
A.17 Thermal Conductivity G11. . . . .	80
A.18 CTE SS 316L . . . . .	80
A.19 CTE G11. . . . .	80
B.1 Results of the Static Structural Analysis: H-BCAMs stand displacements along $x$ . . . . .	81
B.2 Results of the Static Structural Analysis: H-BCAMs stand displacements along $y$ . . . . .	82
B.3 Results of the Static Structural Analysis: SSR2 cavity displacements along $y$ . . . . .	83
B.4 Results of the Static Structural Analysis: SSR2 cavity displacements along $z$ . . . . .	83
B.5 Results of the Static Structural Analysis: SSR2 displacements along $x$ , isometric view. . . . .	84
B.6 Results of the Static Structural Analysis: SSR2 displacements along $x$ , top view. . . . .	84
B.7 Results of the Static Structural Analysis: SSR2 displacements along $z$ , isometric view. . . . .	85
B.8 Results of the Static Structural Analysis: SSR2 displacements along $z$ , side view. . . . .	85
B.9 Reference points to evaluate the SSR2 cavity Static Structural analysis results, isometric view. . . . .	86
C.1 Insertion: displacement of T1-T6 BCAM2. . . . .	90
C.2 Insertion: displacement of T1-T6 BCAM3. . . . .	91
C.3 Insertion: displacement of T1-T6 BCAM4. . . . .	91
C.4 Transport: corrected vertical displacements. . . . .	92
C.5 Transport: corrected horizontal displacements. . . . .	92
C.6 Pump-down: corrected vertical displacements, from BCAM2 to BCAM4. . . . .	93
C.7 Pump-down: horizontal displacements, from BCAM2 to BCAM4. . . . .	93
C.8 Cooldown: vertical displacements, from BCAM2 to BCAM4. . . . .	94
C.9 Cooldown: horizontal displacements, from BCAM1 to BCAM3. . . . .	94



---

# Chapter 1

## Introduction

Neutrinos are tiny, neutral subatomic particles that have mass but no charge. They were first proposed in the 1930s by physicist Wolfgang Pauli, who suggested they were necessary to conserve energy and momentum in certain types of nuclear reactions. Neutrinos are produced in many natural processes, such as the nuclear reactions at the core of the sun and cosmic ray interactions in the Earth's atmosphere. They are also generated in laboratory experiments, such as in particle accelerators and nuclear reactors. Despite their abundance, neutrinos are extremely difficult to detect as they interact very weakly with matter, making them one of the most elusive particles in the universe.

### 1.1 Fermi National Accelerator Laboratory

Fermi National Accelerator Laboratory (Fermilab) is a United States Department of Energy national laboratory specializing in high-energy particle physics. It is located in Batavia, near Chicago, and it is managed by the Fermi Research Alliance LLC, a partnership of the University of Chicago and Universities Research Association Inc., a consortium of 89 research universities. The laboratory was named after the Italian physicist, Nobel prize winner, Enrico Fermi. Fermilab is focusing on many experiments:

- The laboratory is housing the world's largest neutrino experiment (Deep Underground Neutrino Experiment, DUNE), with the aim of detecting and measuring the properties of such particles.
- Fermilab participates in the Large Hadron Collider, the largest particles accelerator in the world built in Geneva, Switzerland.
- Fermilab leads the Dark Energy Survey, known as DES, which analyzes data obtained with one of the world's largest digital cameras to investigate the nature of dark energy.

## 1.2 PIP-II

Proton Improvement Plan-II (PIP-II) is Fermilab's plan for providing an high-intensity proton beams to the laboratory's experiments. PIP-II features a 800-million-electronvolt leading-edge superconducting radio-frequency (SRF) linear accelerator (linac) that will enable the Fermilab complex to deliver more than a megawatt of beam power to LBNF (long baseline neutrino facility). Furthermore, the accelerator complex will be used to deliver electrons to the muon-to-electron-conversion (Mu2e) experiment. PIP-II project is built in collaboration with many countries, like France, Italy, India, United Kingdom and Poland. Institutions in these countries are contributing in their areas of expertise. The aerial view of the PIP-II complex can be appreciated in Figure 1.1.

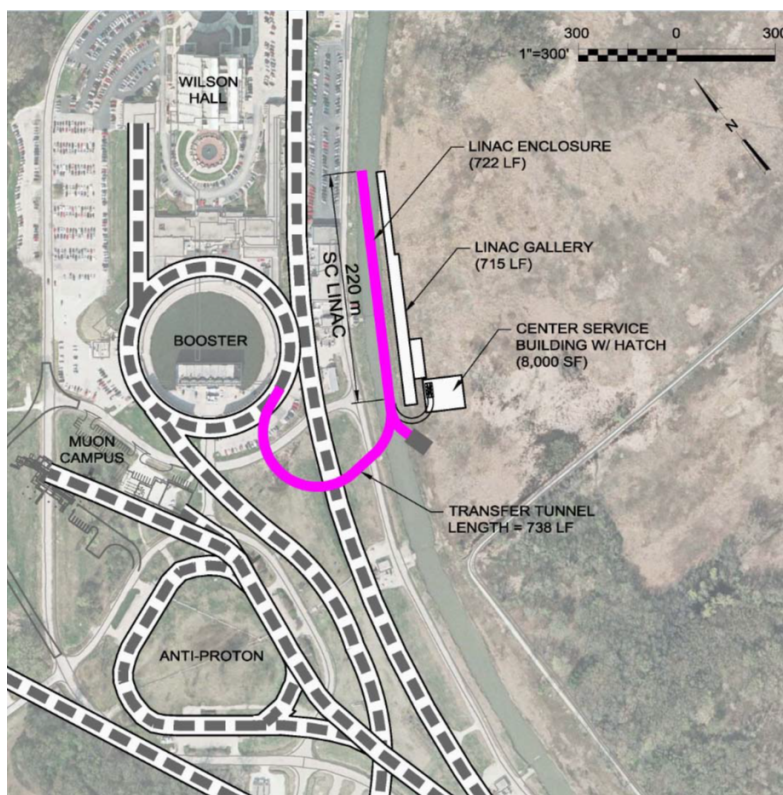


Figure 1.1: Aerial view of the PIP-II complex<sup>11</sup>.

### 1.2.1 Ions source and early stages of acceleration

Protons are made from hydrogen gas, which is broken apart into electrically charged ions that can be accelerated. In PIP-II, the ion used is called H-minus, which consists of a proton with two electrons attached. The transformation from hydrogen to ions takes place in the "ion source". At the end of it, ions are moving at 0.7% the speed of light. The first stage of acceleration takes place in three different devices at room temperature:

- Low Energy Beam Transportation (LEBT), which focuses, shapes and directs the particles beam to fit the size, position and angle requirements for the Radio Frequency Quadrupole.
- Radio-frequency quadrupole (RFQ). It generates electromagnetic waves with a frequency of 162.5 MHz. This device is 4 meters long and made of copper. Once the H<sup>-</sup> ions exit the RFQ, they have about 7 percent the speed of light (2.1 MeV).
- Medium Energy Beam Transportation (MEBT), serving the same purpose of the LEBT. Poor beam quality would lead to beam loss downstream. The MEBT is the last device before the linear accelerator.

### 1.2.2 Linear Accelerator

The linear accelerator is more than 215 meters long, and accelerates protons from 7% to 84% the speed of light. The linac consists of superconductive cavities and focus lens called solenoids. The former increase the H<sup>-</sup> energy from 2.1 MeV to 800 MeV, while the latter are needed to steer and to focus the ions beam. The generated accelerated protons are then separated depending on the research program.

The PIP-II linear accelerator uses superconducting radio-frequency (SRF) technologies to accelerate the particles' beam: an oscillating electric field is generated inside metallic structures (cavities), which accelerates the protons beam. In the presence of an oscillating field, electric currents flow within the metallic walls of these structures, generating heat that negatively affects the accelerator performance. For this reason, cavities are built in niobium: it is a metal that, when cooled below 4 K (called critical value), loses its electrical resistance, which means that no energy is wasted in heat. Niobium cavities, during operation, are cooled down to 2 K with liquid helium. Niobium is said to be superconductive below its critical temperature.

A number of cavities, ranging from three to eight, are assembled into a unit called cryomodule (CM). Depending on the cryomodule type, cavities could be assembled next to solenoids. In PIP-II, 23 CMs house 116 cavities. The cryomodule supplies the required liquid helium bath and vacuum pressure, with the aim of insulating the cavities from the external environment at room temperature and at atmospheric pressure. PIP-II uses five different types cavities designed to efficiently accelerate H<sup>-</sup> ions to a particular velocity. The cavities are grouped into three families: half-wave, single-spoke and elliptical, each one with its own specific working frequency. Each cryomodule houses cavities that share a given family. There are in total three families of cryomodules:

- The first CM in the linac is called Half Wave Resonator (HWR). It consists of eight cavities operating at the same frequency as the RFQ (162.5 MHz), and it accelerates the H<sup>-</sup> up to 10 MeV.

## 1. Introduction

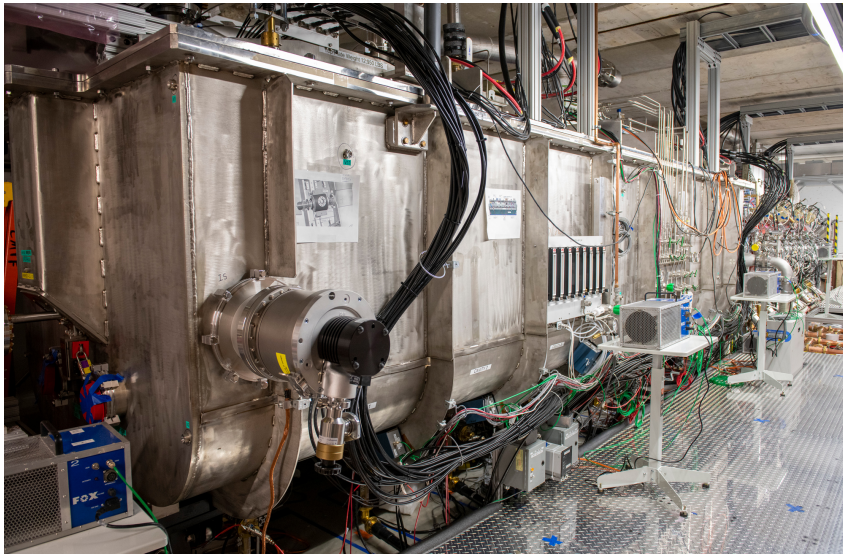


*Figure 1.2: Half Wave Resonator module installed at Fermilab<sup>12</sup>.*

- The second CM in the linac belongs to the Single Spoke Resonator (SSR) family. There are two types of SSR CMs, called type 1 and type 2, and in total nine cryomodules in the linear accelerator. Superconductive cavities housed inside operate at a frequency of 325 MHz, double the amount of the HWR. The particles beam coming out of the SSR cryomodule has an energy of 185 MeV.



*Figure 1.3: Prototype SSR1 Cryomodule assembled and tested at Fermilab<sup>12</sup>.*

- The last family of CMs in the linear accelerator houses elliptical cavities. There are two slightly different types. One is called Low Beta 650 (LB650), while the other is called High Beta 650 (HB650). They both operate at a frequency of 650 MHz, and accelerate the H<sup>-</sup> ions up to the final 800 MeV.

Once the H- ions have completed all the linear accelerator stages, they are directed to the Fermilab accelerator complex. Some of them will be further speeded up to 120 GeV for the LBNF. The remaining will be used for the Mu2e experiment. The overall scheme of the PIP-II plant can be seen in Figure 1.4.

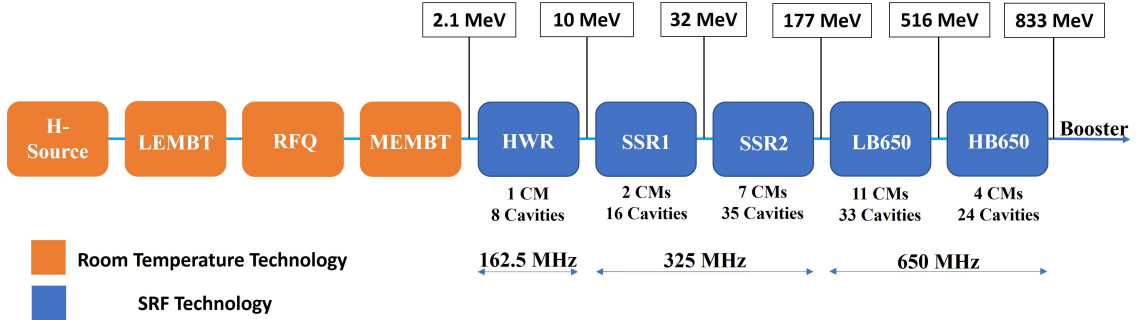


Figure 1.4: PIP-II Scheme, from H- Source to booster.

### 1.3 Importance of the Alignment Monitoring

The particle accelerator performances highly depend on the relative alignment of its internal components. Indeed, misalignments deviate the particles beam from its ideal trajectory, thus inducing beam degradation which prevents the whole system from accelerating the H- ions to the target energy. In the hundreds meters long linac, the tolerances of the charged ions beam are in the micrometric orders of magnitude: the misalignment of even a single component could induce an energy loss, reduced accelerating gradient and power dissipation, leading to inaccurate results.

Cavities and solenoids are installed at room temperature inside the cryomodules. During operation, because of the thermal gradient applied, the coldmass assembly shifts away from its original position. The alignment requirement is different between cavities and solenoids: for an SSR1 CM, the constraint limits are summarized in Table 1.1.

Table 1.1: Alignment requirements for an SSR1 CM.

Transverse Cavity Alignment Error, RMS [mm]	< 1
Angular Cavity Alignment Error, RMS [mrad]	< 10
Transverse Solenoid Alignment Error, RMS [mm]	< 0.5
Angular Solenoid Alignment Error, RMS [mrad]	< 1

The correct alignment of the string assembly is measured as the maximum deviation of the beam pipe from the reference orbit evaluated with the Root Mean Square

method<sup>1</sup>. During assembly, the relative position between cavities and solenoids is checked by a laser tracker system, which compares the beam pipes position to external fiducial points. The displacements, which happen at cryogenic temperatures, are compensated during assembly using Finite Element Analyses (FEA) results. Cavities and solenoids inside a cryomodule sits on a system of plates and screws, which allows adjustability in five Degrees of Freedom (DOF). Once the initial position is evaluated, each coldmass component is adjusted to meet the required alignment constraints.

In addition to this classic position monitoring technique, an innovative alignment monitoring system, based on optical cameras, is used. Not only it is employed to trace the positions of cavities and solenoids during final assembly phases and transportation (like the laser tracker system described above), but also during cooldowns and warmups, allowing a comparison between experimental data and theoretical results given by the FEA. The cameras acquisitions can output the displacements of internal components in time, allowing for a "live" alignment monitoring that cannot be achieved with the classic method. This system consists of two main devices: cameras, called H-BCAMs, and highly reflective targets.

H-BCAMs were first employed for the prototype SSR1 cryomodule, and they were successfully tested and validated. Furthermore, they will be employed for the next cryomodules designed and built at Fermilab. Prior to these, H-BCAMs were first used in the HIE ISOLDE experiment at CERN.

---

<sup>1</sup>The Root Mean Square (RMS) is defined as the square root of the mean square of a set of number  $x_i$

---

## Chapter 2

# Optical Alignment Monitoring System

The Boston CCD Angle Monitor “type H” (H-BCAM) is an optical instrument used for alignment monitoring, where the position and movement of reflective targets needs to be traced. The monitoring aims at checking the translations and rotations of some components due to environmental conditions and cooldown operations. The BCAM was developed and manufactured by the Brandeis University High Energy Physics (BNDHEP) Department in the years 1999-2021 with funding from the United States Department of Energy. A H-BCAM camera has relative accuracy  $5 \mu\text{rad}$  within its field of view, and absolute accuracy  $50 \mu\text{rad}$  with respect to its mounting plate.<sup>13</sup>



*Figure 2.1: H-BCAM. The front lens is visible, with two laser diodes on either sides. Above and below the lens are the four LED flashes<sup>13</sup>.*

The camera consists of two lens and two Charged-Coupled Device (CCD) image sensors, whose dimensions are 5.1 mm × 3.8 mm, giving a matrix of 700 by 520 pixels. It is equipped with four red laser diode light sources and eight white LED illuminators for retro-reflecting targets. The embodied lasers act as a source of light: they are flashed on the targets and the image is acquired by the sensors. The position in pixel points is found by scanning the luminosity peaks in the picture (because targets are highly reflective). The bottom surface of each camera has three depressions, a flat, a slot, and a cone, which can be appreciated in Figure 2.2. These allow the H-BCAM to sit kinematically on three quarter-inch (6.35-mm diameter) steel balls (SS 316).<sup>13</sup> This system is designed to not over-constrain the H-BCAMs to the plate where it is installed. Precision in the installation is indeed required because the cone, in the mounting plate, represents the origin of the coordinate system of the camera.

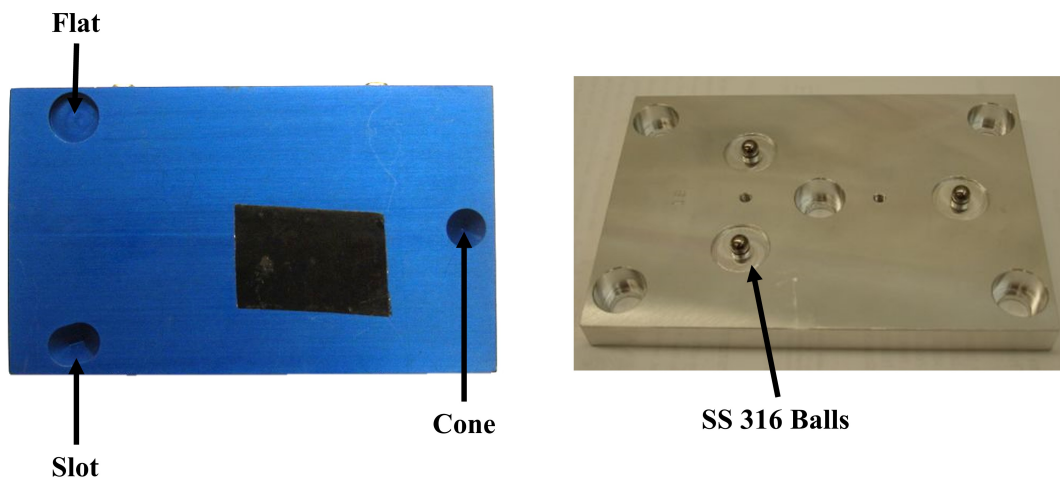


**Figure 2.2:** On the left, the bottom surface of a blue H-BCAM. On the right, its mounting plate with SS316 spheres<sup>13</sup>.

## 2.1 Targets

Targets are used to trace the position of the component they are installed on. Each target is an assembly made of different parts, showed in Figure 2.3:

- A target tube, in which two glass balls with a high reflective index (about 2) are spaced inside along with ceramic balls and springs. The nominal distance between the two glass spheres is  $d = 28mm$ .
- A target frame, which has V-shaped grooves where each tube is mounted.
- A survey base, which holds in position the target frame.
- A bracket, used to mount the assembly on the component to be monitored.

The target frame can be adjusted vertically and horizontally with respect to the survey base, and once the correct position is found its position is fixed by tightening some bolts. All the assembly parts are made of Titanium Grade 2 alloy, and are anodized to reduce their reflection coefficient so that, during the acquisition, only the glass spheres position is captured by the cameras.

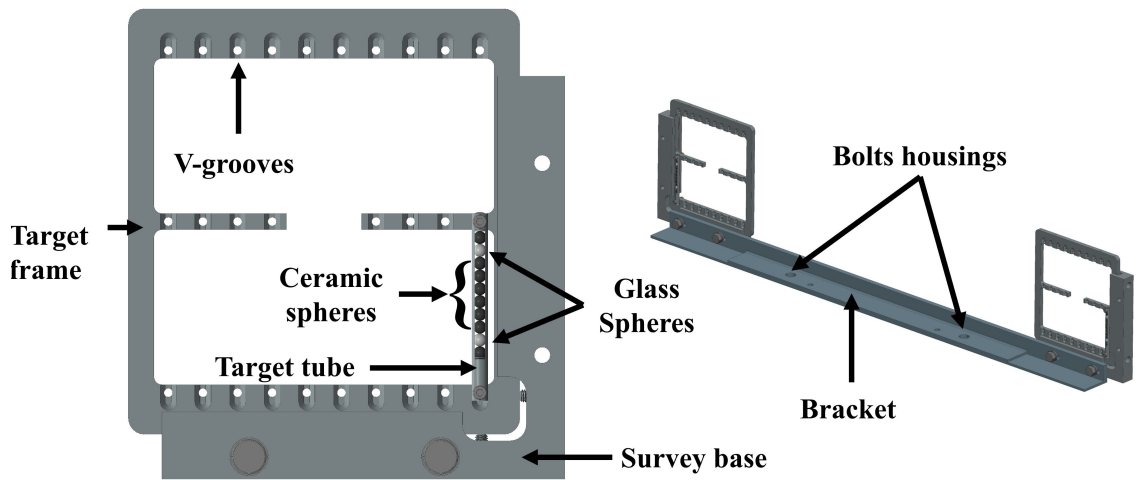


**Figure 2.3:** Target frame assembly with all its components. It is blocked on top of either cavities or solenoids thanks to the bolts and nuts.

Each component to be traced has generally four target frames installed on. In this way, it is possible to place the glass spheres in a plane to evaluate the rotations about the three axes (*pitch*, *roll* and *yaw*). To build a plane, the minimum amount of points is three: the fourth point is used to check if the component is deforming differently from design predictions. Rotations are then evaluated from the acquired translations.

## 2.2 H-BCAM Working Principle

An H-BCAM uses its laser to monitor the position of an object in its field of view. The laser ray hits the glass sphere, it is reflected and its position on the image sensor is measured. It is assumed that the laser lays along the line passing through the lens and its image on the CCD sensor. The BCAM is sensible to targets movements across its field of view, but no to movements towards or away from it.

The camera working principle is showed in Figure 2.4. The higher is the reflection angle  $\alpha$ , the higher the length  $h$  becomes, which translates into a different amount of pixels from the camera axis. With this principle, it is possible to record the reflective targets position.

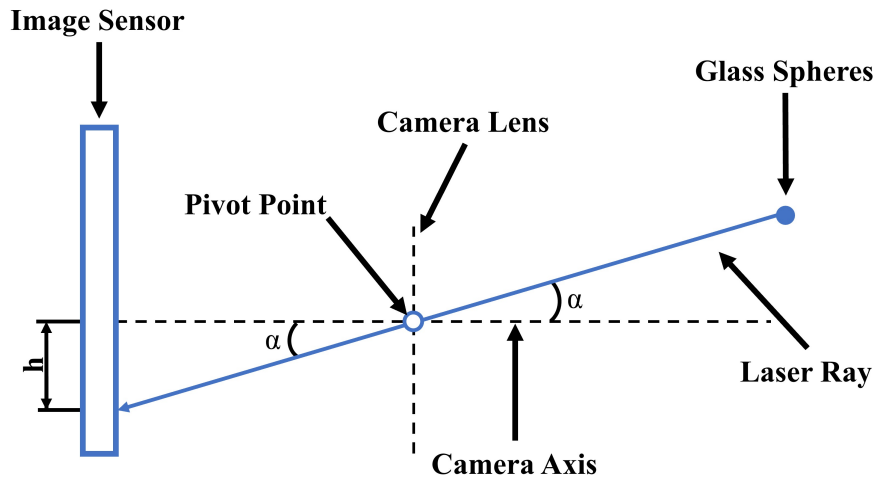


Figure 2.4: Working principle of a H-BCAM. The length  $h$  is proportional to the laser ray angle  $\alpha$ .

Each H-BCAM is assumed to be a thin lens, which means that any ray passing through the center of the lens does not get bent, but it remains straight. In reality it is not, mainly because its optical center does not coincide with its physical center. Nevertheless, an equivalent thin lens system is assumed, where the pivot point is the center of the camera virtual perfect lens, and where the camera axis joins the image sensor center and the lens center.

To translate pixels into real measurements in the reference system, a proper calibration is needed. The scheme reported in Figure 2.5 summarizes what is happening during an acquisition.

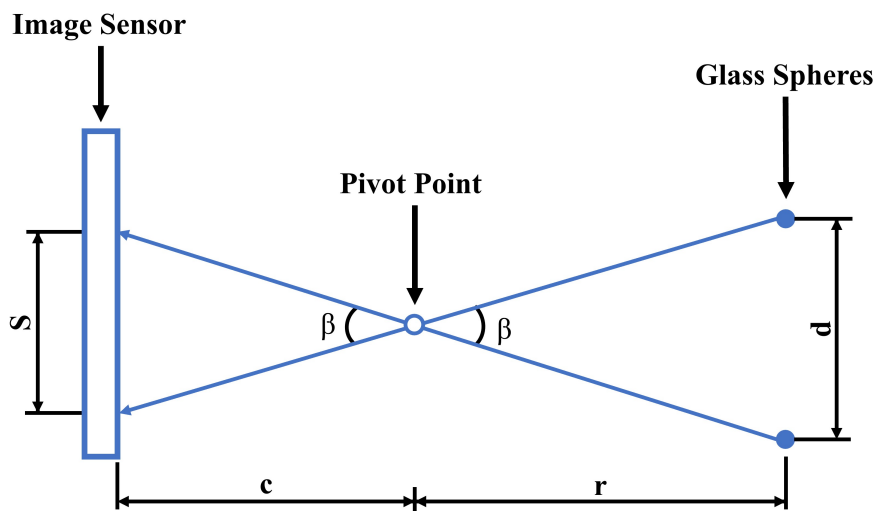


Figure 2.5: Simplified working principle of a H-BCAM in its field of view.

Since the distance  $d$  between the two glass spheres is known, the distance  $s$  between the two glass spheres in pixels is used to evaluate the parameter  $K$ :

$$K = \frac{d}{s} \quad (2.1)$$

The parameter  $K$  is constant for a certain target at a fixed distance, and it is used to translate its displacements from pixels to millimeters thanks to equation 2.2.

$$\Delta x = (x_n - x_0) \cdot K \quad (2.2)$$

Where:

- $x_n$  is the target position, in pixels, at the n-th timestamp.
- $x_0$  is the initial target position, in pixels.

A similar approach is adopted to find the distance  $r$  between camera and target. Relying on the scheme presented in Figure 2.5, the range is evaluated as:

$$\beta = \frac{d}{r} = \frac{s}{c} \quad (2.3)$$

$$r = \frac{d}{\beta} \quad (2.4)$$

Where:

- $\beta$  is the angle subtended by the lasers beam separation.
- $c$  is the distance between the lens and the CCD image sensor, measured in millimeters. It is a calibrated distance given by the H-BCAM manufacturer.

Each camera can also find the position of another camera at a certain distance. Instead of using highly reflective targets, the H-BCAM, whose position needs to be found, turns on alternatively the two LED lights and their distance in pixels is found. This is used, like the parameter  $s$  in equation 2.1, to divide the real distance between the two flashes to evaluate the parameter  $K$ .

To instruct the H-BCAMs for the data acquisition, the tool provided by the LWDAQ® (Long-Wire Data Acquisition) software takes in input an acquisition file, which is a text script file containing all the information to acquire the data from the targets:

- Number of targets to find. This number depends on the type of target: if a BCAM is looking at a target frame equal to the one reported in the previous paragraph, the number of targets is two since there are two glass spheres. On the other hand, if the camera is looking at another camera, it will only search for one target, which is the LED light.

## 2. Optical Alignment Monitoring System

---

- Duration of the flash. Depending on the lighting conditions, the BCAM will automatically adjust the flash duration to capture the best quality image possible. This process directly affects the exposure time of the image sensor to capture the right amount of light every time.
- Restricted area to scan. Since there usually are more than one target to trace, it is possible to specify a restricted region of the CCD sensor where the BCAM has to look for a target. This calibration is done to ensure that the camera is looking at the right target at each acquisition.

The acquisition software gives in output another text file with all the recorded information, which are:

- Position  $x$  and position  $y$ , in pixels, of the target center (glass sphere or camera flash).
- Number of pixels which reflects the light.
- Peak intensity, which is the amount of light reflected captured by the sensor.

The output text file is loaded into a MATLAB® script to post-process the acquisition. To reach better accuracy, repeated measurements are taken and averaged.

---

## Chapter 3

# Spoke Test Cryostat

The Spoke Test Cryostat (STC) is a testing facility built to test lower frequency cavities (325MHz), used primarily for accelerating beams of heavy ions or protons. The test is performed to check the cavity functionality before it is inserted in the cryomodule, as well as to make sure that all the facilities used (mechanical, cryogenic, vacuum, instrumentation, RF systems, safety) work properly. In the STC, the superconducting cavity is characterized to assess its performances, and it is qualified to be inserted into the cryomodule. Moreover, the test is useful to validate the coupler and the tuner, external components of the cavity, which are necessary for its correct performance during operation.

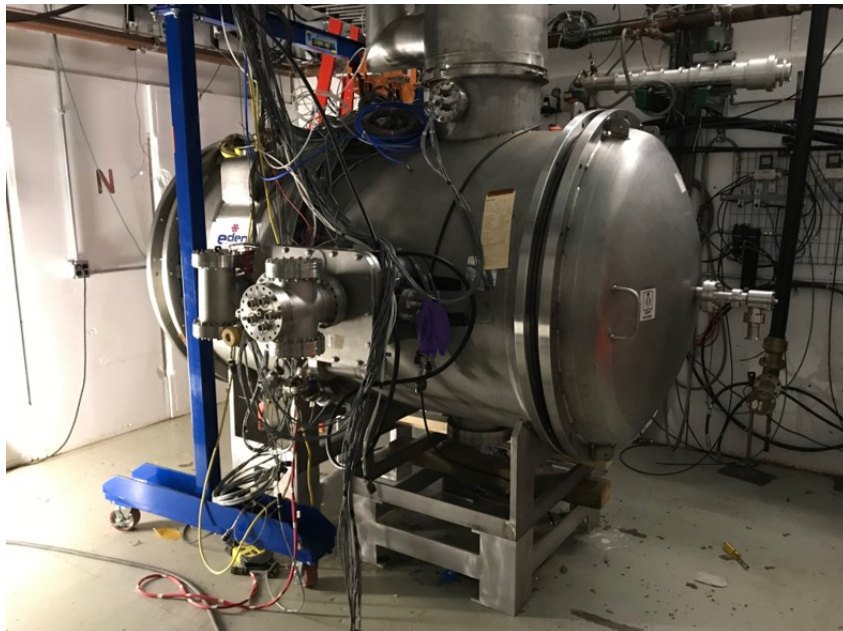


*Figure 3.1: Spoke Test Cryostat facility at Fermilab<sup>11</sup>.*

### 3. Spoke Test Cryostat

---

For the STC test, the cavity is placed inside a stainless steel cryostat, aligned along the coupler port, bolted on a titanium plate and connected to the liquid helium line through the two-phase pipe on the upper side. The liquid helium supply is at the bottom of the cryostat: once it heats up, the generated vapor rises up thanks to its lower density and it is collected in the two-phases pipe. The cryostat has two dome doors on each side providing access for cavity installation.

The vacuum vessel is equipped with: a magnetic shield, fixed on the inner surfaces of the cryostat, which aims at minimizing the electromagnetic interference that may affect the cavity functionality during the test, and a thermal shield, which encloses every component tested during the experiment. The latter is made of aluminum alloy sheets and extrusions (pipes). The thermal shield function is to reduce the heat load on the 2 K volume by providing thermal intercepts and by stopping the radiation from room temperature components. It is convection cooled down by liquid nitrogen flowing in the extrusions. Thermal straps made of copper provide the connection between the thermal shield and the parts which have to be cooled down.

The second aim of the STC test is to check the cavity deformations under the same load conditions met during operation inside the cryomodule. The displacements along the three main axes are measured thanks to three H-BCAMs, which read the position of the reflective targets mounted on the upper portion of the cavity. Inside the cryostat, the H-BCAMs are installed on an aluminum stand placed in front of the cavity, facing the front flange and parallel to the tuner (Figure 3.2).

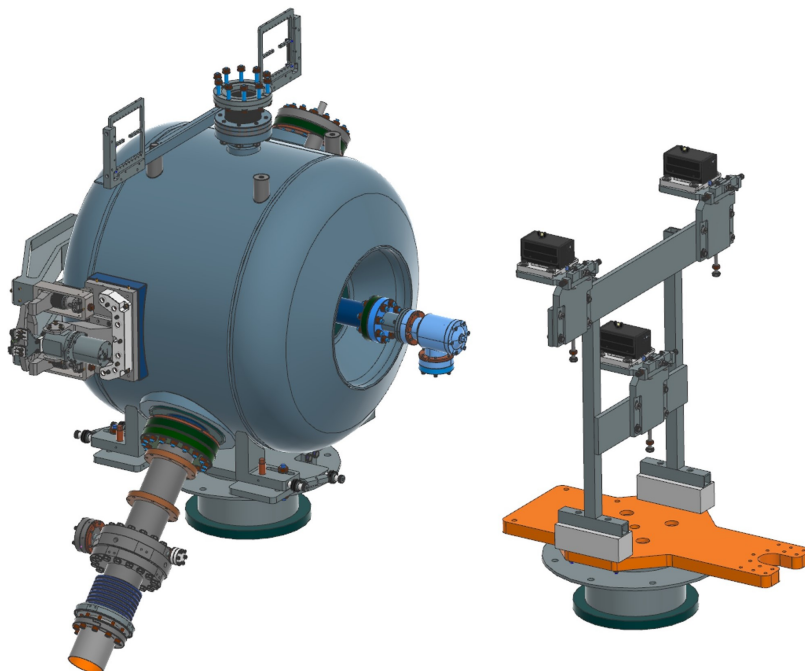


*Figure 3.2: STC configuration: SSR2 cavity with targets installed and H-BCAMs stand.*

### 3. Spoke Test Cryostat

The stand is heated thanks to two film heaters to keep the H-BCAMs at room temperature during the test at cryogenic conditions, which is crucial to make them work properly since the cameras are not designed to operate in such an environment. The cavity's deformations (due to the thermal shrinkage) are evaluated thanks to equation 2.2.

One last aim of the experiment is to compare the experimental values acquired by the H-BCAMs and the results of the finite elements analysis to check the model accuracy. This topic will not be discussed in this thesis. All the equipment tested is provided with temperature sensors to check not only the temperature reached in steady-state conditions, but also the temperature gradient across the components.

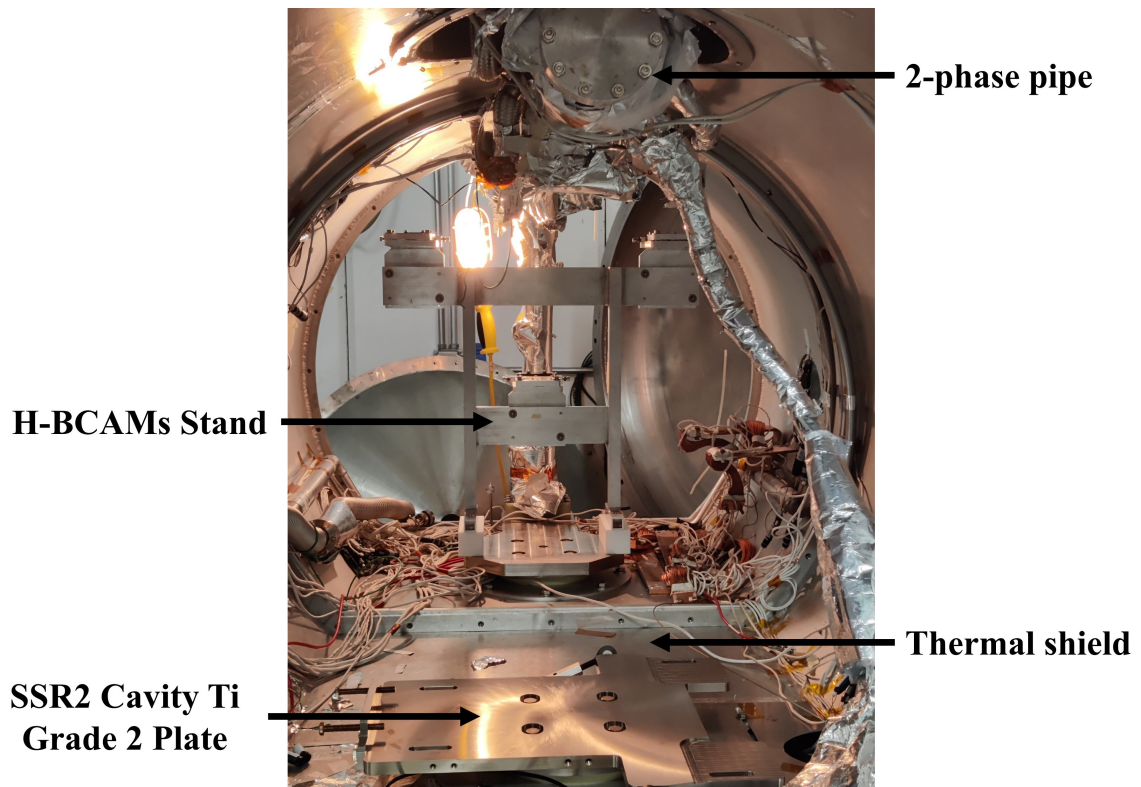


*Figure 3.3: Internal environment of the STC with the H-BCAMs aluminum stand installed.*

#### 3.1 H-BCAMs Stand

The H-BCAMs stand is a device used to hold in position the H-BCAMs during the test in the STC. It is made from aluminum 1/4" square tubes welded together. It is thermally insulated from the support post thanks to two PTFE blocks and its position is fixed on the latter with bolts and nuts. Its main components are shown in Figure 3.4 and 3.5.

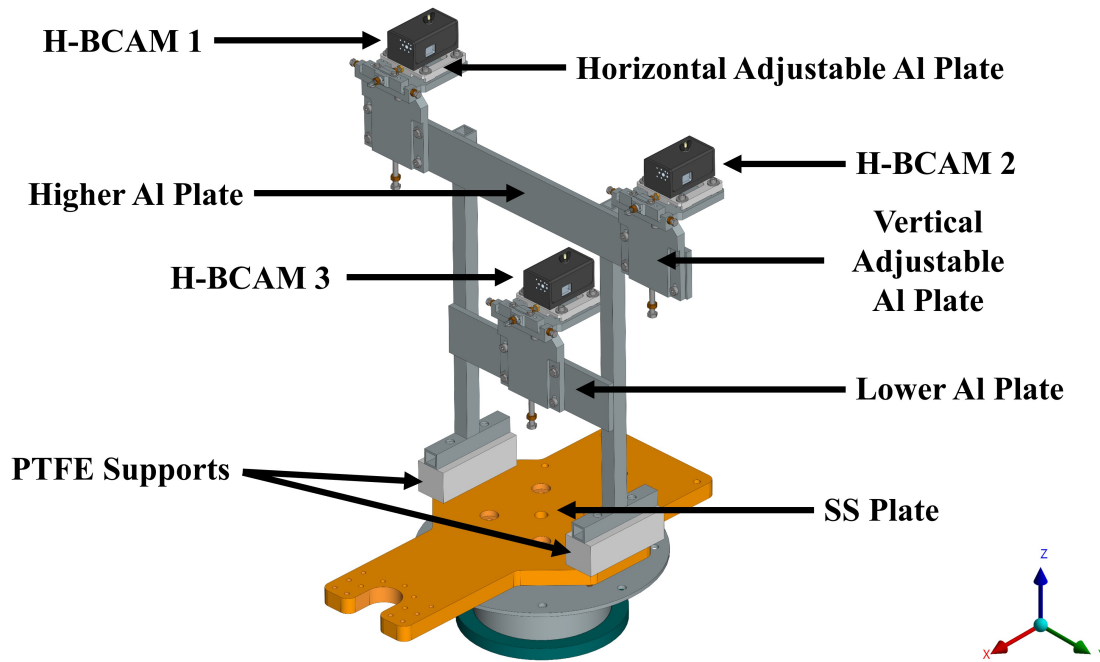


Figure 3.4: H-BCAMs stand main components description, isometric view.

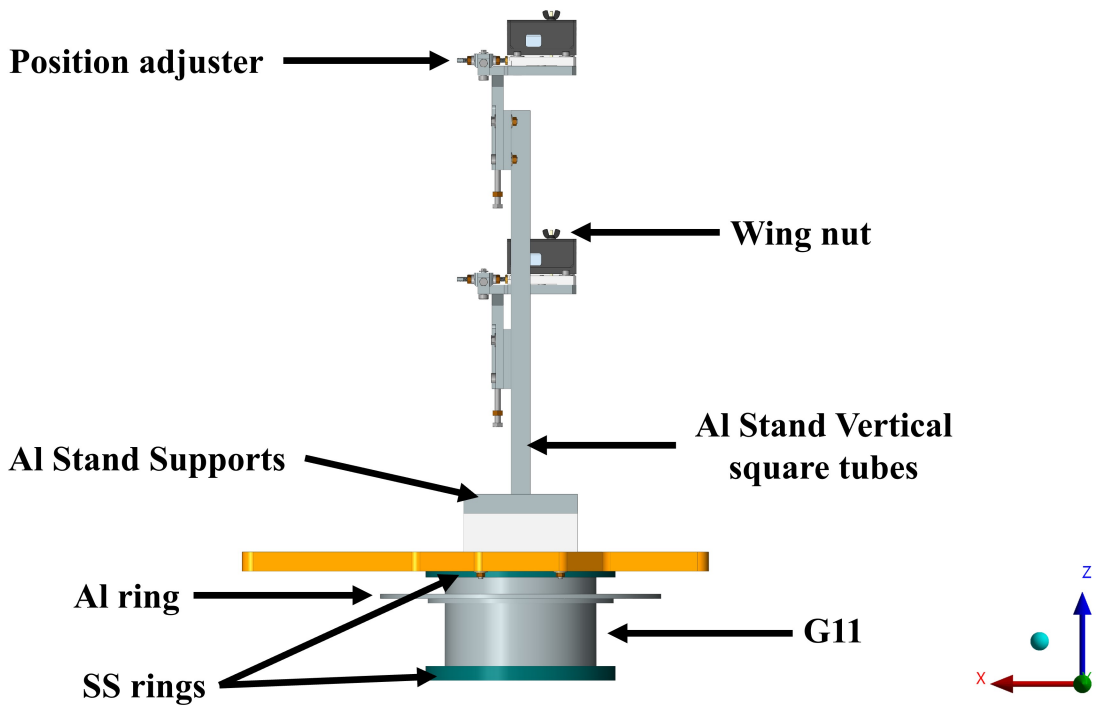


Figure 3.5: H-BCAMs stand main components description, side view.

### 3. Spoke Test Cryostat

---

The support post is a piece of equipment used to anchor the stand to the vessel. It is made of a 3 mm thick fiberglass G11 cylinder with low thermal conductivity at low temperatures, to thermally isolate the cold components from the room temperature cryostat. Disks are shrink fitted inside the composite tube to support Multi-Layer Insulation (MLI) plies, a material used to limit the thermal radiation coming from the warmer vessel. Rings are fitted outside the cylinder, in correspondence of disks to anchor the support post to the cryostat and to support the stand. Both disks and rings are made of stainless steel (SS). One couple of disk and ring is made of aluminum, and it is used to support the thermal shield in position during the STC test.

The stands accommodates three H-BCAMs, fixed on three equally shaped aluminum plates which can be moved along the three directions ( $x$ ,  $y$ ,  $z$ ). Adjustments along  $x$  and  $y$  are granted by both the position adjuster and the horizontal adjustable plate. The former is used to finely tune the H-BCAM, the latter coarsely sets the camera position for the STC test. The displacement along  $z$  is ensured by the vertical aluminum plate. Once the correct position of the cameras is found, each camera is fixed to the movable aluminum plate by a wing nut, while the latter is tightened to the fixed aluminum plate by four bolts.

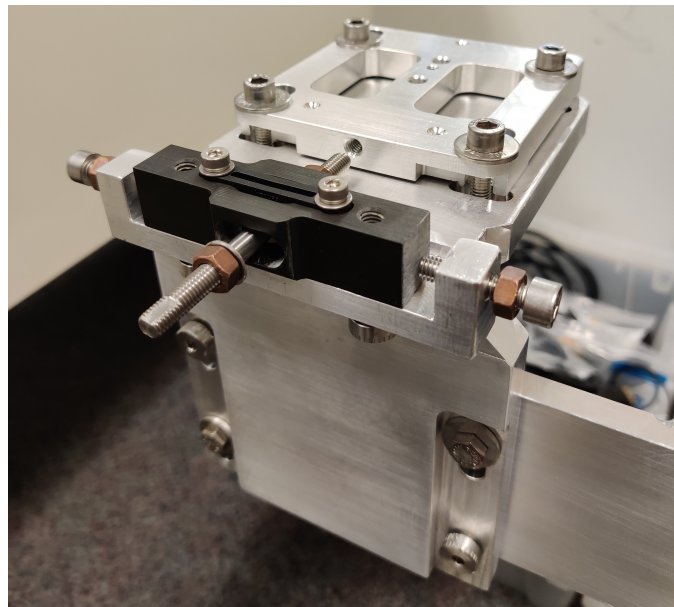


**Figure 3.6:** Close-up of the stand. Position adjuster, vertical and horizontal adjustable plates are visible.

The stand is also instrumented with temperature sensors to monitor the temperature gradient across its components during the test, and to compare the experimental results with the ones found in the finite element analysis. This is crucial to validate the stand model. Two film heaters, manufactured by MINCO®, are installed on the stand. They are made of Polyimide, a material suitable for vacuum environment, and they can also

be operated at cryogenic temperatures. The heaters are 1” x 4” big, they have a power density of 10 W/in<sup>2</sup> and they can be powered until 33.2 W. A power supply is needed to turn the heaters on and off, depending on the experiment set up. For the test in the STC, a power supply with a resolution of 1 mV was chosen.

### 3.1.1 Model and Scope of the Analysis

In the H-BCAMs stand model, the contact in between every component was modeled as frictional, which means that:

- The gap between the two surfaces in contact can either open or close.
- Sliding is allowed if  $F_{sliding} > F_{frictional}$ , so a friction coefficient must be provided. The coefficients set in the model are reported in Table 3.1.

*Table 3.1: Friction coefficients*

Materials	Friction Coefficients [-]
Aluminum-Aluminum	1.20
Aluminum-PTFE	0.24
Stainless Steel-PTFE	0.13
Stainless Steel-Stainless Steel	0.65
Stainless Steel-Aluminum	0.61

The contact between the support post and the stainless steel plate was set as frictionless in accordance with other models built at Fermilab in the past. This type of contact allows both sliding and opening or closing of the two surfaces, but it prevents penetration. As for the support post, each couple of disk and ring was fixed to the composite tube with a bonded contact, which does not allow neither sliding nor opening. It simulates the interference fit between the components. The same contact type was used to model the welds between the vertical square tubes, the upper and lower plates and the aluminum stand supports.

Every bolted connection was reproduced with a mono-dimensional beam, made up by two nodes of six degrees of freedom each (three translations and three rotations). To make it more accurate, the beam was tied to the imprint of the washer on the surface (instead of the edge of the threaded hole). This was done for both sides. A bolt pretension was then applied to replicate the effect of tightening. The axial load set was evaluated as it showed in equation 3.1:

$$F_A = \frac{M_A}{0.16P + 0.52d_2\mu_g} \quad (3.1)$$

Where:

- $M_A$  is the tightening torque evaluated from Table A.1.

- $P$  is the screw pitch.
- $d_2$  is the nominal diameter of the screw.
- $\mu_g$  is the frictional coefficient between screw thread and housing.

**Table 3.2:** Axial preload calculation.

$M_A$ [Nmm]	6440
$P$ [mm]	1
$d_2$ [mm]	6
$\mu_g$	0.60
$F_A$ [N]	3000

In the model described, the H-BCAMs were not considered because it was assumed that cameras and adjustable plates have the same displacements. The aim of the analysis is to find the displacements of all the components in the model, as well as the temperature of the adjustable plates. These two information are necessary to find the optimal position of the two film heaters, and to calibrate the positions acquired by the H-BCAMs during the actual test in the STC. Indeed, by knowing how much the cameras move during the cooldown process, it is possible to estimate with higher precision movement of the targets fixed on the SSR2 cavity.

### 3.1.2 Material properties for the Finite Element Analysis

The material properties can sensibly vary depending on the temperature. For this reason, a deeper study is needed both for mechanical and thermal properties to analyse the stand with the Finite Element Method (FEM). Two types of analyses were conducted on the H-BCAM support stand: steady-state thermal and static structural. To solve the steady-state thermal analysis, the thermal conductivity of materials has to be provided in the model. As for the static-structural analysis, the Young's modulus, the Poisson's ratio and the coefficient of thermal expansion need to be expressed.

For isotropic materials, where the properties are constant independently from the direction, the dependence of each property (thermal and mechanical) on the temperature is investigated in the range from 2 K to 300 K. As for the G11, because it is a composite, orthotropic material, whose properties depend on the direction, the properties must be expressed in three main directions (normal, warp and out of plane direction) with respect to the temperature. The G11 is a glass epoxy composite laminate where fibres are placed along two directions, called normal and warp, while the fibres binder is epoxy resin (also called matrix). The properties (both mechanical and thermal) along direction one and two mainly depend on the fibres. Along the out of plane direction, properties depend solely on the matrix. To see all the properties of the materials used in the analyses, refer to the appendix.

### 3.1.3 Steady-State Thermal Analysis

The steady-state thermal analysis goal is to find the temperature distribution across the stand during nominal operating conditions. Once this result is obtained, the next objective is to find where to position the two film heaters and, as a consequence, to obtain the power to supply to make sure that: the temperature of each H-BCAM is close to room temperature, to ensure they can operate under cryogenic conditions; the vertical displacement of the lower and higher H-BCAMs adjustable plate is the same. This is crucial to have an accurate measurement of the cavity displacements during the test in the STC.

The stand is placed inside the cryostat under vacuum, which means that only conduction and radiation are considered as forms of heat transfer. The fixed temperatures set in the model are:

- The support post surfaces in contact with the cryostat are set at room temperature, 294.35 K.
- The aluminum ring in contact with the thermal shield is set at 80 K.

The radiation considered is the one exchanged from the outer surfaces of each component of the stand to the cooled environment inside the vacuum vessel. Since the thermal shield encloses both the cavity and the stand, and since its average temperature is 80 K from other analysis performed, it is assumed that the chamber at steady-state reaches the same temperature. In the numerical analysis, each body is considered as a grey body which can either absorb or emit energy. The energy emitted is equal to the one of a black body (which follows the Stefan-Boltzmann's law<sup>1</sup>), but scaled. The scale factor is called emissivity, which must be provided in the model. The MLI plies inside the support post have not been considered, but instead no radiation is set on the G11 inner cylindrical surfaces and on the SS and aluminum disks. The emissivity values are reported on Table 3.3. Coupling between every surfaces in contact was set, meaning that a perfect contact is supposed with infinite thermal conductivity, therefore each couple of touching faces have the same temperature. The boundary conditions are summarized in Figure 3.7.

*Table 3.3: Emissivity coefficients*

<b>Materials</b>	<b><math>\epsilon</math> [-]</b>
Aluminum 6061-T6	0.03
Stainless Steel 316L	0.07
PTFE	0.92
NEMA G11	0.90

---

<sup>1</sup> $E = \sigma \cdot T^4$ , where  $\sigma = 5.67 \times 10^{-8} \text{ W}/(\text{m}^2 \cdot \text{T}^4)$  is the Stephan-Boltzmann constant.

### 3. Spoke Test Cryostat

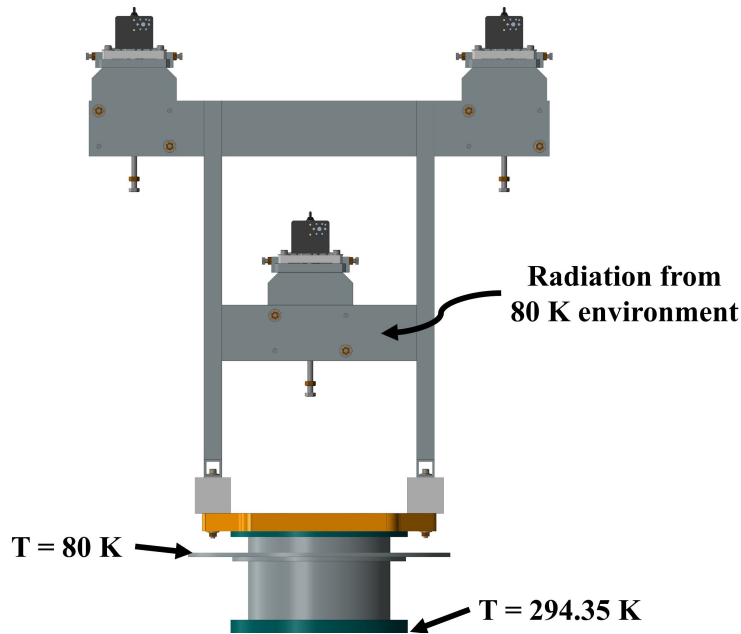


Figure 3.7: Boundary Conditions set for the steady-state thermal analysis.

The results of Steady-State Thermal Analysis, without the two heaters, can be appreciated in Figure 3.8. As expected, at steady-state the H-BCAMs stand reaches an equilibrium temperature of 80 K. This is due to the conduction from thermal shield, and the radiation coming from the cryostat cooled environment. A thermal gradient can be appreciated between the lower surfaces of the support post, at room temperature, and the aluminum ring at 80 K.

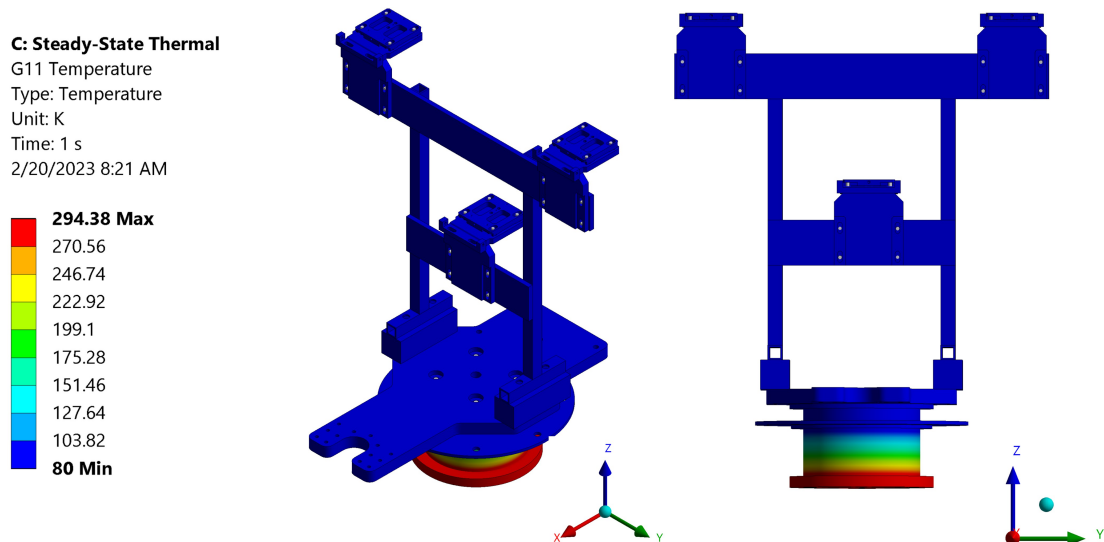


Figure 3.8: Result of the Steady-State Thermal Analysis: H-BCAMs stand temperature distribution.

### 3.1.4 Static Structural Analysis

The goal of the static structural analysis is to find the stand displacements along the three main directions ( $x$ ,  $y$  and  $z$ ), and especially the vertical displacements of the H-BCAMs. The stand is placed and fixed to the support post, which is bolted on the cryostat. As a result, all the degrees of freedom of the support post surfaces in contact with the vacuum vessel have been blocked. A fixed support constraint in the model was set to replicate this condition.

The initial temperature set in the model is 294.35 K and the solution of the steady-state thermal analysis is loaded. The main effect studied is the thermal shrinkage due to the difference between the final temperature of the stand and the initial one. For this reason, earth gravity is not considered.

The stand displacement along  $x$ ,  $y$  and  $z$  are represented in Figure B.1, Figure B.2 in the Appendix, and Figure 3.9. It is clear that the main effect of the thermal shrinking is the displacement along the vertical direction. As a matter of fact, the solution is symmetric in the XZ plane, while the displacement is negligible along the  $x$  axis being in the order of  $1 \times 10^{-3}$  mm. For this reason, results along the  $x$  will be discarded from now on.

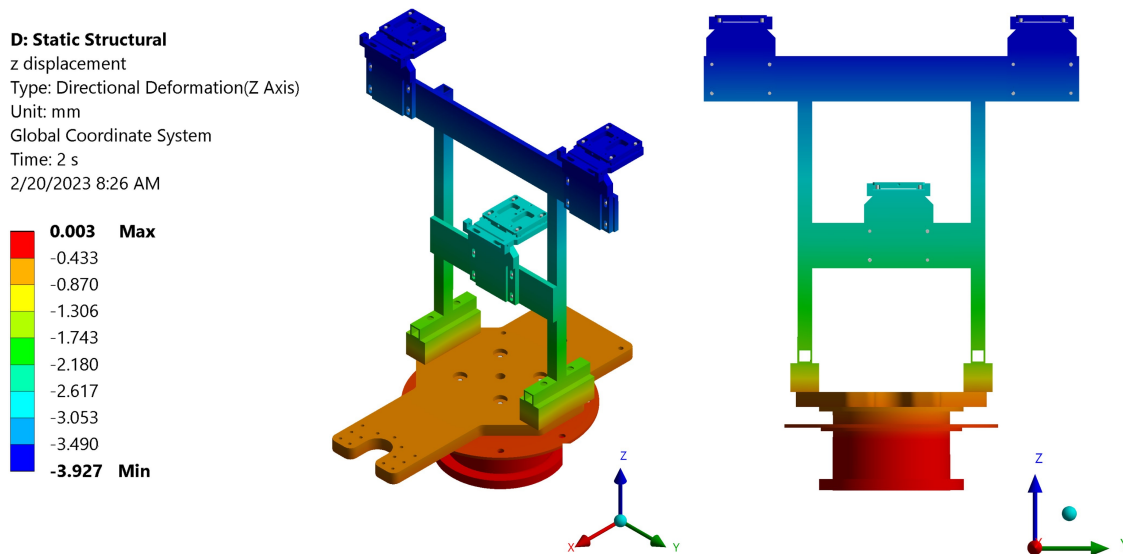


**Figure 3.9:** Results of the Static Structural Analysis: H-BCAMs stand displacements along  $z$ .

The most interesting results of the analysis are the displacements of the H-BCAMs adjustable plates, since they determine how the cameras are moving during the cooldown. In Table 3.4, the main results are presented. The displacement along  $y$  is reported as  $\pm 1$  mm since the solution is symmetric. The negative solution refers to the point 1 with positive  $y$  coordinates.

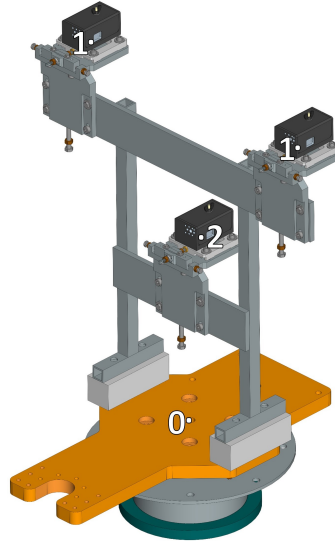


**Figure 3.10:** Reference points to evaluate the H-BCAM stand static structural analysis results.

**Table 3.4:** Static structural analysis results with no heat applied.

Point	Displacement z [mm]	Displacement y [mm]
0	-0.588	$\approx 0$
1	-3.882	$\pm 1$
2	-2.767	$\approx 0$

To check if the model was set up correctly, these results are compared with calculations made using the Coefficient of Thermal Expansion (CTE) of the different components and the solution of the Steady-State thermal analysis. Considering the height of each component, and its average temperature at the end of the analysis, it is possible to evaluate the theoretical contraction due to the difference in temperature with respect to the initial one using equation 3.2. The results are presented on Table 3.5.

$$\Delta x = CTE \cdot x_0 \cdot (T_f - T_0) \quad (3.2)$$

**Table 3.5:** Theoretical vertical displacements of the H-BCAMs stand components.

Component	Displacement $\Delta z$ [mm]
Support Post	-0.729
SS Plate	-0.070
PTFE Supports	-0.987
Al Stand	-2.289

The theoretical displacement of point 1 is equal to  $-4.075$  mm. A difference lower than  $0.200$  mm exists between this value and the result obtained in the Static Structural analysis, meaning that the model is set up correctly and its outputs are reliable.

#### 3.1.5 Sensitivity Analysis

The next step analysis is to add the two film heaters to the model. The heaters were positioned on the vertical  $\frac{1}{4}$  " tubes, at the interface with the stand support. The final position was found after many iterations: in each of them, a dummy power was applied to the heaters to observe the effect on the stand temperature and displacements. The two heaters were progressively placed on different components of the stand until both the conditions described above were satisfied: the temperature of the H-BCAMs is close to room one, and the vertical displacements of higher and lower cameras are similar.

Initially, the film heaters were placed on the two horizontal aluminum plates, to be closer to the three H-BCAMs. This position was later discarded, in favor of the final one, because it required to apply two different unknown power levels, leading to a difficult tuning of the assembly. Placing the two heaters on the vertical tubes means that the same power is applied to both, resulting in an easier characterization of the behavior of the stand under different external conditions.

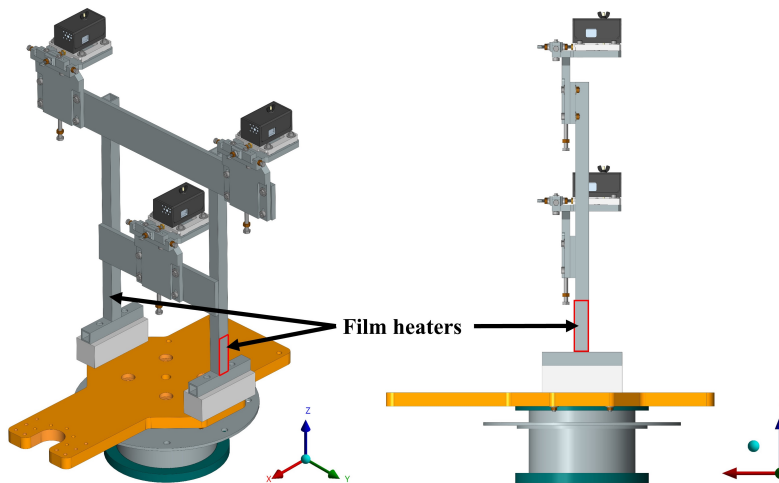


*Figure 3.11: Film heaters position on the aluminum stand.*

To find the heating power to apply, firstly it is necessary to characterize the aluminum stand behavior under different boundary conditions. The resulting analysis, called sensitivity analysis, has two main variables: the power  $P$  [W], and the environment temperature  $T$  [K]. Three different power levels were chosen,  $15$  W,  $20$  W and  $25$  W, and three different environment temperatures were set,  $60$  K,  $80$  K and  $100$  K. For each  $T$ , three different Thermal-Structural analyses were performed to find how the vertical

displacement of stand is affected by those conditions. The results are fully reported in Table B.1 in the appendix, and summarized in Figure 3.12.

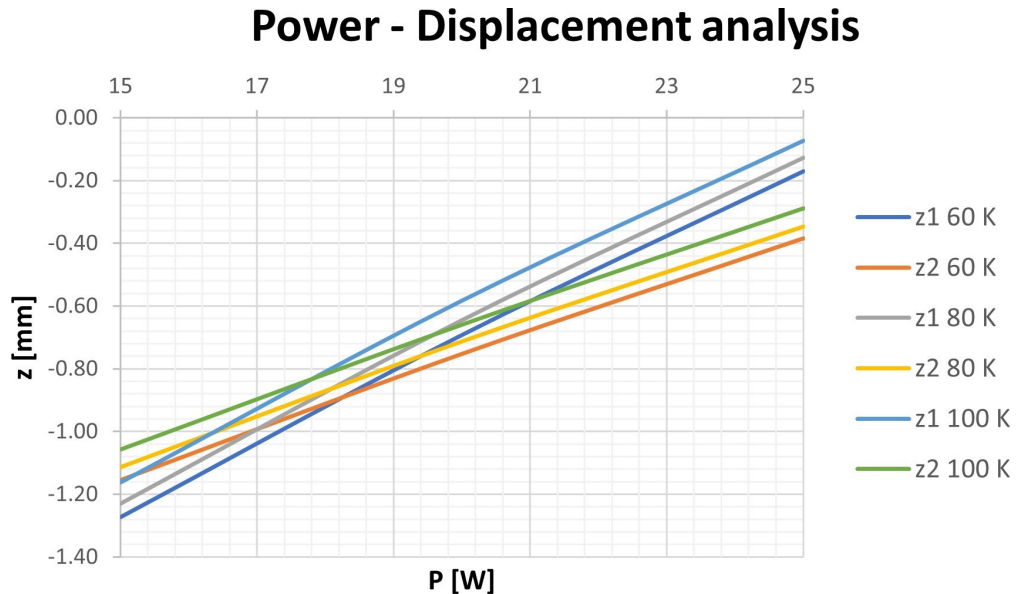


Figure 3.12: Plot of the vertical displacements as a function of Power and Temperature.

Each curve in the plot represents either the displacement of point 1 or 2 (Figure 3.10) at a fixed environment temperature, when the heating power supplied is increasing. It is clear that the results present non-linearities, indeed the experimental data do not lay on a straight line. The explanation must be found in the contact types used (i.e. frictionless is a not linear contact) and in the thermal radiation, which depends on the temperature to the fourth power. Another important aspect to highlight is the intersection between  $z_1$  and  $z_2$  at the same environment temperature. It represents the point where, at a specific power level (different for every couple of curves) the displacements of the higher H-BCAMs is equal to the one of the lower camera.

The next step in the sensitivity analysis is to find the power which must be provided to the two heaters. For this reason, a MATLAB script was made, whose work principle is simple: at a specific environment temperature, the script finds the power to supply to get the coordinates of the intersection cited above. In this way, the same correction must be applied to the two camera measurements during the data acquisition during the STC test.

Under nominal conditions, when the environment is at 80 K, the power to supply to the two film heaters is 18.07 W. The upper cameras plates will reach a temperature of  $T_1 = 292.05$  K, while the lower one will be at  $T_2 = 299.92$  K. The vertical displacements of the upper and lower adjustable plate is 0.862 mm. Results are reported in Figure 3.13 and Figure 3.14. As for the displacement along  $y$ , when both heaters are turned on, the results are negligible.

### 3. Spoke Test Cryostat

**C: Steady-State Thermal**  
G11 Temperature  
Type: Temperature  
Unit: K  
Time: 1 s  
2/20/2023 8:55 AM

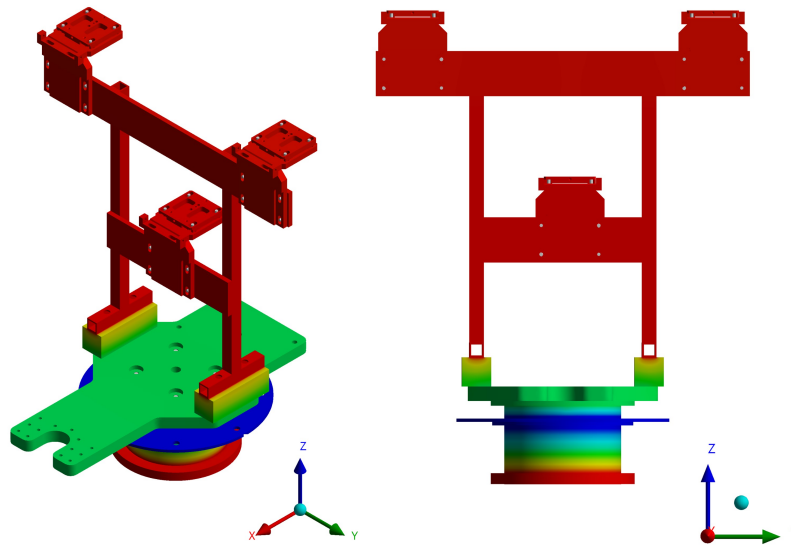
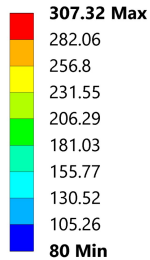


**Figure 3.13:** Result of the Steady-State Thermal Analysis: H-BCAMs stand temperature distribution when  $P = 18.07\text{ W}$  is applied.

**D: Static Structural**  
z displacement  
Type: Directional Deformation(Z Axis)  
Unit: mm  
Global Coordinate System  
Time: 2 s  
3/2/2023 7:14 AM

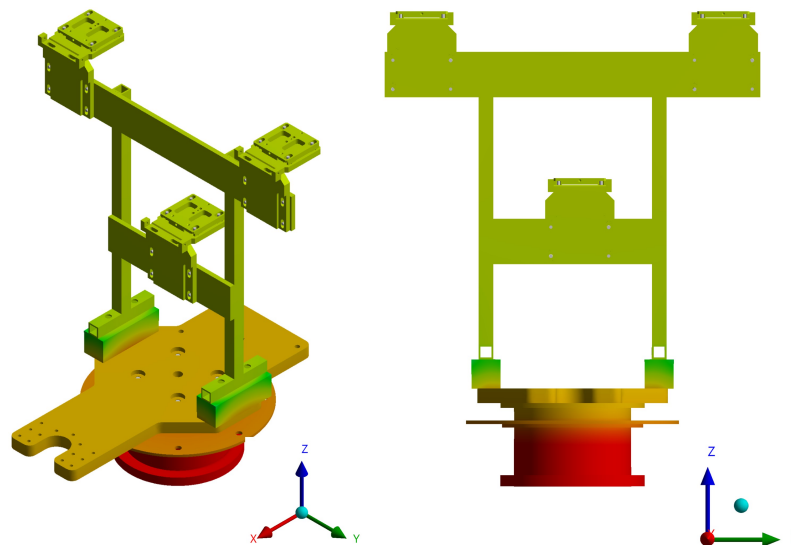
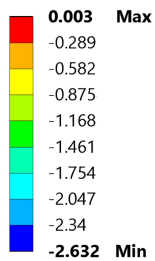


**Figure 3.14:** Results of the Static Structural Analysis: H-BCAMs stand displacements along  $z$  when  $P = 18.07\text{ W}$  is applied.

The results obtained are important because, by knowing how the stand is deforming under any circumstances, and the amount of power to supply, the H-BCAMs measurements during the cooldown test in the STC can be calibrated, thus improved. To measure the actual cavity displacements, the deformations of the stand (evaluated in the analysis) are subtracted from the H-BCAMs acquisitions.

### 3.1.6 Comparison between experimental test and numerical model

The test held in the STC was performed to check the cavity functionality under nominal working conditions. During the test, the cavity is gradually cooled down to 2 K, while the thermal shield reaches a temperature of 80 K. No target frames were installed on the cavity for this test. The H-BCAMs stand was instrumented with temperature sensors, placed as described in Figure 3.15, as well as with the film heaters and with one camera installed on the upper aluminum adjustable plate.

The cooldown process takes several days, during which both the heaters and the camera are turned off. Once the temperature inside the cryostat reaches steady-state conditions, the heaters are turned on to observe how the temperature of the stand changes under different powers supplied. This test is crucial to validate the H-BCAMs stand model: under steady-state conditions, for a given power, if the temperature recorded by the sensors is close to the one evaluated through the FEA, the model results to be reliable. A reliable thermal model outputs realistic displacements (assuming correct material properties), which is the main aim of the numerical simulation.

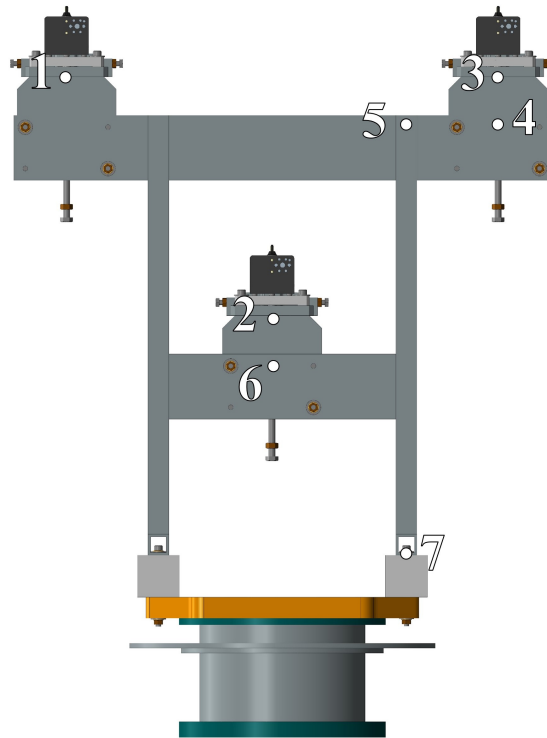


*Figure 3.15: Position of the temperature sensors on the aluminum stand for the test held in the STC.*

Two power levels were chosen to conduct the test: 15 W and 22.5 W. Considering that the evaluated power to supply to the two heaters, under nominal conditions, is equal to 18.07 W, the two values chosen should be enough to characterize the aluminum stand in

### 3. Spoke Test Cryostat

the working range of the heaters. The two powers are supplied without the stand reaching steady-state conditions, since it would take a considerable amount of time. Instead, the values read by the temperature sensors are compared with the ones given by the numerical analysis. To assess the reliability of the thermal model, the trend of the two curve must be the same, reaching similar final temperatures starting from the same boundary conditions.

With respect to the steady-state analysis reported in the previous paragraph, here the temperature of the thermal shield is 96 K, while the temperature of the cryostat stayed unchanged. The stand starting temperature is 128 K. These parameters come directly from the test held in the STC. The analysis performed is a transient thermal analysis, which aims at finding the temperature change during time. The simulation duration was set at 27000 seconds, which is slightly longer than the duration of the test of the two film heaters. In Figure 3.16, the results of sensor 2 are represented, while in Table 3.6 the final results are summarized.

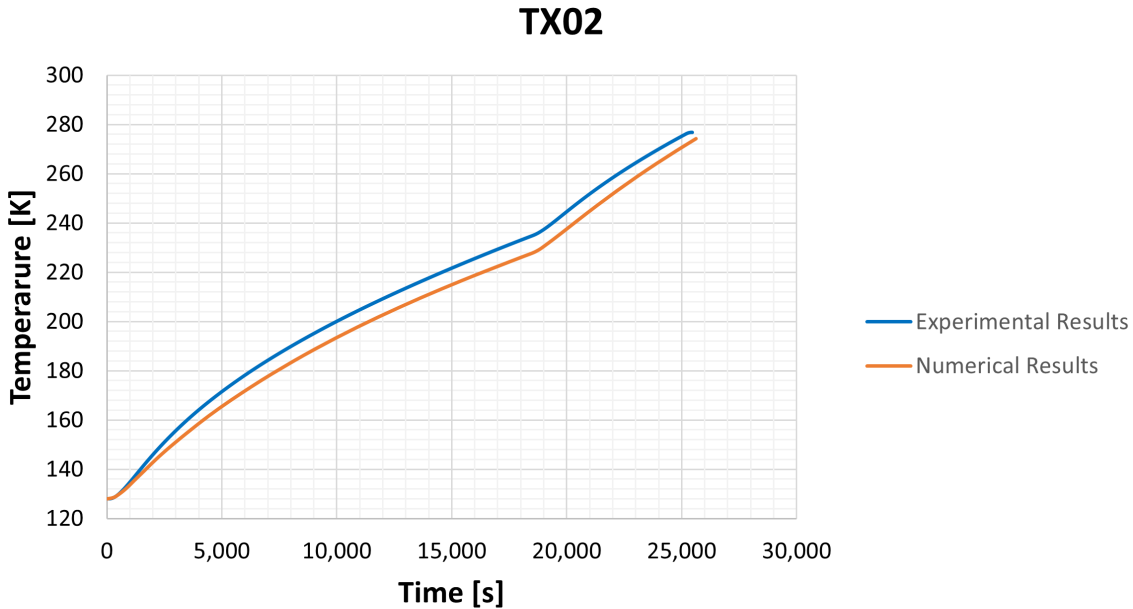


**Figure 3.16:** Comparison between numerical and experimental results.

**Table 3.6:** Comparison between numerical and experimental temperature, sensor 2.

	Numerical	Experimental
$T_{max}$ [K]	274.24	276.81

In each curve, two clear parts can be recognized in the plot: the first one, which goes from 0 to almost 19000 seconds, and the second one which goes until the end. These two have different angular coefficients, which depend on the power supplied to the heaters:

when it is higher, the temperature increases at an higher speed. this is the case for the second part of the curve.

It is clear that these two curves, experimental and numerical, present the same overall trend, meaning that the model built is behaving like the real stand. Moreover, the final temperature is difference is  $\Delta T = 2.57$  K, which is close enough to conclude that the model is reliable.

To further support this thesis, in Figure 3.17 the values read by sensor 3 are reported. In this case, the final temperature difference is only  $\Delta T = 1.13$  K. Differences in the angular coefficients of the two curves are probably linked to slightly different materials properties between the numerical model and the actual aluminum stand.

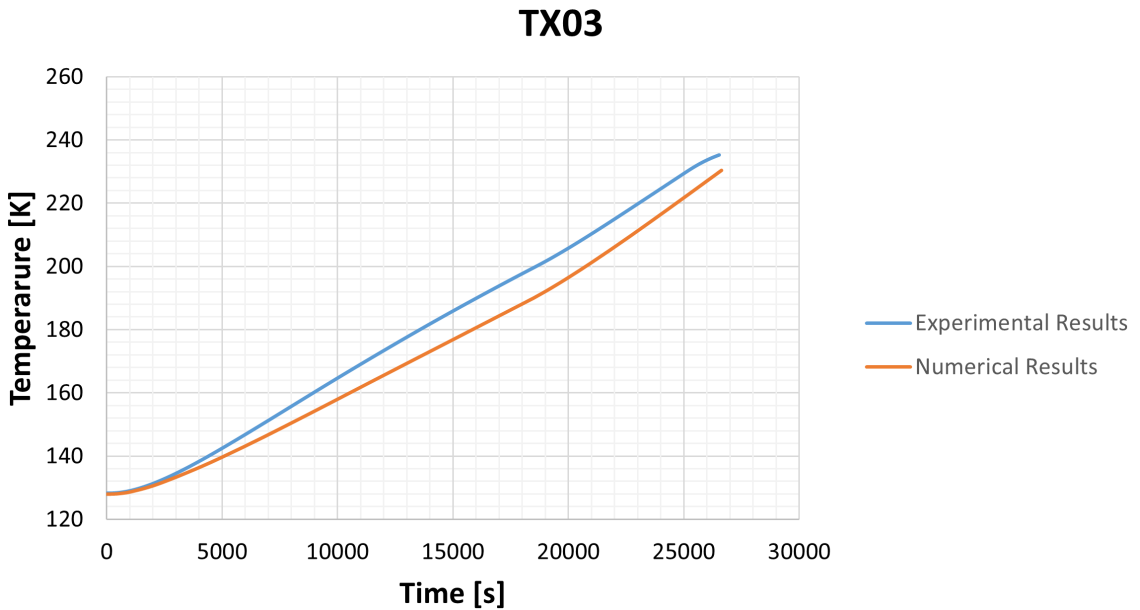


*Figure 3.17: Comparison between numerical and experimental results.*

*Table 3.7: Comparison between numerical and experimental temperature, sensor 3.*

	<b>Numerical</b>	<b>Experimental</b>
$T_{max}$ [K]	230.39	231.52

In conclusion, the numerical model has a behavior almost equal to the one of the actual aluminum stand. The results showed a good agreement between the numerical and experimental data, with only minor differences, ensuring that the solutions obtained, with all the previous analyses, are realistic.

### 3.2 SSR2 Cavity

The Single Spoke Resonator “type 2” (SSR2) cavity is a jacketed chamber which consists of two nested cryogenic pressure vessels operating at 2 K. The inner vessel is the bare superconducting cavity made from a 3.75 mm high purity niobium sheet, the outer one is the helium containment vessel made from a Titanium grade 2 sheet, a pure alpha alloy. This grade of Ti is not magnetic, has excellent mechanical properties and it resistant to oxidation. On the other hand, niobium is used for its superconductive properties under its critical temperature.

The two chambers are connected together by Electron-Beam (EB) and Tungsten Insert Gas (TIG) joints. The cavity operates at 325 MHz, and accelerates the H- in PIP-II SRF linac from 35 to 185 MeV. The particles are accelerated as they pass through the beam pipe, which extends from the cavity front flange to the back one thanks to an electromagnetic field generated inside. The cavity is not symmetric, neither along the longitudinal direction, nor along the transversal one.

The main components of the SSR2 cavity are presented in Figure 3.18, Figure 3.19 and Figure 3.20.

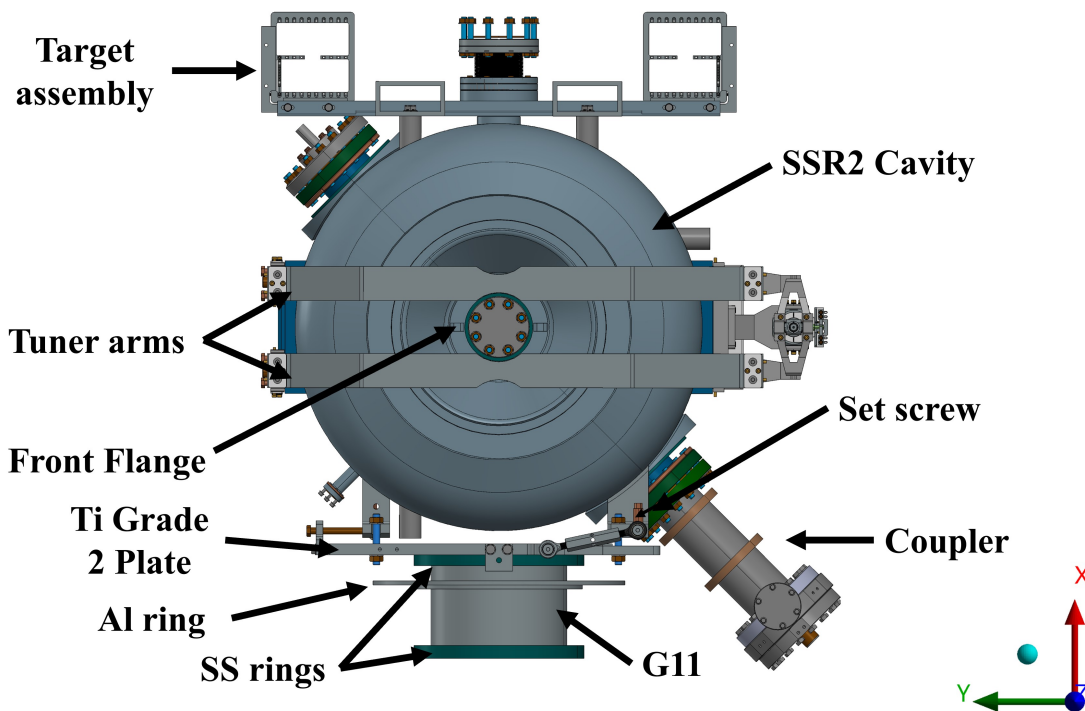


Figure 3.18: SSR2 Cavity main components, front view.

### 3. Spoke Test Cryostat

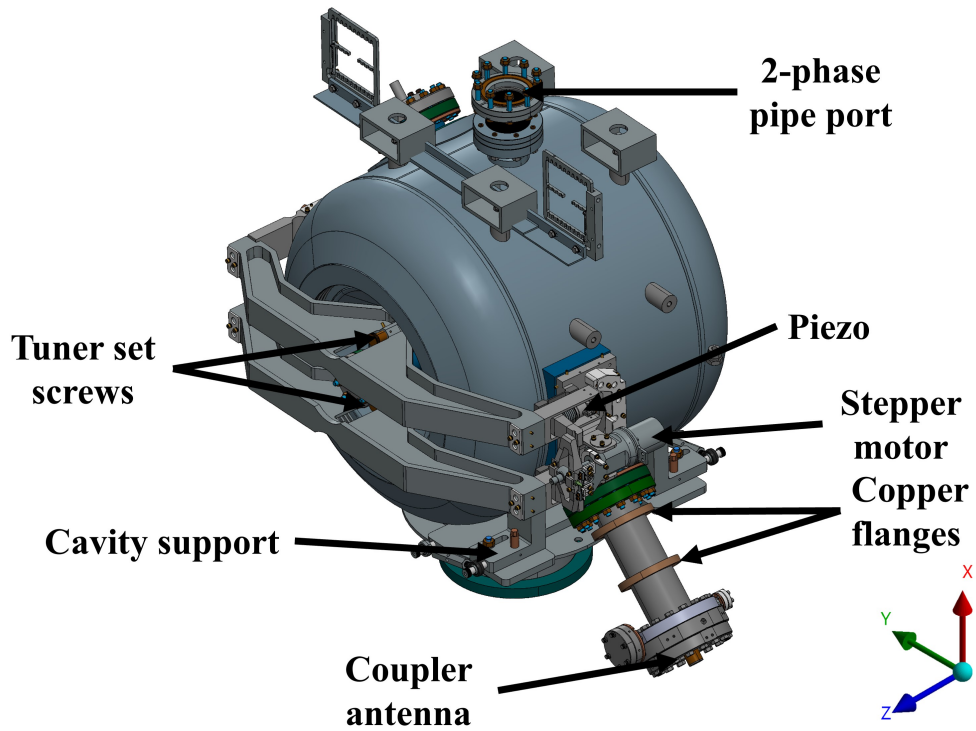


Figure 3.19: SSR2 Cavity main components, isometric view.

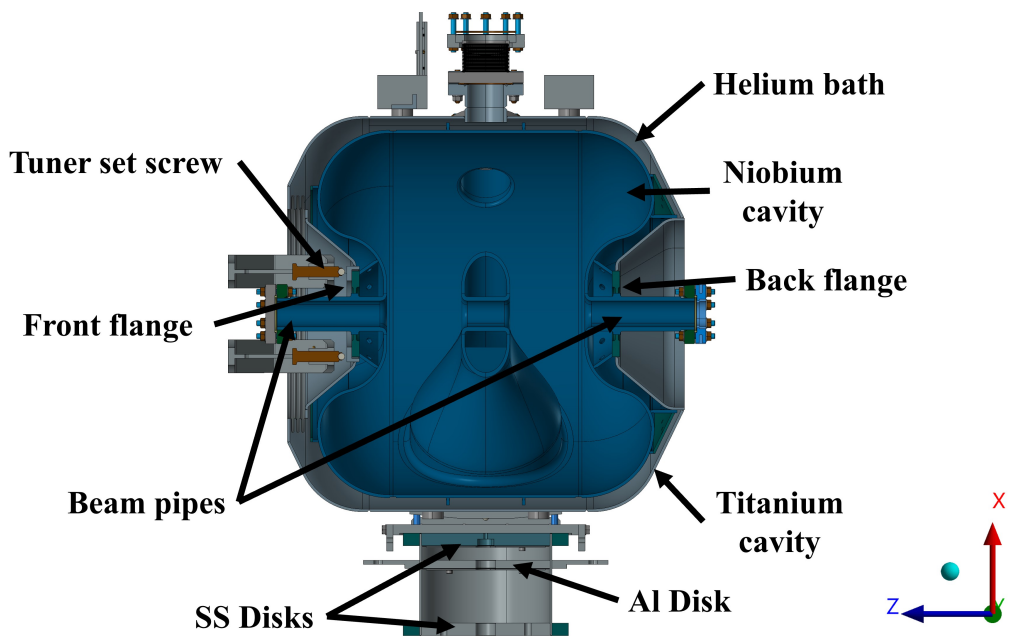


Figure 3.20: SSR2 Cavity main components, section view.

### 3. Spoke Test Cryostat

---

The tuner is a device used to tune the cavity frequency to the target one of operation at 2 K. It is a double lever system made of stainless steel alloy. It ensures both coarse and fine tuning, the former allows a range of adjustability of 135 kHz to take into account the frequency uncertainty due to the cooldown, while the latter has a range of 1 kHz to minimize (or possibly cancel) external noises known as microphonic, that disturb the resonant frequency of the cavity in operation. The tuner is composed of a main arm hinged at one end of the cavity, which is connected to the actuation system consisting of a stepper motor in series with two piezos, and a probe (set screw) which tunes the cavity by pushing an alumina sphere on the front flange.

The coupler is a RF device which allow energy to be exchanged with the modes of oscillation of the cavity. It is used to deliver the right RF power that creates the field which accelerates the particles. It is essentially made of an antenna inside a stainless steel cylinder, the latter is connected to the cavity and intercepts the 80 K thermal shield thanks to a copper flange. On the other end, it is connected to the cryostat thanks to a series of bellows on the coaxial line to allow for coupling adjustment and to accommodate cavity motion during cooldown and warm-up of the cryostat.

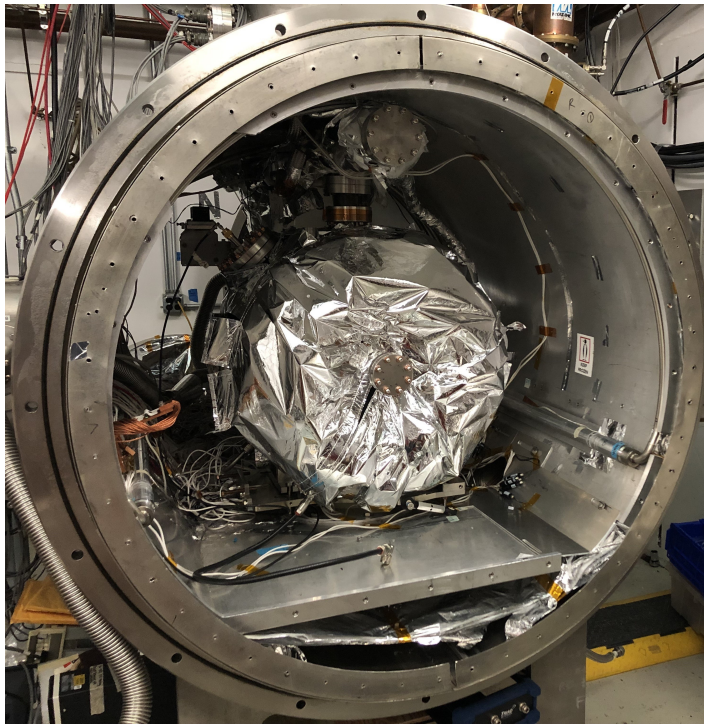


*Figure 3.21: SSR2 Cavity, wrapped around MLI, installed inside the STC.*

The cavity is placed on top of a titanium Grade 2 plate thanks to three silicon bronze set screws, which helps calibrating the cavity position in five degrees of freedom together with four brackets, which connect the cavity supports to the plate. The alignment

is performed using a laser tracker system, and when the cavity final position is found, it is fixed by tightening two bolts per side. The titanium plate is bolted on a support post equal to the one used for the H-BCAMs stand. Once installed, the cavity has no free degrees of freedom.

In the STC, the cavity meets the same conditions as the ones found during operation when integrated into the SSR2 beamline. The test aims at characterizing the cavity, as well as to ensure its functionality. The cavity is cooled down to 2 K to make it superconductive thanks to the helium bath, and tuned to its working frequency of 325 MHz using the tuner. Finally, its SRF performances are measured with a series of tests.

During cooldown, the cavity deformations along the three main axes are evaluated by the H-BCAMs mounted on the aluminum stand. The cavity is equipped with two target frames mounted on a support on the upper side, and one target mounted on the beam pipe thanks to a SS flange. Targets, supports and frames, made of Titanium grade 2 alloy, are equal to the ones described in Chapter 2.

#### 3.2.1 Model and Scope of the Analysis

Since the model has a large number of nodes (3633205), the contact between two touching surfaces was set as bonded to reduce the solving time. Because it reduces the accuracy of the analysis, it was used only for those surfaces in contact which have little to no influence on the results. This is the case for the targets and their survey base, the survey base and the bracket, the bracket and the bracket supports, and for all the flanges both fitted on the support post and on the coupler. The contact between the set screws and the cavity support is bonded as well to simulate the effect of tightening.

Where the influence of the contact type is much more important, it was modeled as frictionless. This is the case for the contact between the support post and the titanium plate supporting the cavity. The contact between the set screws and the titanium plate was set as no separation, which means that sliding without friction can occur, but the two surfaces cannot neither open nor close. As previously done in the stand analysis, every bolted connection was modeled with a mono-dimensional beam. The preload was evaluated using equation 3.1.

The aim of the analysis is to find the displacements of all the components in the assembly, and especially the ones of the H-BCAMs targets and the beamlines' axis. These results will be compared to the actual acquisitions made by the cameras during the test, and will be used to calibrate the Finite Element (FE) model for the SSR2 CM cooldown analysis.

### 3.2.2 Steady-State Thermal Analysis

The Steady-State thermal analysis' goal is to find the temperature distribution across all the assembly components. The boundary conditions set in the model are:

- The surfaces in contact with the cryostat have room temperature ( $T = 294.35$  K). These are the bottom surfaces of the support post, and the outer SS flange of the coupler.
- The aluminum ring shrink fitted on the support post in contact with the thermal shield has a temperature of 80 K. The same temperature is applied to the copper flange fitted on the coupler, since it is cooled down by copper thermal straps.
- The inner surface of the titanium cavity and the outer surface of the niobium one have a temperature of 2 K.
- On the stepper motor flange, the temperature set is 100 K.

As previously done for the H-BCAMs stand, thermal radiation towards the external environment was set for all the components, except for the internal ones of the support post. The values used are the ones of Table 3.3. The emissivity of all titanium bodies was set equal to  $\varepsilon = 0.30$ . Thermal coupling between the surfaces in contact was also set.

During the test in the STC, the cavity is wrapped around MLI plies to limit the thermal radiation towards the internal enclosure of the thermal shield. The MLI does not make the cavity perfectly insulated from the external environment, but it has a heat loss value of  $1.62 \times 10^{-6}$  W/mm<sup>2</sup>. Since this value is low, it is negligible and therefore it was not considered in the analysis. The boundary conditions applied are summarized in Figure 3.22, while the results of the steady-state thermal analysis are reported in Figure 3.23.

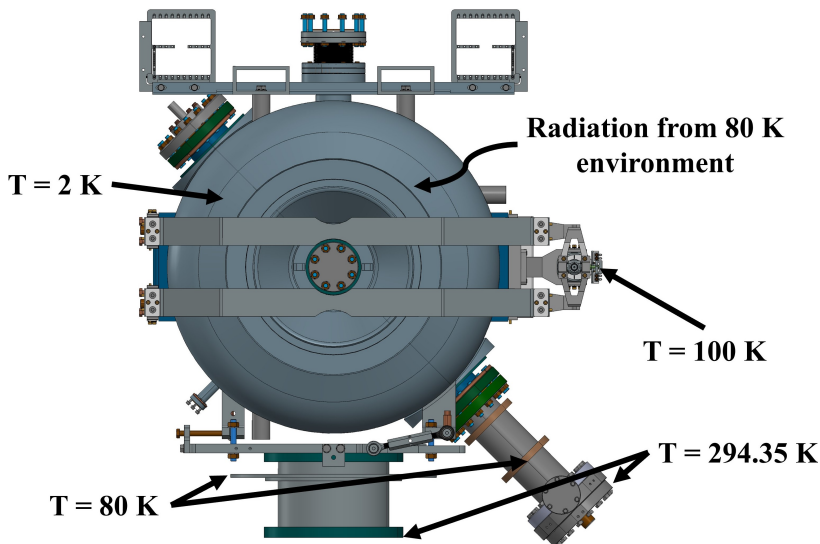
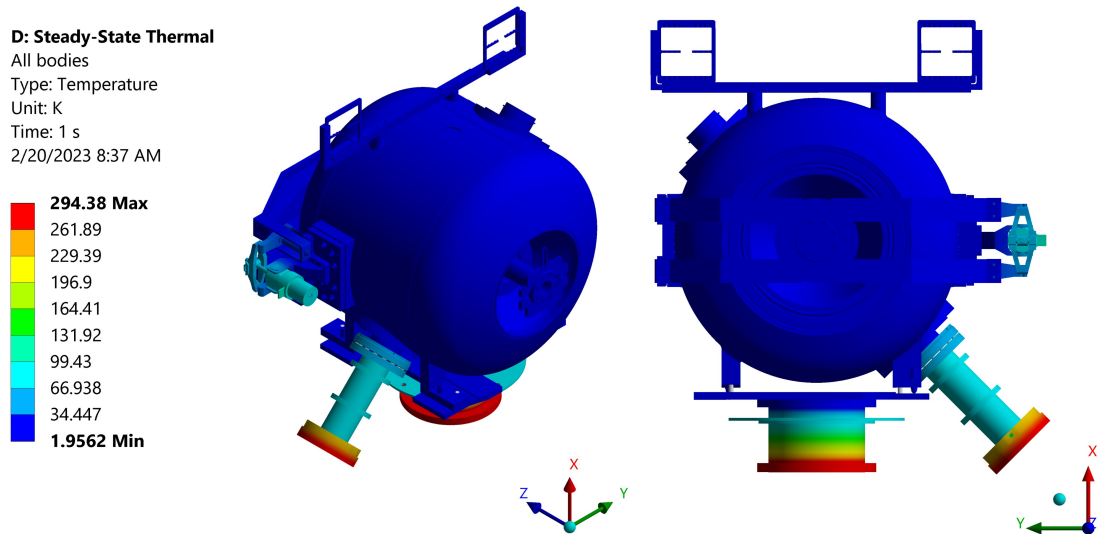


Figure 3.22: Boundary Conditions set for the steady-state thermal analysis.



*Figure 3.23: Results of the Steady-State Thermal Analysis: SSR2 cavity temperature distribution.*

Because of the helium bath, the cavity reaches an equilibrium temperature of 2 K. There is a clear thermal gradient between the aluminum ring shrink fitted and the bottom surfaces of the support post, and between the SS and copper flanges of the coupler.

### 3.2.3 Static Structural Analysis

The static structural analysis objective is to find the displacements of all the components in the assembly. The boundary conditions set in the model are the same as the ones used for the stand: the dof of the support post bottom surfaces are blocked with a fixed support. The solution coming from the steady-state thermal analysis is imported into the static structural to take into account the thermal shrinking due to the temperature difference from the initial one. Two case studies are reported: in the first one, only the steady-state thermal solution was loaded, while, in the second one, bolts pretensions were also taken into consideration. These two analyses are performed to observe the effect of tightening on the solution. In any case, during the installation inside the STC, the cavity is first tighten to the support post, and then aligned.

### 3.2.4 Case Study 1: Thermal Load

The displacements along  $x$ ,  $y$  and  $z$  are shown in Figure 3.24, and in Figure B.3 and Figure B.4 in the appendix.

### 3. Spoke Test Cryostat

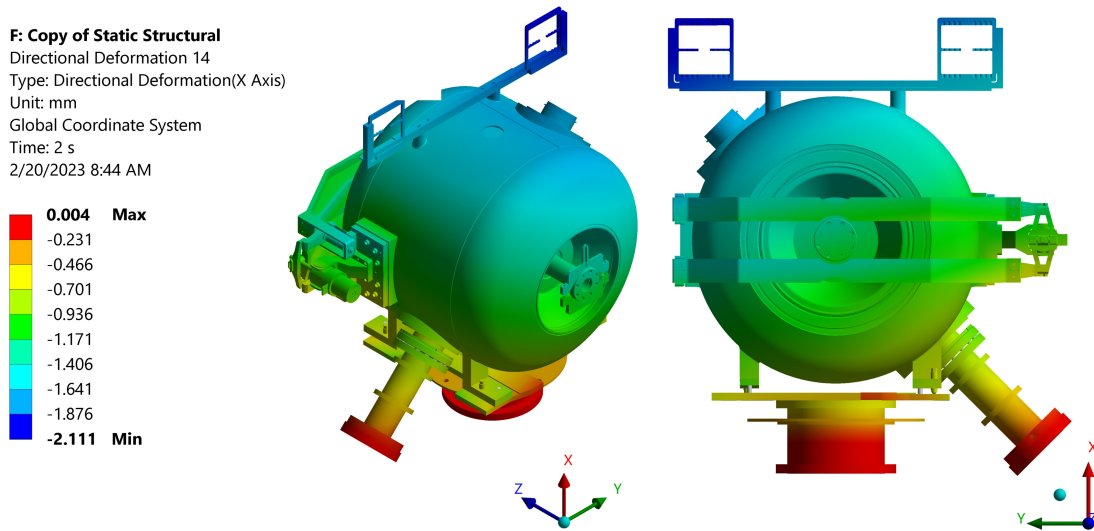


**Figure 3.24:** Results of the Static Structural Analysis: SSR2 cavity displacements along x.

To have a better understanding on how the whole assembly is deforming, the displacements of different points, showed in Figure 3.25, are here reported in Table 3.8.

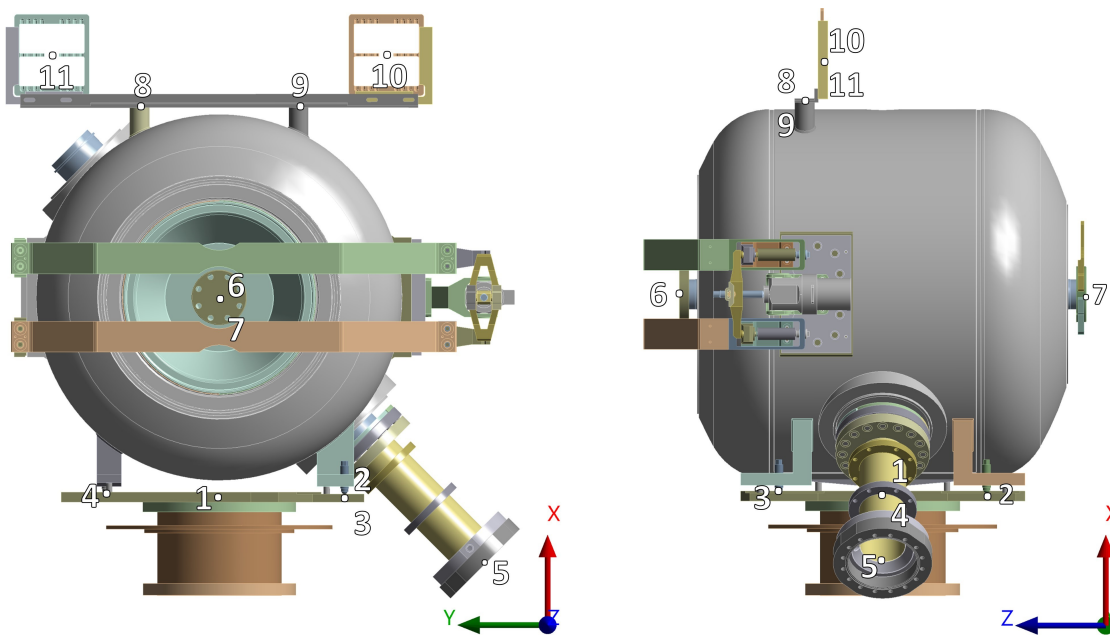


**Figure 3.25:** Reference points to evaluate the SSR2 cavity Static Structural analysis results.

As previously done for the H-BCAMs stand analysis, also in this case it is crucial to compare the numerical solution with the theoretical one evaluated using equation 3.2.

### 3. Spoke Test Cryostat

**Table 3.8:** Displacements along  $x$ ,  $y$  and  $z$  of the points reported in Figure 3.25, case study 1

Point	Displacement $x$ [mm]	Displacement $y$ [mm]	Displacement $z$ [mm]
1	-0.623	-0.015	$\approx 0$
2	-0.667	0.266	0.308
3	-0.671	0.385	-0.118
4	-0.618	-0.271	-0.058
5	-0.454	0.838	0.141
6	-1.075	-0.029	-0.468
7	-1.081	-0.162	0.485
8	-1.532	-0.259	-0.237
9	-1.583	0.136	-0.168
10	-1.768	0.317	-0.115
11	-1.635	-0.497	0.244

The main results are showed in Table 3.9. The titanium grade 2 plate has a low CTE at low temperatures, for this reason the resulting contraction was discarded. A difference lower than 0.150 mm exists between the two solutions, leading to highlight the goodness of fit of the model.

**Table 3.9:** Theoretical vertical displacements of the SSR2 cavity assembly.

Component	Displacement $\Delta x$ [mm]
Support Post	-0.727
Cavity	-0.955

By looking at the vertical displacements of point 10 and point 11, it is possible to state that the cavity is tilting about the  $z$  axis. This phenomenon can be explained by the shape of the cavity, indeed it does not have a symmetry plane. Geometric asymmetries lead to different displacements along  $x$  of the two target frames. The tilting angle can be evaluated by considering the difference in displacements and the distance between the two points.

$$\alpha = \arctan\left(\frac{\Delta x}{D}\right) = \arctan\left(\frac{0.133}{547}\right) = 0.014^\circ \quad (3.3)$$

Where:

- $\Delta x$  is the difference between the vertical displacement of point 10 and point 11.
- $D$  is the distance between the two points.

The resulting value is negligible and under the design constraint reported in Table 1.1.

Another important aspect to evaluate is the horizontal displacement of the tuner set screws pushing against the front flange. By changing their positions during the cooldown, the two set screws determine a different frequency of the cavity.

$$\Delta z = z_{flange} - z_{probe} = -0.191 - 0.700 = 0.509 \text{ mm} \quad (3.4)$$

Considering both the movements of the titanium flange and the silicon bronze probe, the cooldown shrink produces a relative horizontal consistent with the theoretical calculation using the CTE. This result is important because, this longitudinal contraction, can be compensated when the cavity is tuned to avoid possible frequency shift during operation.

### 3.2.5 Case Study 2: Thermal Load and Bolts Pretension

The second scenario taken into consideration is the case where both the bolts pretension and the thermal solution are used. The two types of loads were applied to the model at two different load steps to help the solution convergence and to have more accurate results. Bolts pretension was evaluated thanks to equation 3.1. Table 3.10 reports the displacements along  $x$ ,  $y$  and  $z$  using the same reference points of Figure 3.25.

*Table 3.10: Displacements along  $x$ ,  $y$  and  $z$  of the points reported in Figure 3.25, case study 2.*

Point	Displacement x [mm]	Displacement y [mm]	Displacement z [mm]
1	-0.582	-0.047	$\approx 0$
2	-0.659	0.198	0.403
3	-0.653	0.305	-0.280
4	-0.800	-0.257	-0.057
5	-0.150	0.788	0.129
6	-1.203	0.354	-0.478
7	-1.219	0.174	0.475
8	-1.761	-0.307	-0.251
9	-1.614	0.702	-0.187
10	-1.691	0.945	-0.138
11	-1.975	0.131	-0.257

As it happened in the previous case study, also here the cavity rotates about the  $z$  axis. By looking at the displacement along  $x$  of point 10 and 11, it is possible to evaluate

### 3. Spoke Test Cryostat

the rotation angle in the same way showed in equation 3.3. The result is reported in equation 3.5.

$$\alpha = \arctan\left(\frac{-0.284}{547}\right) = -0.030^\circ \quad (3.5)$$

The result which stands out is that the tilting happens in the other direction with respect to case study 1. This can be well explained by looking at the tilting moments created by the effect of the bolts preload on the two sides of the SSR2 cavity supports (Figure 3.26). The axial preload was evaluated starting from equation 3.1.

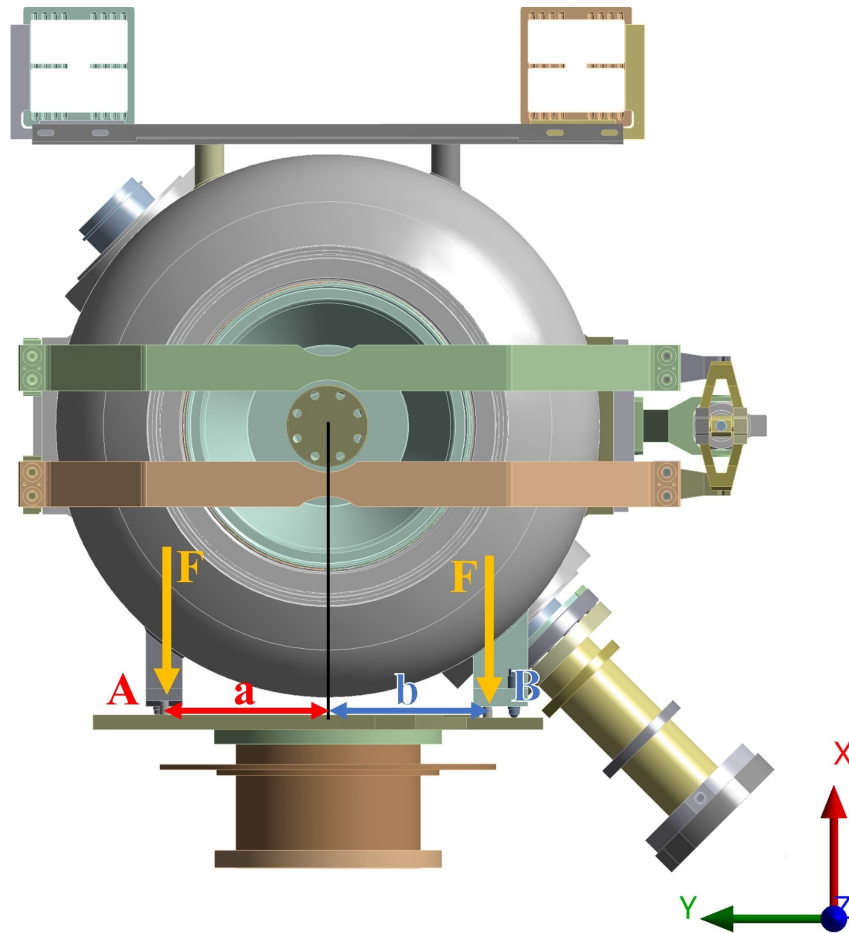


*Figure 3.26: Forces applied along x as a result of the bolts preload.*

The distance between the bolts housing on the left support and the cavity beamline center (**a**) is different from the one on the right (**b**), thus resulting in different tightening moments (since the axial force applied is the same). The full results of the preload calculations are available in Table 3.11, where the moments are evaluated about the *z* passing through the beampipe of the cavity.

### 3. Spoke Test Cryostat

---

**Table 3.11:** Tilting moments about  $z$  as a result of the preload applied.

F [N]	3000
a [mm]	175.78
b [mm]	179.72
$M_a$ [Nm]	545
$M_b$ [Nm]	557

In conclusion, the resulting tilting moment, caused by the preload, makes the cavity rotate about  $z$  in clockwise direction. As seen for the case study 1, the cavity presents geometrical asymmetries: during the cooldown, the cavity rotates anti-clockwise about  $z$ . The effect of this rotation leads to a re-alignment in the XZ plane: in the end, the tilting angle is lower than the previous result presented in equation 3.3. The final result is negligible since it is under the constraint limits presented in Table 1.1.

---

## Chapter 4

# Single Spoke Resonator "type 2" Cryomodule

The Single Spoke Resonator “type 2” cryomodule is a cryostat designed at Fermilab to contain Superconductive Radio Frequency (SRF) cavities. The whole point of a cryostat is to isolate the superconductive cavities from the room temperature environment. While cavities are designed to imprint energy to the particle beam, thus to accelerate them using an electromagnetic field, inside the cryomodule there are magnets, called solenoids, which are meant to keep the beam focused. Inside an SSR2 cryomodule there is a total of five cavities and three solenoids, which is called string assembly. Cavities and solenoids are interconnected by bellows, a flexible type of joint designed to compensate their displacements. The main components are reported in Figure 4.1 and Figure 4.2.

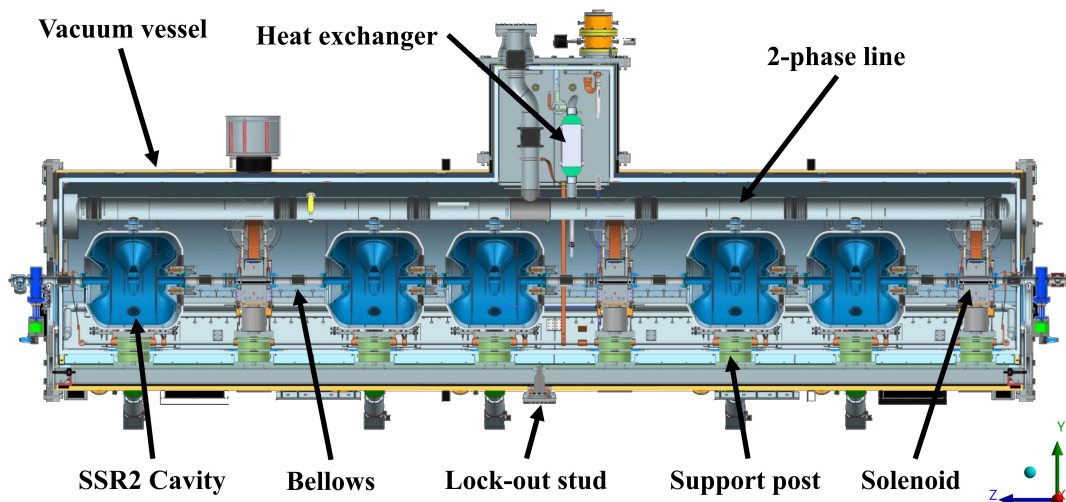


*Figure 4.1: SSR2 CM main components description, side view.*

#### 4. Single Spoke Resonator "type 2" Cryomodule

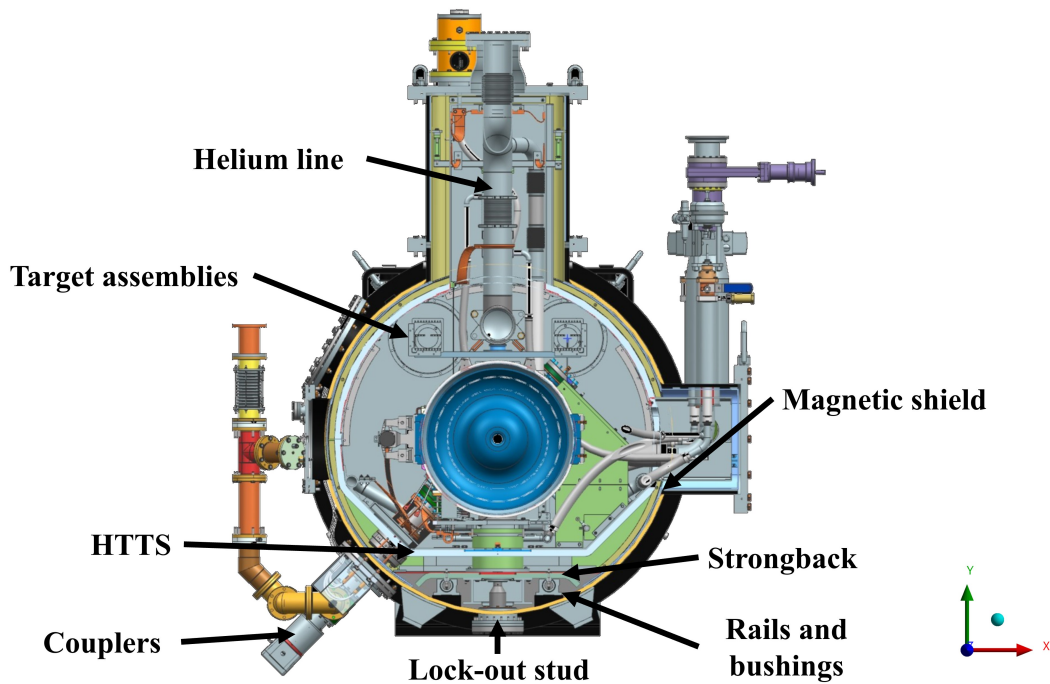


Figure 4.2: SSR2 CM main components description, front view.

Both cavities and solenoids sit on top of a titanium plate bolted on a support post, in a configuration similar to the one used for the test in the STC. This time, there are four stages of shrink fitted rings and disks, one more than the support post already described. Furthermore, to bring solenoids to the same height of the cavities beam pipe, a cylindrical titanium device is used. The SSR2 cryomodule is composed by different main components:

- Vacuum vessel.
- Strongback.
- High Temperature Thermal Shield (HTTS).
- Low Temperature Thermal Shield (LTTS).
- Magnetic shield.
- SSR2 cavities.
- Solenoids.
- Helium line.
- Heat exchanger.

#### 4. Single Spoke Resonator "type 2" Cryomodule

---

The vacuum vessel is the rigid enclosure which contains the coldmass, the strongback, the thermal and the magnetic shields and all the auxiliaries. Its main goal is to create a low-pressure environment to isolate the helium cooled environment from the room temperature one. Vacuum inside is created to eliminate convective heat transfer by gases. It also provides support for the strongback. The SSR2 vacuum vessel is made by a cylindrical shell in carbon steel (ASTM A-516) with a thickness of 12 mm, anchored to the floor with bottom supports and equipped with lugs for lifting purposes. All the components inside the CM operate in a moderate to high vacuum environment, which means that the minimum pressure inside the vacuum vessel can reach  $1 \times 10^{-6}$  Pa.

The strongback is a structure designed to support the coldmass. Instead of being connected to each other, cavities are installed on a common support frame (the strongback) which stays at room temperature thanks to thermal straps connected to the vacuum vessel. The goal is to minimize the axial movements of beamline components, as well as auxiliaries, during cooldown. As a result, components can contract together and stay aligned. Additionally, the bottom surfaces of the strongback is painted with an high emissivity paint to increase the radiation heat transfer to the vacuum vessel at room temperature. The strongback is made by different parts: a main aluminum Al-6061 extrusion, SS I-beams, carbon steel rails and bushing. The extrusion is bolted on the rails and stiffened by the stainless steel beams. Another important purpose of the strongback is to facilitate the assembly: the coldmass and the other components are first installed on it, and later the strongback is slid into the vacuum vessel and locked to the vessel with a central lock-out stud.

The High Temperature Thermal Shield have the same purpose as the one described for the test in the STC. It is made by aluminum alloy Al 1100-H12 for the sheets and aluminum alloy Al 6061 T6 for the extrusion (the pipe carrying the helium gas). The latter is welded on the HTTS sheets by means of finger welds, designed to reduce the stress during cooldown. The thermal shield can slide longitudinally (along  $z$ ) since it is simply supported by the aluminum rings shrink fitted on the support posts, while it is fully constrained only on one support (in central position). While the HTTS works in between 40 K and 65 K, the LTTS supply line has a temperature of 4.5 K and the return line is at 9 K. The aim of the LTTS is to provide low thermal intercepts for internal components, such as solenoids.

The connections between the two thermal shields, and the components which need to be cooled down, are ensured by thermal straps, devices used to couple thermically two parts which must be structurally divided. This de-couple is important to reduce stresses arising during the cooldown, which could damage fragile components. Thermal straps are usually made of high purity copper with an high thermal conductivity.

The magnetic shield goal is to reduce the influence of the earth magnetic field, as well as to attenuate the magnetic field generated by internal and external components of the cryomodule. The upper portion is bolted to a inner frame fixed on the vacuum vessel,

while the bottom one is bolted on the strongback. The magnetic shield material is a 3 mm thick 80% Nickel-Iron alloy sheet, which conforms to ASTM A753-85, Type 4.

Both cavities and solenoids are provided with reflective targets (four target frames per string component), whose position is recorded by four H-BCAMs in total, mounted on the two end flanges of the cryomodule. It is crucial to monitor their position throughout the entire assembly sequence, transportation, and testing qualification phase to check their alignment, which could compromise their functionality during operation. The targets have the same shape and dimensions as the ones already described.

Every internal component is installed and aligned at room temperature. The alignment is performed using a laser tracker: thanks to external fiducial points, the geometric axes of cavities and solenoids is identified and, if necessary, their position is mechanically changed during the assembly. The correct alignment is measured as the maximum deviation of the beam pipe from the reference orbit, which must not exceed an error better than 0.5 mm RMS.

During operation, the CM is cooled down to make the SSR2 cavities superconductive. The result is thermal shrinkage: misalignment can occur, which may reduce the ability of the CM to increase the particles' energy. Therefore, a prediction method must be implemented to compensate the displacements of the internal components of the CM. Finite Element Analyses (FEA) were performed to evaluate the corrections to be applied to the coldmass assembly during assembling at room temperature.

### 4.1 Model and Scope of the Analysis

The SSR2 CM model consists of several sub-assemblies: coldmass assembly, strongback, thermal shield and vacuum vessel. The goal of the analysis is to find the displacements of all the components, and especially of the beam line, so that corrections can be applied during the CM assembly at room temperature. Furthermore, it is also important to predict the targets displacements, to make a comparison between the Finite Element (FE) model and the experimental acquisitions of the H-BCAMs during the cryomodule cooldown (which is not planned yet because the CM is still under production).

Considering the analysis' aim, the vacuum vessel was not considered: indeed, only the thermal shrinkage was taken into account, which means no vacuum load. Moreover, only the lower portion of the thermal shield was modeled (the one in contact with the aluminum rings). Since the model is heavy, to cut the running time no radiations were considered, which means that the thermal shield upper portion has no influence neither on the thermal solution, nor on the structural one. Finally, no bellows or any type of joints were included because it is not in the analysis interest to consider their deformation.

Each support post is connected to the strongback with a bonded contact type, the same contact used to replicate the shrink fitting of rings and disks. As for the contact

between the HTTS and the support post aluminum rings, it was set as no separation for all of them, except for the second solenoid, where a bonded contact was used. The connections used for the cavities are equal to the ones used for the SSR2 cavity in the STC analysis. Solenoids share a similar configuration with cavities, resulting in the same contacts in the model.

## 4.2 Steady-State Thermal Analysis

The steady-state thermal analysis goal is to find the temperature distribution across all the components of the CM model. The boundary conditions (BCs) set in the model are:

- The temperature of the strongback was set at room temperature,  $T = 289$  K.
- The temperature of the internal surfaces of the titanium cavity and the external surfaces of the niobium one were set at  $T = 2$  K because of the helium bath.
- The temperature of the couplers external flange was set at room temperature because it is in contact with the vacuum vessel.
- The temperature of the first copper flange of the couplers was set considering the local temperature thermal shield extrusion. To take into account the thermal resistance caused by the copper thermal straps, a 10 K gradient was applied. As a results, this condition is not constant, but it changes for every cavity going from downstream the CM to upstream.
- The temperature of the second copper flange of the coupler was set at  $T = 15$  K. This is due to the temperature of the LTTS. For the same reason, the temperature of the higher support post ring was also set at 15 K.
- The temperature of the first aluminum ring of the support posts depends on the local temperature of the HTTS. This conditions is different for every cavity.
- The temperature of the solenoid beam pipe and lateral flanges were set at  $T = 4$  K. This is due to the thermal intercepts, with the LTTS, possible thanks to copper thermal straps.
- The thermal solution of the thermal shield was imported. This directly affects the temperature of the aluminum rings shrink fitted on both cavities and solenoids support post.

As previously done for the analysis of the SSR2 cavity in the STC, the thermal loss of the MLI was not considered. The boundary conditions applied are summarized in Figure 4.3. The thermal solution of the bottom surface of the HTTS can be appreciated in Figure 4.4, while the results of SSR2 steady-state thermal analysis can be appreciated in Figure 4.5.

#### 4. Single Spoke Resonator "type 2" Cryomodule

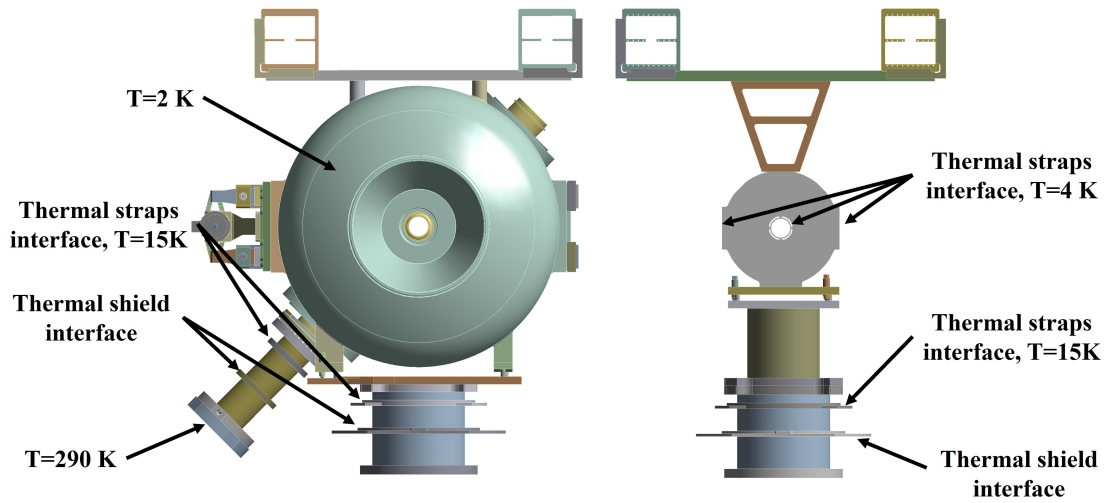


Figure 4.3: Boundary Conditions applied for the steady-state thermal analysis.

**K: Steady-State Thermal**  
 Temperature 20  
 Type: Temperature  
 Unit: K  
 Time: 1 s  
 2/18/2023 2:41 AM

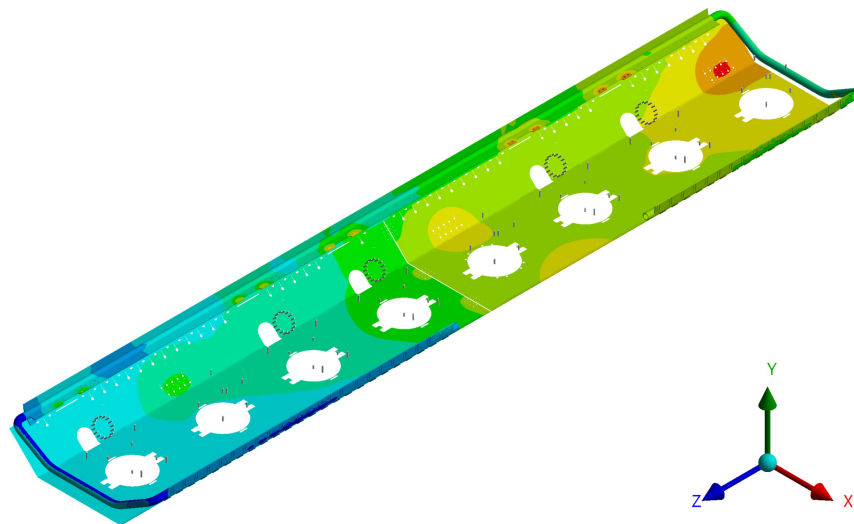
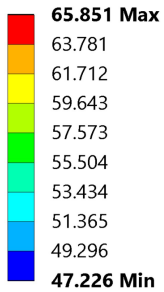


Figure 4.4: HTTS Steady-State Thermal Analysis solution.

The result of the steady-state thermal analysis of the HTTS, coming from another model, is imported into the SSR2 CM model to find the temperature distribution across all the components. The solution presented in Figure 4.4 depends on the liquid helium flowing into the extrusions: the mass flow rate of the supply line is  $\dot{m} = 3.5 \text{ g/s}$ .

## 4. Single Spoke Resonator "type 2" Cryomodule

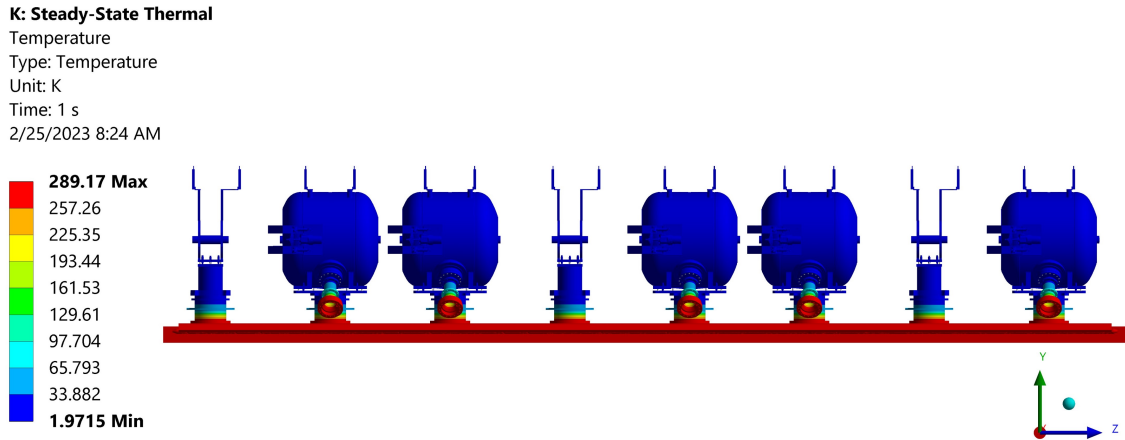


Figure 4.5: SSR2 CM Steady-State Thermal Analysis solution.

Because of the helium bath, the cavities average temperature sits at 2 K, while the average temperature of the solenoids is 4 K. Thermal gradients are clearly visible along the support posts due to thermal intercepts and the strongback at room temperature. The same comments can be made about the thermal gradients on the couplers.

### 4.3 Static Structural Analysis

The aim of the structural analysis is to find the displacements of the components in the assembly. Considering that the vacuum vessel was not included in the model, a way of locking the strongback is needed. Since the strongback can move along  $z$ , but cannot move along  $x$  and  $y$  because of bushing and rails, joints were used to constraint it to the ground. A joint is a type of constraint where it is possible to specify the free and the fixed degrees of freedom. As for the rotations, they were set as free, as it is in the real assembly. The joints need to be assigned to one surface in case the other end of it is fixed to the ground. In the model, the surfaces chosen are the outer surfaces of the carbon steel rails. The model is still under-constrained. In fact, in real life, the strongback is able to contract along  $z$ , but only because it is locked to the vessel with a central lock-out stud. A frictionless type of constraint was used in the central stud housing to fix the strongback.

Two case scenarios are studied to investigate the effect of the bolts preload, just like the analyses performed for the SSR2 cavity in the STC: in the first one, only the effect of the thermal shrinking is analyzed, so only the solution of the steady-state thermal analysis is loaded into the structural one, whereas, in the second one, also the bolts pretension is taken into consideration.

### 4.3.1 Case Study 1: Thermal Load

In the first Case Study, only the thermal load is imported from the steady-state analysis. The results of the static structural analysis along y are here reported in Figure 4.6 and Figure 4.7. All the remaining results are available in the appendix.

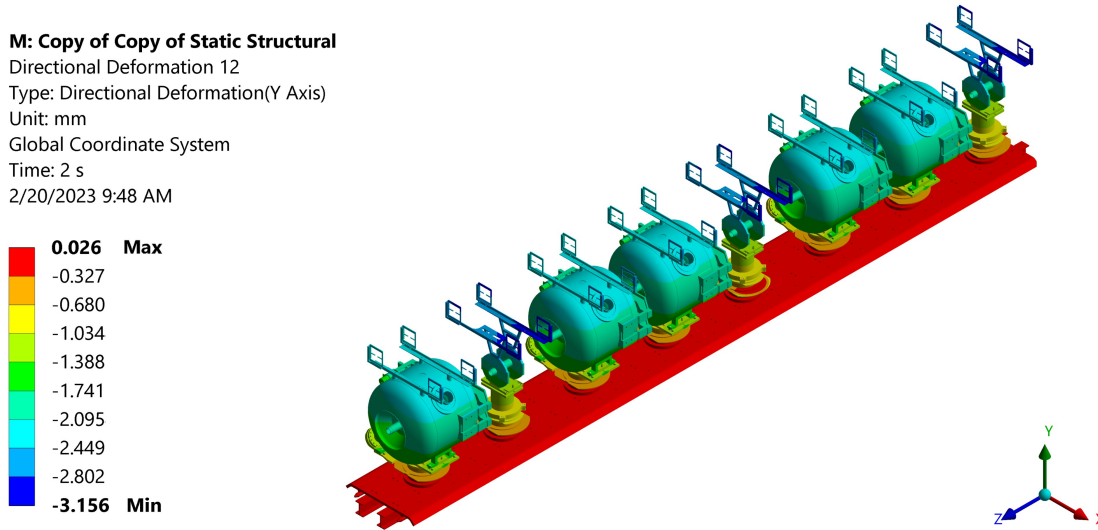


*Figure 4.6: Results of the Static Structural Analysis: SSR2 displacements along y, isometric view.*

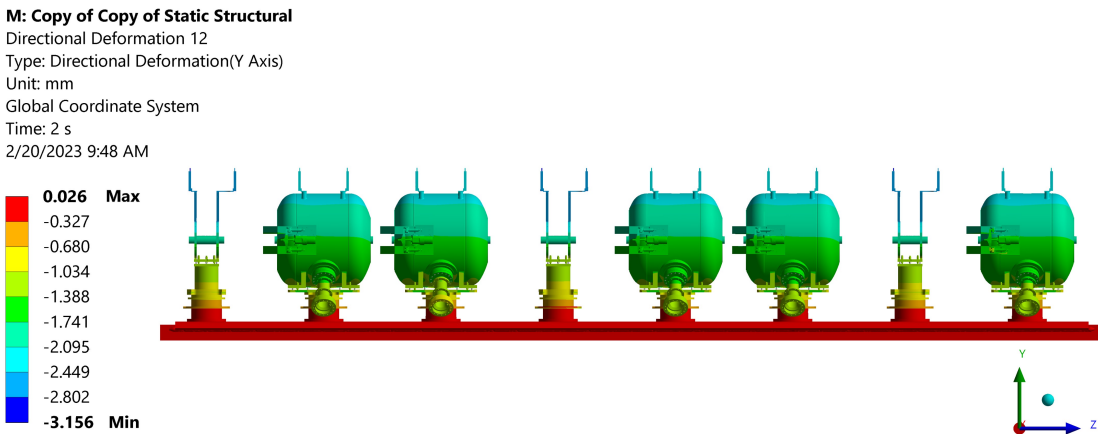


*Figure 4.7: Results of the Static Structural Analysis: SSR2 displacements along y, side view.*

To have a better understanding on what are the displacements of the whole assembly, some reference points were chosen and are visible in Figure 4.8 and Figure B.9 in the appendix, while their beamline displacement is reported on Table 4.1. The full numerical results are available on Table B.3 and Table B.2 in the appendix.

#### 4. Single Spoke Resonator "type 2" Cryomodule

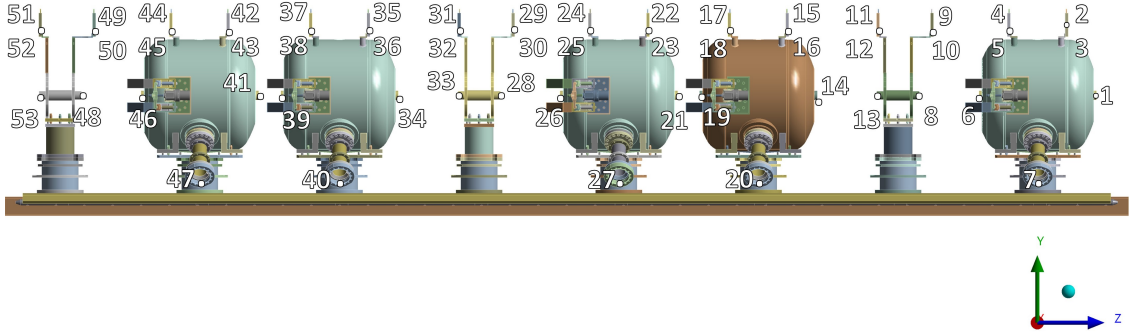


**Figure 4.8:** Reference points to evaluate the SSR2 cavity Static Structural analysis results, side view.

**Table 4.1:** Beamline displacements of the coldmass assembly, case study 1.

Point	Displacement y [mm]	Point	Displacement y [mm]
1	-1.583	6	-1.587
8	-1.822	13	-1.822
14	-1.584	19	-1.581
21	-1.575	26	-1.582
28	-1.800	33	-1.817
34	-1.579	39	-1.575
41	-1.584	46	-1.583
48	-1.816	53	-1.821

Firstly, the beamline displacements are different between cavities and solenoids, but consistent in each of these two categories from upstream to downstream. The average beamline displacement for cavities is  $-1.581$  mm, while the one of solenoids is  $-1.816$  mm. The numerical results are compared with calculations made using using equation 3.2. The main results are summarized in Table 4.2 for cavities and in Table 4.3 for solenoids. A difference lower than 0.100 mm exists both for cavities and solenoids, leading to conclude that the model is reliable and in line with the expected results.

**Table 4.2:** Theoretical vertical displacements of a cavity inside the SSR2 CM.

Component	Displacement $\Delta y$ [mm]
Support Post	-1.139
Cavity (beamline)	-0.445

**Table 4.3:** Theoretical vertical displacements of a solenoid inside the SSR2 CM.

Component	Displacement $\Delta y$ [mm]
Support Post	-1.134
Titanium Support	-0.109
Solenoid (beamline)	-0.524

Also in this Case Study, due to the cavity geometrical asymmetries, there is a tilting angle about  $z$  which can be evaluated in the same way showed in equation 3.3. The angle value is  $0.021^\circ$ , lower than the design constraint reported in Table 1.1, so it is negligible.

### 4.3.2 Case Study 2: Thermal Load and Bolts Pretension

In addition to the thermal load applied in case study 1, here also the bolts preload is added. The analysis is performed to observe its effect on the solution. The full results are reported in the appendix.

The cavity is behaving in the same way as described for Case Study 2 in the STC Chapter, with a final tilting angle is equal to  $0.021^\circ$ , under limits. By looking at the vertical displacements of point 9 and 10, it is possible to state that also the solenoids are tilting about  $z$ . The reason why it is happening is different from the cavity case, even though the effect is similar. Solenoid do not have geometrical asymmetries, nor a different distance between the point where the preload is applied and the center of the beampipe. Instead, they have a different number of bolts per side: two on one side, one on the other side. The resulting bending moment about  $z$  is therefore different for each side. The tilting angle is  $0.007^\circ$ , under constraint limits reported in Table 1.1.

## 4.4 Influence of the HTTS

One important factor to evaluate is the influence of the HTTS on the static structural solution. Since the temperature of the thermal shield is affected by the helium flowing in the extrusions, from upstream to downstream it is not constant. Therefore, it determines vertical displacements which are non-homogeneous along the CM. By recalling that the thermal shield sits on top of the aluminum rings shrink fitted on the supports posts, a variation of its temperature would directly result in a different thermal gradient on the composite G11 supports.

Two cases are studied: the difference in the vertical displacement of the beamline of cavity one and cavity five, and the same difference between solenoid one and solenoid three. Table 4.4 and Table 4.5 reports the results.

#### 4. Single Spoke Resonator "type 2" Cryomodule

**Table 4.4:** Influence of the HTTS on the vertical displacements of SSR2 cavities.

	Cavity 1	Cavity 5
$T_{\text{avg}}$ [K]	52.420	59.872
$y_{\text{avg}}$ [mm]	-1.585	-1.584

**Table 4.5:** Influence of the HTTS on the vertical displacements of SSR2 solenoids.

	Solenoid 1	Solenoid 3
$T_{\text{avg}}$ [K]	53.510	61.227
$y_{\text{avg}}$ [mm]	-1.822	-1.819

Where:

- $T_{\text{avg}}$  is the mean temperature of the aluminum ring in contact with the thermal shield.
- $y_{\text{avg}}$  is the average beamline vertical displacement between front and back flange.

It is clear that, even though there is temperature difference of around 7 K for both cases, the vertical displacement is almost identical. This can be explained by looking both at the expression to evaluate the contraction when a temperature difference is applied (equation 3.2), and at the CTE in the normal direction  $y$  of G11 reported in Figure 4.9.

### Linear CTE G11 Normal Direction

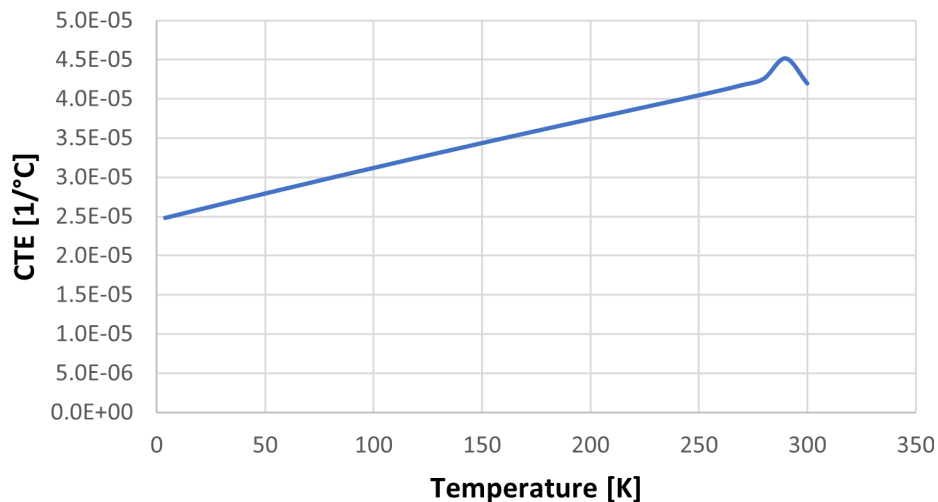


**Figure 4.9:** G11 Coefficient of Thermal Expansion, normal direction.

Since the temperature difference is negative (because the final temperature is lower

than the initial one), when the temperature  $T$  of the component increases, the magnitude of the value inside the brackets decreases, resulting in a lower contraction. At the same time, the CTE, for higher temperatures, has a greater value: when it increases, the contraction is larger. The sum of these two effects almost annihilate the effect of the thermal shield temperature. This is true for both cavities and solenoids.

## 4.5 Influence of the Helium Flow Rate

Another important influence to evaluate is how the helium flow rate in the extrusions affect the solution. The analyses performed until now took in consideration the nominal working conditions, but these could change during the cooldown process, thus resulting in different displacements of the components inside the CM.

The case study considered is a limit case, when the mass flow rate of helium passes from 3.5 g/s to 7 g/s, double the amount of the initial one. The aim is to observe how the system responds to such a change and how it affects the alignment of the string assembly. In Figure 4.10, the new thermal solution of the HTTS can be appreciated.

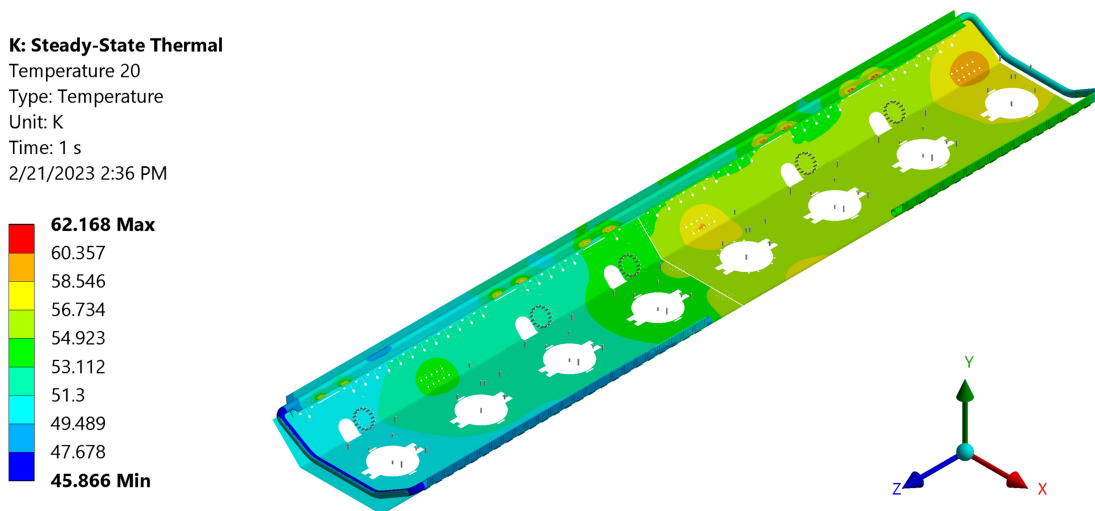


Figure 4.10: HTTS Steady-State Thermal Analysis solution,  $\dot{m} = 7$  g/s.

Recalling the temperature distribution of the HTTS in the nominal case showed in Figure 4.5, the  $\Delta T$  appreciated between the two solutions is 3 K. More helium circulating in the extrusions means an higher supply of cooling, leading to an overall lower temperature in the second case. Although this difference should induce a different alignment of cavities and solenoids in the CM, recalling the argument made in the previous paragraph, the vertical displacement of the beam pipe is essentially the same as the nominal case. Indeed, the difference appreciated is in the order of  $1 \times 10^{-3}$  mm, practically negligible.

---

## Chapter 5

# Prototype High Beta 650 Cryomodule Data Acquisition

The High Beta 650 MHz is a class of SRF cavities designed to accelerate the particles from 185 MeV, coming out from SSR cryomodules, to the final 800 MeV. The prototype HB650 (pHB650) cryomodule contains six jacketed cavities interconnected by bellows, each one with their own coupler, tuner, local magnetic shield and connection to the two-phase pipe. The cryomodule shares the same design concepts with SSR2 one: both have a room temperature strongback, and the cryogenic layout is identical, even if the configuration of cavities and solenoids is different.

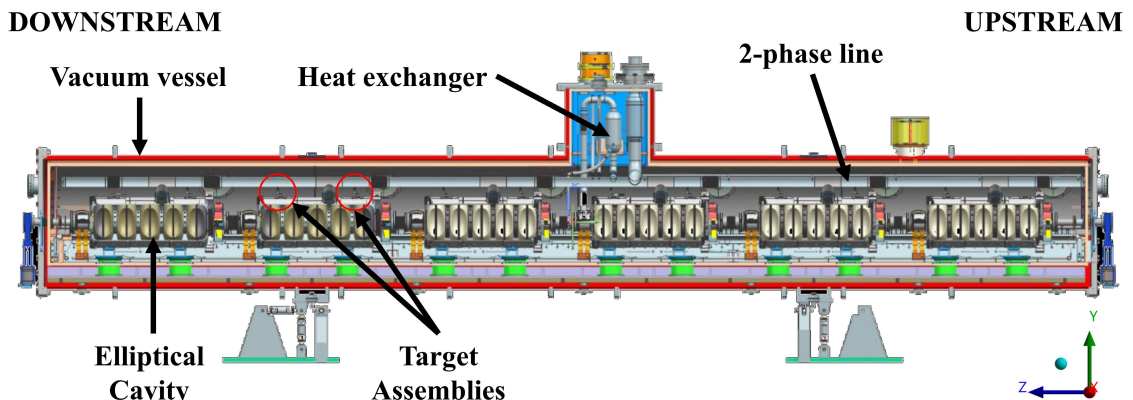


*Figure 5.1: pHB650 CM main components description, side view.*

Each cavity is equipped with four H-BCAMs target frames, two at front and two at the rear of the cavity. The hardware used to mount the targets is the same as the one described for the test in the STC, and in total there are 24 targets. The cryomodule is

provided with four H-BCAMs of the same type explained in Chapter 2, with the purpose of monitoring the targets displacements throughout the all the assembling phases. The cryomodule assembly is divided into different phases which must be monitored:

- The string assembly, which consists of cavities, two-phase pipes and bellows, is built along with the strongback assembly.
- The string assembly is lifted on to the strongback one. With the installation of the thermal shield, the coldmass assembly is then completed.
- The coldmass assembly is inserted into the vacuum vessel by sliding it into the CM.



*Figure 5.2: Insertion of the coldmass assembly into the pHB650 vacuum vessel.*

The cameras are also used to trace the targets throughout transportation and testing. Each H-BCAM is facing twelve targets and the camera on the other side of the cryomodule.

## 5.1 H-BCAMs and Targets Installation

Before proceeding with the acquisition, targets need to be installed along with the H-BCAMs, and a proper calibration of both is necessary. The H-BCAMs were installed on an aluminum stand whose position was fixed to the ground. Each couple of H-BCAMs sits on top of an adjustable aluminum plate, which can be moved along the three main axes and rotated about the vertical axis by tightening or untightening some screws. The targets frames were placed on the upper cavity side, in correspondence of the cavity support, and they were bolted on them. Once all the hardware was installed, the H-BCAMs were

## 5. Prototype High Beta 650 Cryomodule Data Acquisition

connected to the main acquisition driver, which was later connected to a laptop PC with the acquisition software provided by the manufacturer.

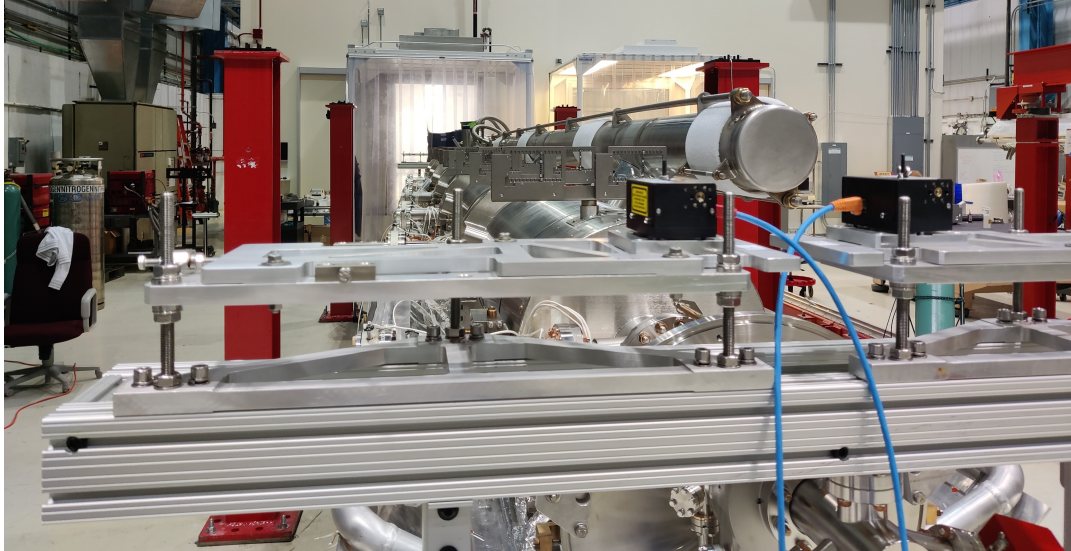


*Figure 5.3: H-BCAMs and targets installed on the pHB650 string assembly.*

To make the acquisition more reliable, at each iteration the software looks for targets in a specific rectangle of the visible space of the CCD sensor, which must be manually specified in the acquisition script. The position of both the H-BCAMs and targets was adjusted so that each camera could clearly identify the first six targets in its view and the camera on the opposite side of the cryomodule. In Figure 5.5, it is reported an example of the view field of each camera. As part of the calibration, all glass spheres and all H-BCAMs lasers were carefully cleaned using an air duster can. The scheme summarizing the name and positions of both targets and cameras can be appreciated in Figure 5.4.

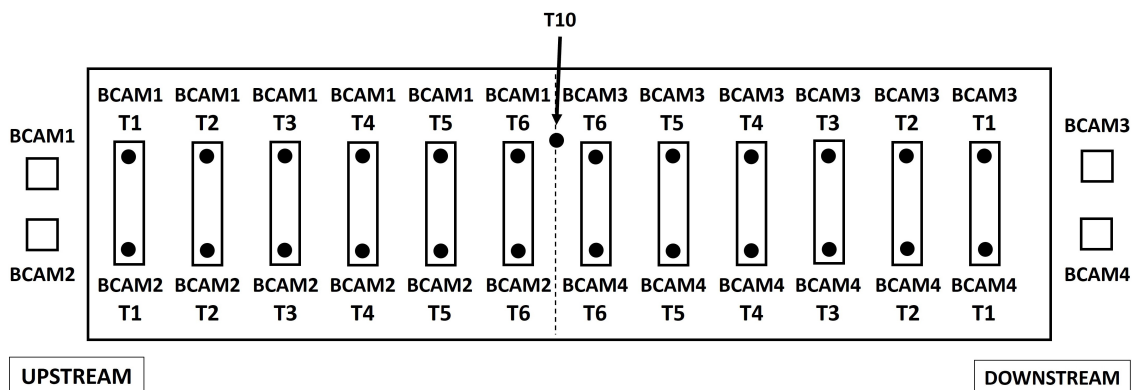


*Figure 5.4: Scheme representing the position and name of both H-BCAMs and targets installed on pHB650.*

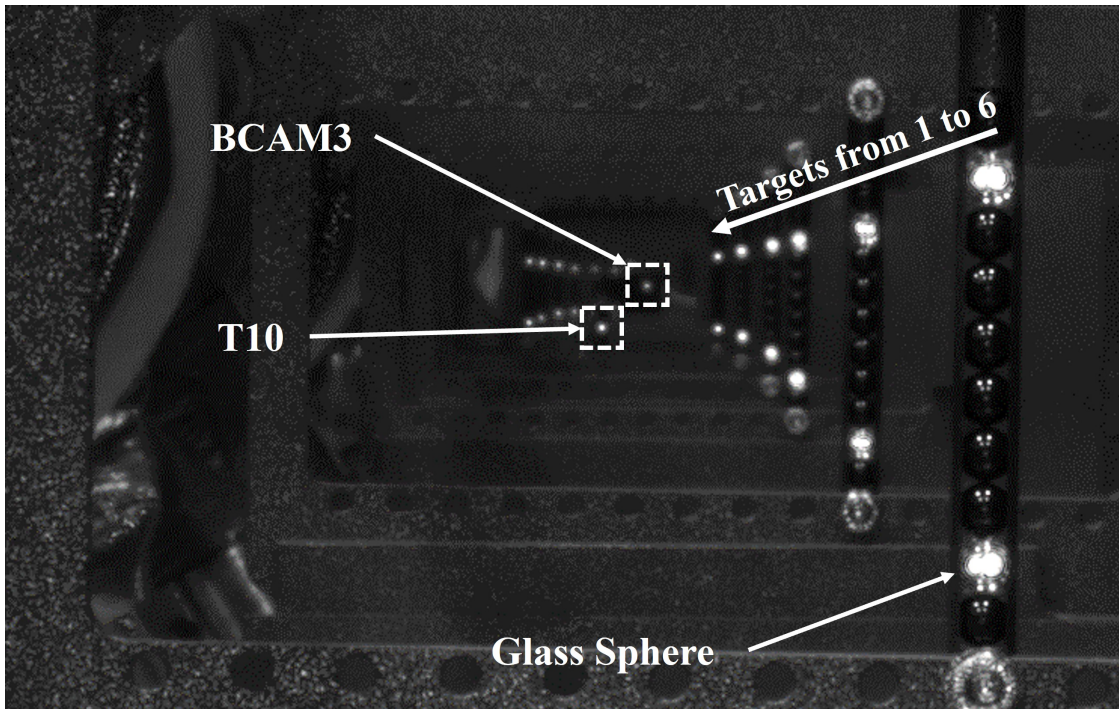


*Figure 5.5: View field of H-BCAM1. The first six targets, as well as H-BCAM3 on the opposite side, are clearly visible.*

## 5.2 MATLAB Script

As already mentioned above, the LWDAQ® software takes in input an acquisition file, and displays in output a text file containing all the data acquired from the targets. Each H-BCAM looks for two different types of targets: the glass spheres mounted on the target frames and the LED light of the camera placed on the opposite side of the cryomodule. For each of them, several parameters are recorded. The main ones are:

- Position  $x$  and position  $y$ , in pixels, of the target center (glass sphere or camera flash).
- Number of pixels which reflects the light.
- Peak intensity, which is the amount of light reflected captured by the sensor.

The parameters, recorded by the software, are used in the MATLAB script to clean the acquisition from outliers, which are incorrect recorded points. There are many reasons why these points are falsely acquired. Firstly, since the cryomodule's components are mainly made of metal, they are highly reflective, and therefore they could negatively influence the acquisition. When the cameras are flashing their lasers on the targets, the sensor could detect the peak intensity somewhere else far from the glass spheres. Moreover, particles of dust or dirt laid on the lens or on the spheres could make the target

detection harder. Even though all the titanium surfaces of the targets are anodized, which make their reflection coefficient lower, and even though a strong attention was used for cleaning the components, a proper script is essential to make the acquisition more reliable.

The MATLAB code takes in input the whole text file containing all the acquisitions, it then organizes them into a matrix depending on the target number each camera is looking at and which laser the camera is using (e.g. HBCAM 1 looking at target 1 using laser 3). This matrix is then loaded into a cleaning function, which analyses every point recorded and decides whether or not it must be saved or rejected. The cleaning function is essentially a loop, which scans the matrix looking for outliers. It reads one point at a time, performs several checks and saves it in a new matrix. If the point acquired does not respect the conditions of the cleaning function, it is considered as an outliers and it is replaced by the previous point. The working principle of the function can be appreciated in Figure 5.6.

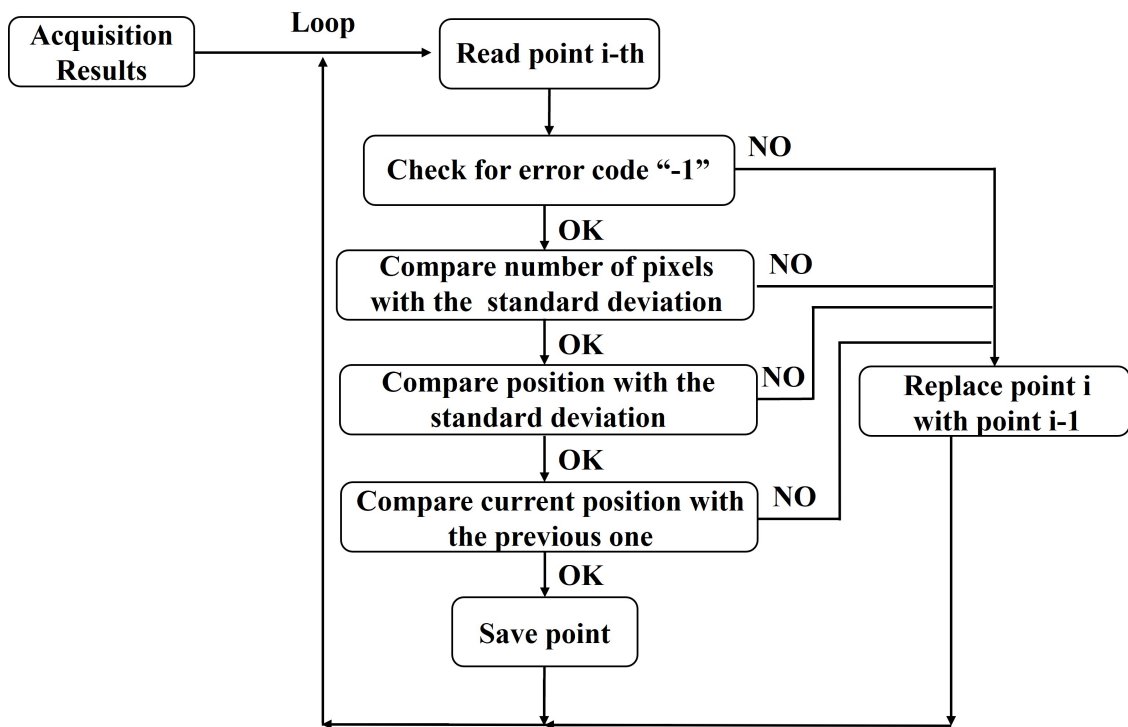


Figure 5.6: Data cleaning function working scheme.

The checks the cleaning function performs are:

- Error code “-1”: if something went wrong during the acquisition, the H-BCAMs would output the number “-1” instead of the positions, in pixels, of the glass spheres.
- Number of pixels: as said above, the cameras record the number of pixels which

reflects the light. If this number is too high with respect to the mean value, it probably means that, not only the glass spheres, but also another object is reflecting the light.

- Position: each position recorded is the average between ten consecutive acquisitions made by the BCAM. If the standard deviation of the position (of these ten acquisitions) is too distant from the mean value, it means that another target is being traced instead of the correct one.
- Current position: the last check compares the position of the current point with the position of the previous point. If two consecutive points are too far one another, but the last point recorded still respects all the other checks, something went wrong during the acquisition.

### 5.3 Reference Data Acquisition

The first acquisition was made to have a reference to evaluate the targets displacement for the other phases of the assembly. Data were recorded when the string assembly was already mounted on top of the strongback one, without the thermal shield, as showed in Figure 5.3. This acquisition was also used to properly tune the MATLAB code to detect the outliers. It is a static acquisition, meaning that the cryomodule is fixed and no process is going on.

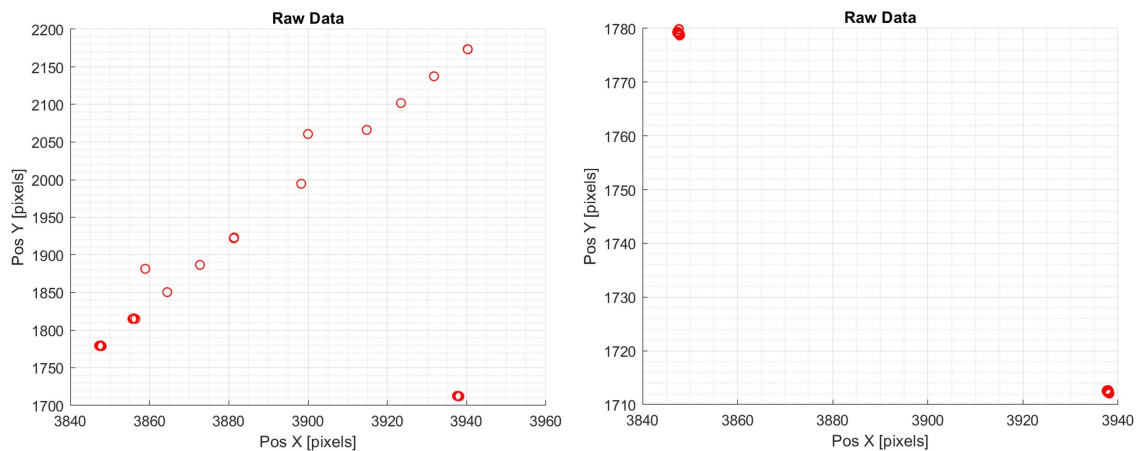


**Figure 5.7:** On the left, raw data acquired from the H-BCAM. On the right, the same data after the cleaning function has deleted the outliers.

To increase the accuracy of the measurements, repeated acquisitions were made for a total of one hour. The acquisition file was then loaded into the MATLAB script with the aim of finding the targets position in pixels. To achieve this result, the cleaning function was modified with the right flags: boundary values that, if not respected, would discard the current point in the loop. As it is showed in the Figure 5.7, the cleaning function tuning

was performed successfully. The camera was looking for two glass spheres, so two points needed to be recognized, but instead something prevented the H-BCAM from acquiring only those two positions. The cleaning function discarded all the values wrongly saved, leaving only the correct targets positions.

## 5.4 Insertion Data Acquisition

The final stage of the assembly consists in inserting the coldmass assembly into the cryomodule vacuum vessel. The coldmass is placed on a rail system, which can be leveled by hydraulic adjustable supports anchored to the floor, and it is later slid into the cryomodule and fixed to the strongback already installed. The insertion can be appreciated in Figure 5.2.

Alignment of the coldmass assembly, as well as of the strongback one, is performed before the insertion by a laser tracker. Therefore, it is crucial to check the targets position, which means checking if the cavities have moved during this phase of the assembling. The two stands, with the H-BCAMs installed on, were moved away from the two ends of the cryomodule to allow the assembly. After the insertion, they were placed back on their previous position and their alignment, with respect to the vacuum vessel, was checked with a laser tracker. The acquisition respected the same path described above, with a total duration of 48 hours. The main results are showed in Figure 5.8 and Figure 5.9.

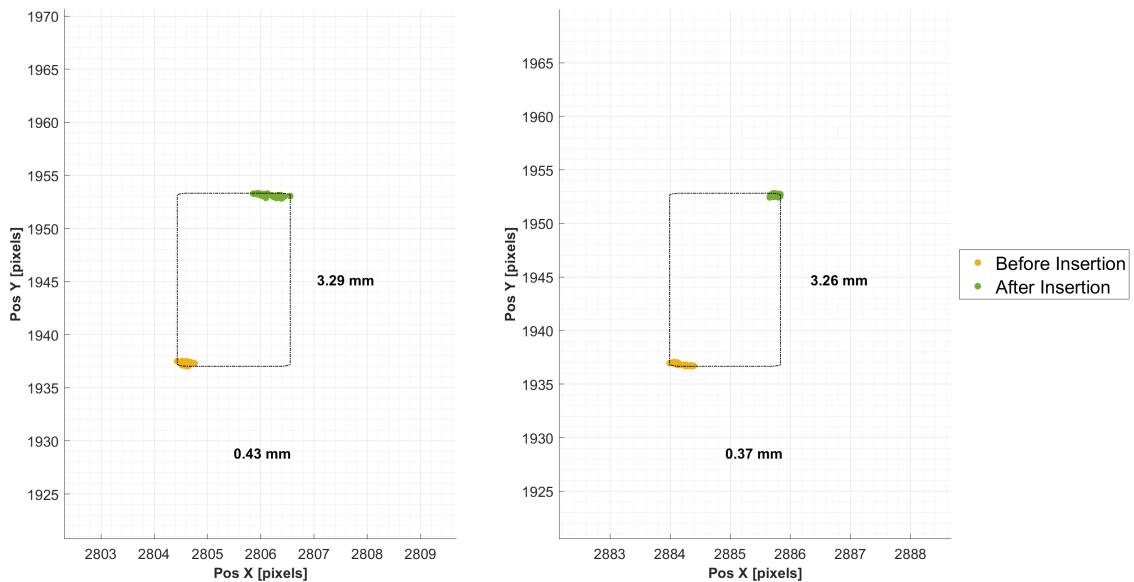


Figure 5.8: BCAM3 displacement after the insertion. Acquisition made by BCAM1 with both laser diodes.

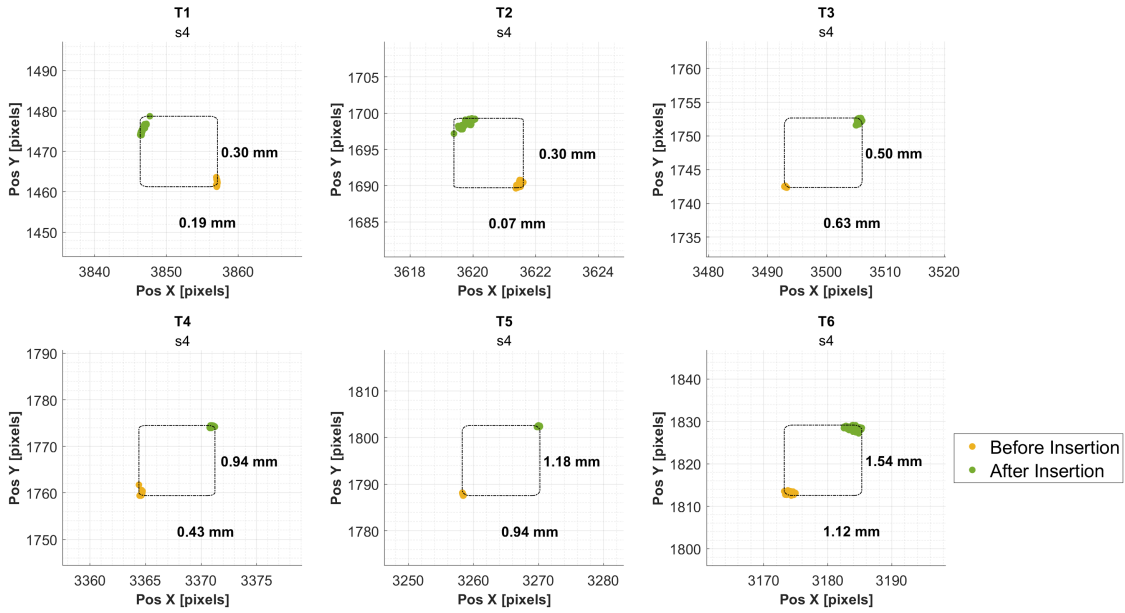


Figure 5.9: BCAM1 first six targets displacements after the insertion, with both laser diodes.

By looking at the results, it is clear that either the targets or the H-BCAMs have shifted away from the position they had before the insertion. In fact, the average displacement is higher than the one expected before the test (in the order of  $1 \times 10^{-2}$  mm), both in the vertical and horizontal direction. Considering the assembly process, it is unlikely that the cavities have shifted of this magnitude during the insertion of the coldmass assembly into the CM. The source of error is probably linked to the H-BCAMs aluminum stand. As a matter of facts, no mechanical connection links the stand to the cryomodule during the assembly phases, but the stand position is manually adjusted starting from the laser tracker measurements. Even though this measuring system is reliable and can reach an accuracy of 0.025 mm over a distance of several meters, the relative position between the stand and the vacuum vessel is not fixed, as it lacks of repeatability. For this reason, no conclusive comments can be drawn from this data acquisition.

## 5.5 Transport Data Acquisition

The next phase of the assembly is the transport. The pHB650 cryomodule was assembled at MP9, a workshop with the largest cleanroom at Fermilab. Once the assembly is completed, it is transported to the Cryomodule Test Facility (CMTF). Misalignment between internal components could occur as a consequence of the transport vibrations. As a result, the data acquisition is important to check the cavities position before and after

this operation. After the insertion of the coldmass assembly into the cryomodule, the H-BCAMs were positioned on their permanent plates, which were installed and fixed on the two end flanges of the cryomodule (Figure 5.10). Their position was calibrated again to make sure each camera can clearly identify the first six targets and the opposite H-BCAM. Each camera can look inside the CM thanks to view ports in the end flanges, and MLI is wrapped around to limit heat dispersion. The data acquisition aims at comparing the target displacements before and after the cryomodule transport. The benchmark is the insertion acquisition. The main results can be appreciated in Figure 5.11 and Figure 5.12.

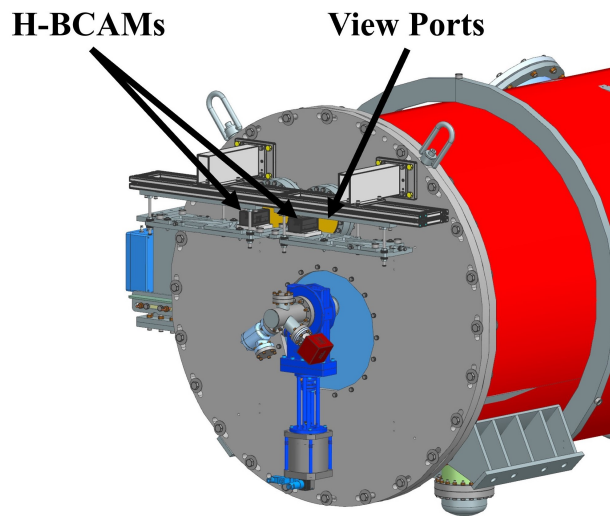


Figure 5.10: Downstream H-BCAMs installed on their permanent plates on pHB650 CM.

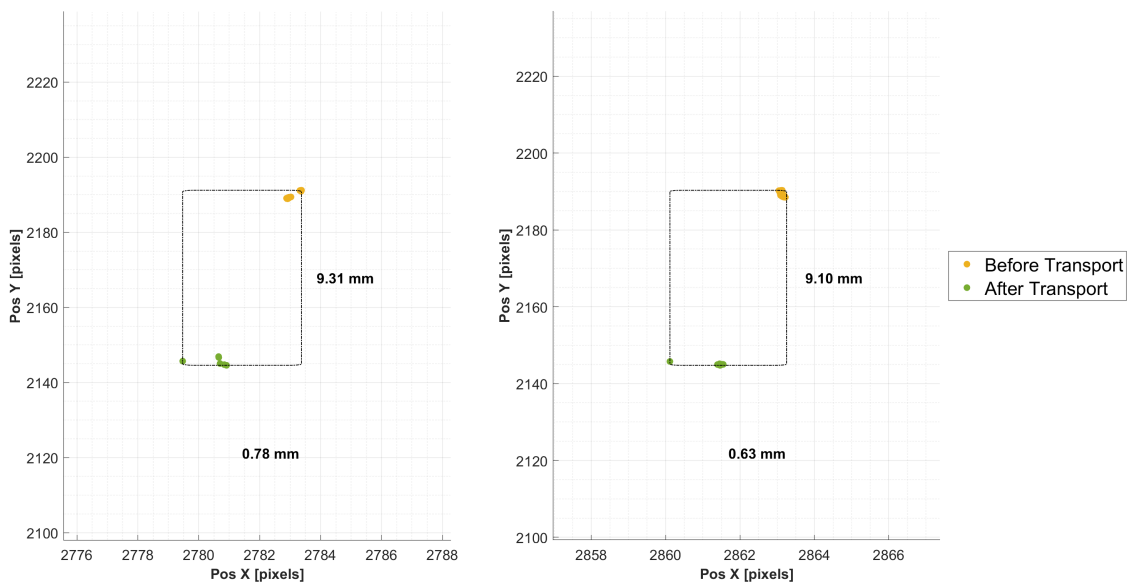


Figure 5.11: BCAM3 displacement after the transport.

## 5. Prototype High Beta 650 Cryomodule Data Acquisition

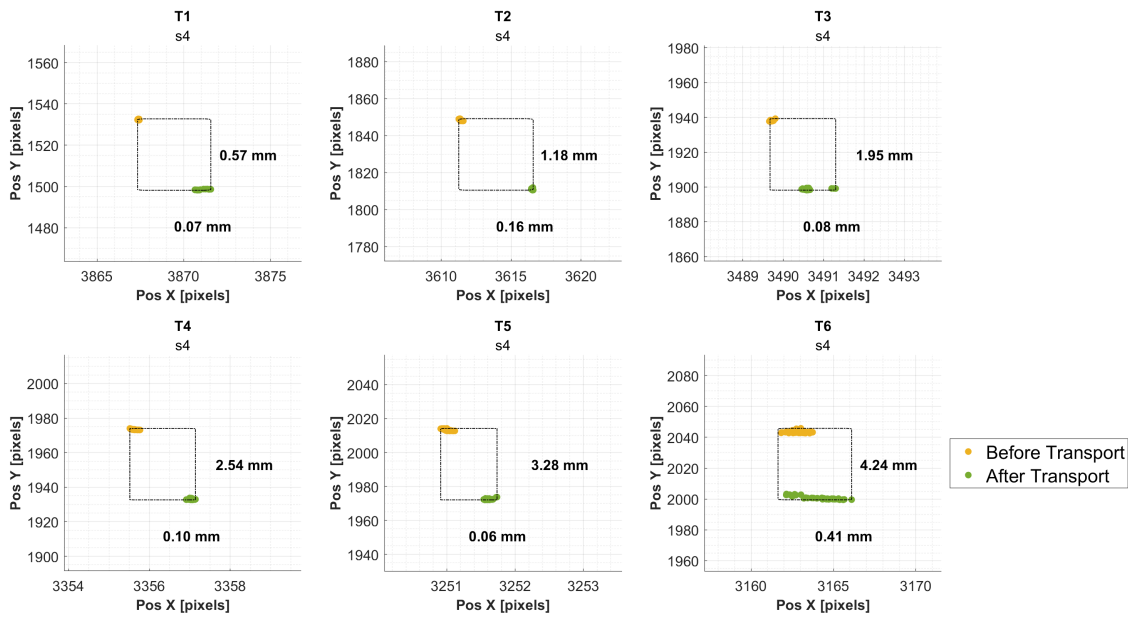


Figure 5.12: BCAM1 first six targets displacements after the transport.

The result which stands out is that, by increasing the distance between the target and the camera, the vertical displacement increases as well. The increment is linear, which leads to assume that the H-BCAMs have tilted about their transverse axis. This thesis is supported by the fact that, if the displacements measured are plotted as a function of the distance from the camera, a straight line can be found, with the least squared method, which approximates almost perfectly the experimental data (Figure 5.13). The  $R^2$  value is a number which tells how close the trend line is to the experimental data. The closer it is, the more  $R^2$  gets closer to 1. In this example showed,  $R^2 = 0.9994$ .

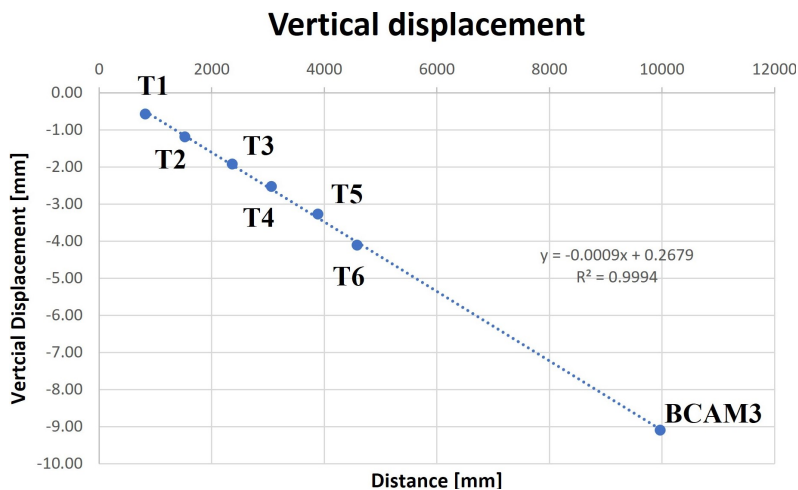


Figure 5.13: BCAM1 first six targets vertical displacement as a function of their distance from the camera.

Assuming that this hypothesis is real, the straight line evaluated can be used to find the corrections to apply to the experimental data. Indeed, the real measurement is the vertical distance between the recorded point and the tendency line, so the corrections, subtracted to the original data, are evaluated using the line equation and the position of the target. Table 5.1 reports the corrections for the first six targets of BCAM1. After applying the corrections, the results are consistent with the expectations of the transport operation. The average vertical displacement is  $-0.141$  mm, with a standard deviation of  $0.123$  mm.

**Table 5.1:** Corrections and new vertical displacements of the first six targets of BCAM1.

	Correction [mm]	New Displacement [mm]
T1	-0.472	-0.103
T2	-1.102	-0.088
T3	-1.857	-0.068
T4	-2.487	-0.038
T5	-3.230	-0.045
T6	-3.860	-0.245
BCAM3	-8.701	-0.399

Talking about the horizontal displacements, their magnitude is much smaller than the vertical one. Moreover, by plotting the displacements as a function of the target distance from the camera (Figure 5.14), it is clear that they are scattered, and it is not possible to find a tendency line interpolating the experimental data, so no correction was applied. In the case showed, the average value is  $-0.043$  mm, with a standard deviation of  $0.298$  mm.

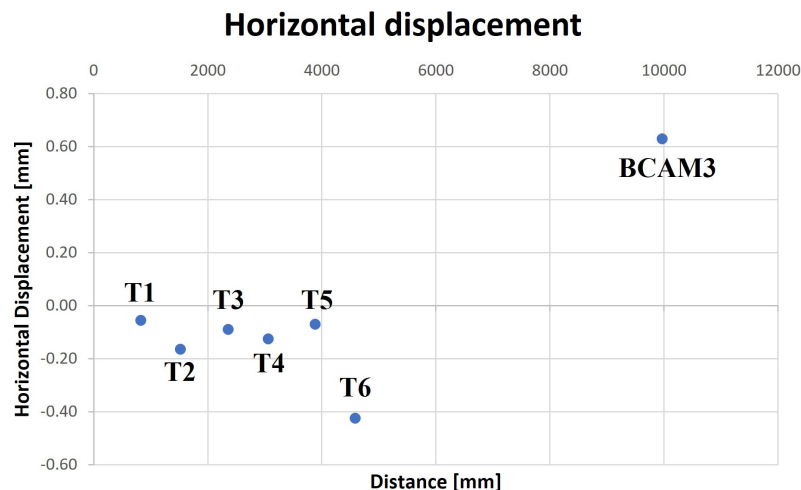


**Figure 5.14:** BCAM1 first six targets horizontal displacement as a function of their distance from the camera.

To better appreciate how the cavities have shifted after transport, Figure 5.15 and Figure 5.16 reports the cavities displacement, from upstream to downstream, seen by BCAM1 and BCAM3. The full results are reported in the appendix.

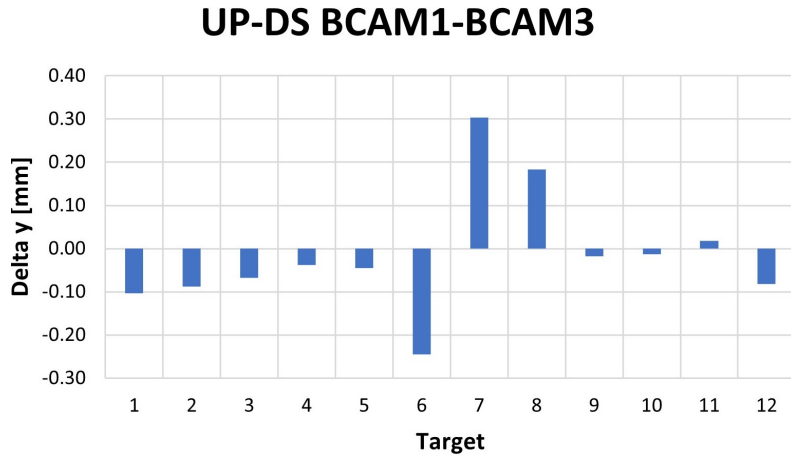


Figure 5.15: Corrected vertical displacements of the first twelve targets seen by BCAM1.

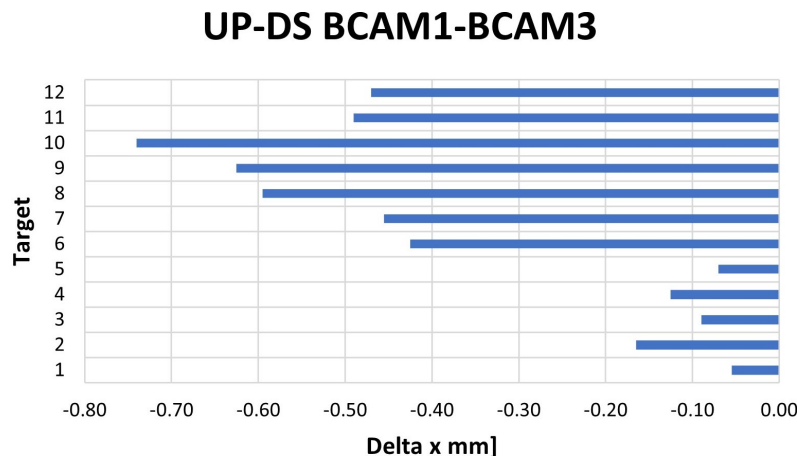


Figure 5.16: Horizontal displacements of the first twelve targets seen by BCAM1.

## 5.6 Pump-down Data Acquisition

Once the cryomodule is installed, its functionality is tested to make sure all the systems work as designed (vacuum, mechanical, instrumentation, cryogenic, RF system, safety). The first test performed is the pump-down test. It consists in creating vacuum inside the cryomodule, and back filling it with nitrogen. This test is performed several times, and the aim is to check the vacuum line and the CM capability to hold the vacuum inside. H-BCAMs were used during this test to check the alignment of the string assembly and to

compare the experimental values with the ones evaluated through numerical simulations. The vertical displacement recorded by BCAM1 watching BCAM3 is presented in Figure 5.17.

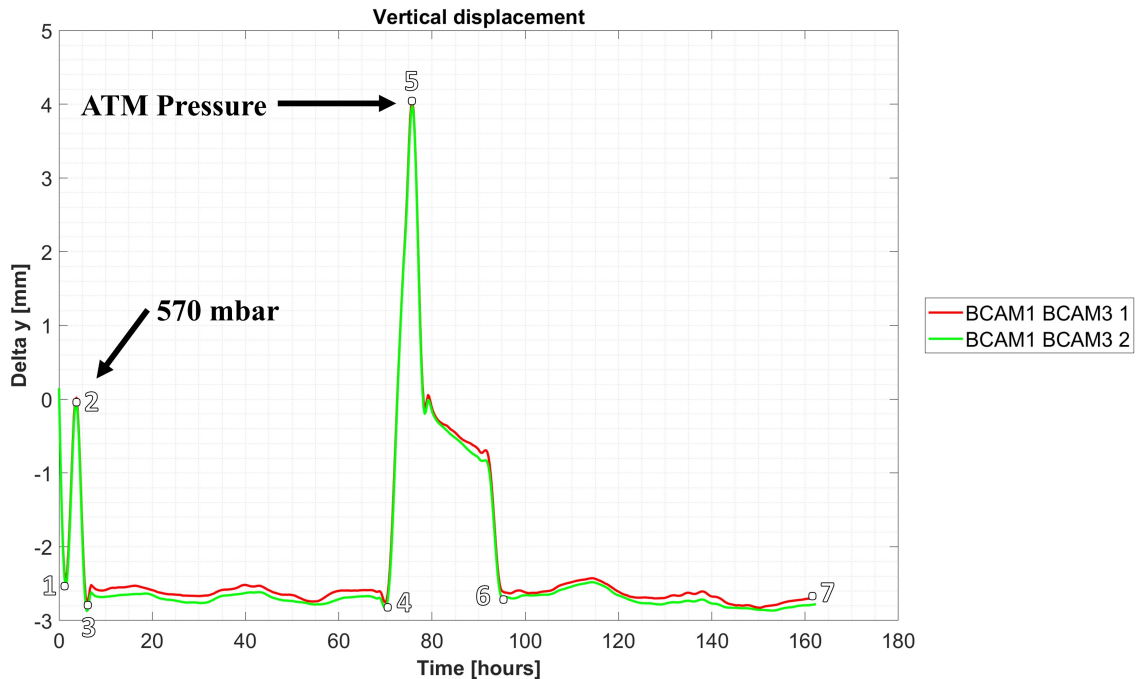


Figure 5.17: BCAM3 vertical displacement during the pump-down test.

In the plot, the vertical displacement has a different trend depending on the timestamp considered. Where there is a minimum, it means that the vacuum was created inside the cryomodule. This is true for point 1,3 and 6. Where the plot is flat, it means that the vacuum is held inside the CM (from point 3 to 4, from point 6 to 7). On the other hand, each peak corresponds to the point where nitrogen is back-filled inside the CM, leading to a pressure rise in the vessel. This is the case for point 2 and point 5. The average vertical displacement, during the test, is  $-2.197$  mm, with a standard deviation of  $1.123$  mm. The maximum value recorded  $4.341$  mm, while the minimum value is  $2.838$  mm. Two problems arise from the plot in Figure 5.17:

- Looking at the data, BCAM3 has a vertical displacement range of over 7 mm during the test. This is not reasonably realistic for this type of test where no thermal load is applied.
- When the CM is brought back to atmospheric pressure, the displacement recorded should be nil. By looking at points 5, this is not the case.

The acquisitions of BCAM1 are consistent with the other cameras acquisitions (they all present the same trend), meaning that there is no failure during the acquisition

occurred. The correlation between the vertical displacement and the pressure level inside the CM could be explained by looking at how the H-BCAMs are installed on the cryomodule. During the pump-down test, it is possible that the two end flanges bend under the vacuum load, leading to wrong data acquired. Indeed, a tilting angle of BCAM1 as low as  $0.017^\circ$ , results in a vertical displacement of BCAM3 of 3 mm. As for the second problem, one possible explanation could be that non-linearities in the assembly do not allow the system to come back its original position. Nevertheless, further investigation is needed to find out the nature of these problems.

The same trend can be found by analyzing the vertical displacements of the first twelve targets (Figure 5.18), from upstream to downstream. Therefore, the same conclusions can be drawn regarding the end flanges. In this case, the same phenomenon happening in the transport acquisition is visible: the greater is the distance between the target and the camera, the larger is the vertical displacement. While in the previous acquisition nothing was moving, which led to conclude that, during transport, the H-BCAMs setup shifted away from its original calibrated position, during the pump-down test the cryomodule is subjected to a vacuum load which changes in time (as seen in Figure 5.17), leading to conclude that the tilting angle is not fixed: this explains why, for example, the displacement of target 6 recorded by BCAM1 is either larger or smaller than the other targets in different moments. To graphically solve this problem, the same approach used for the static transport acquisition can be used, only this time it is applied for each timestamp. The corrected plot can be appreciated in Figure 5.19. The correction evaluates, for each time instant, the straight line which best fit the vertical displacements of the first twelve targets, and bring back these to their real value.

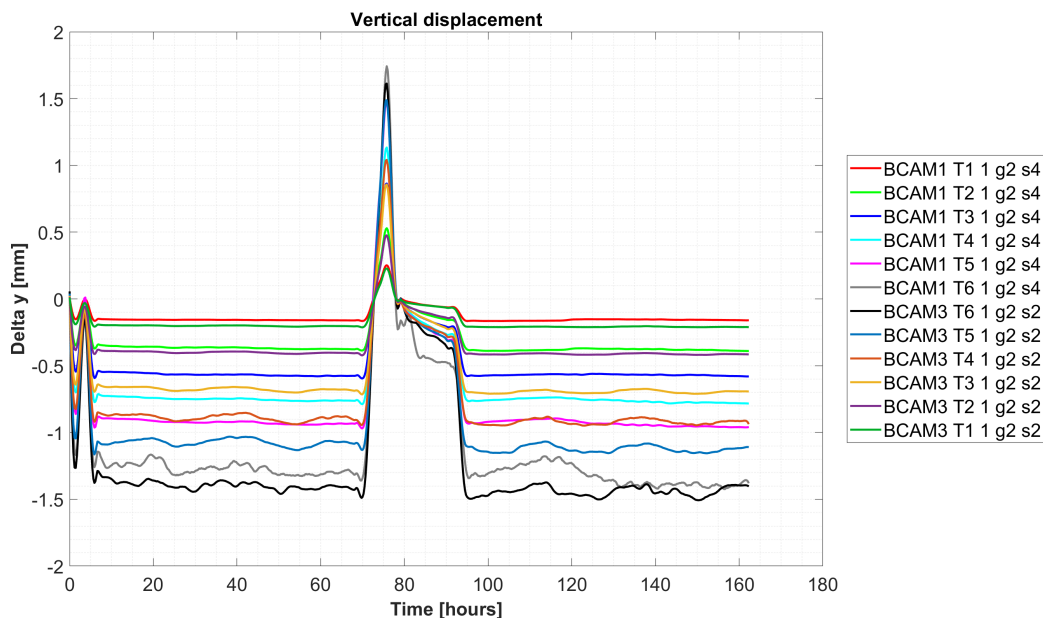
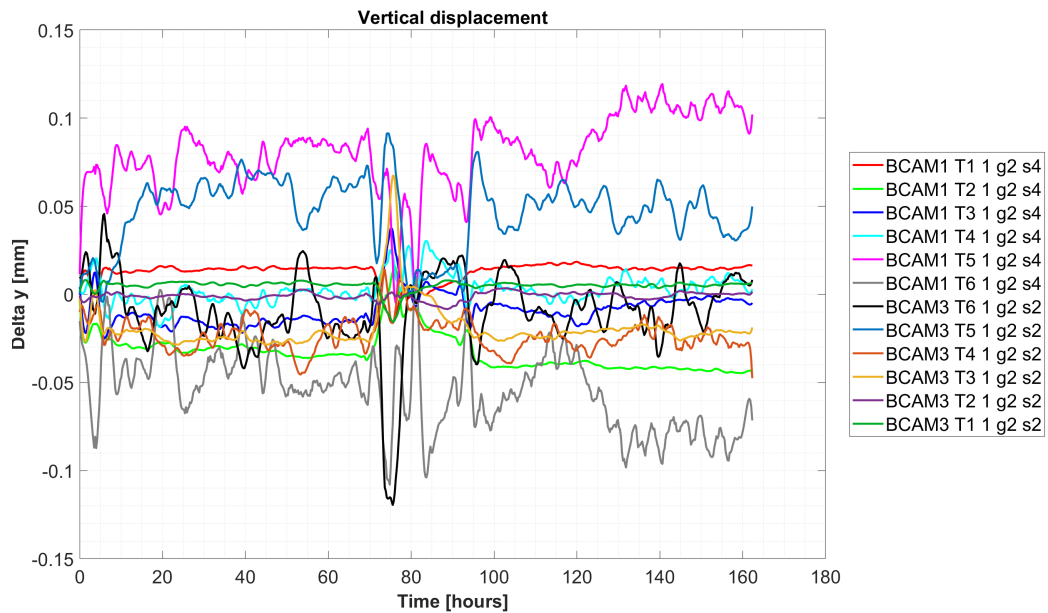


Figure 5.18: BCAM1 first twelve vertical displacement during the pump-down test.

## 5. Prototype High Beta 650 Cryomodule Data Acquisition



*Figure 5.19: BCAM1 first twelve corrected vertical displacement during the pump-down test.*

The final results are much smaller in magnitude and closer to the expected ones obtained with numerical simulations. The vertical displacements are spread around 0 mm, with a maximum value of 0.120 mm, and a minimum value of  $-0.120$  mm. As for the horizontal displacements, the acquisition of BCAM1 looking at BCAM3 is represented in Figure 5.20.

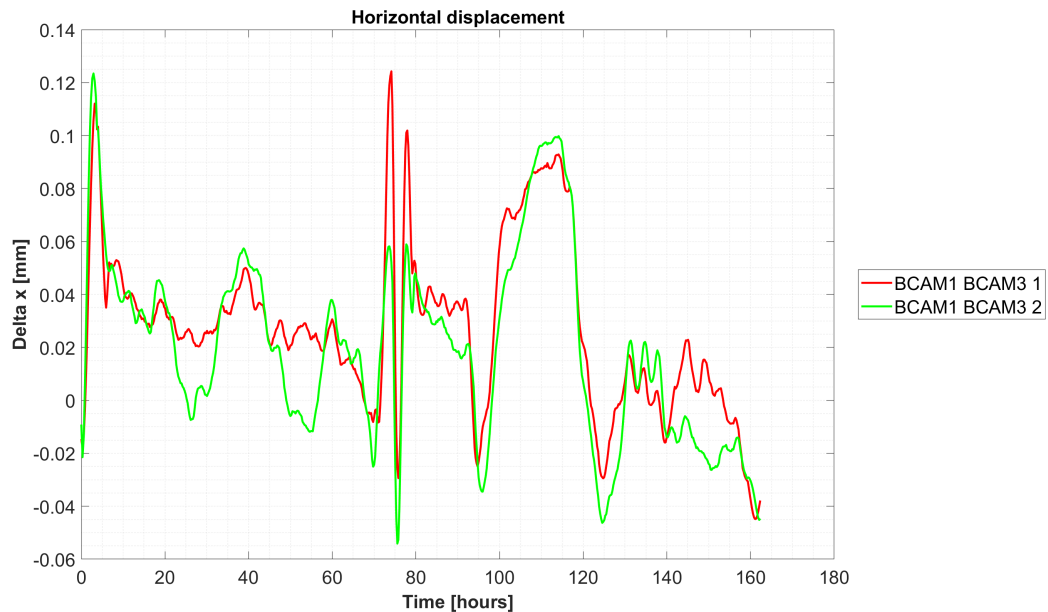


*Figure 5.20: BCAM3 horizontal displacement during the pump-down test.*

The results over time are distributed around 0.028 mm, which is the average value, with standard deviation of 0.034 mm. The maximum value is 0.179 mm, while the minimum value is  $-0.109$  mm. These results are consistent with the numerical analyses performed, seeking an horizontal displacement around 0 mm. As for the targets displacements, the data of the first twelve frames from BCAM1 to BCAM3 are reported in Figure 5.21. These results show that, during the pump-down test, also the horizontal displacements are influenced by the end flanges bending. This is clear from the analysis of the plot trend over time: it resembles the one on Figure 5.18, with minimums when vacuum is created inside, and peaks when nitrogen is back-filled in to the vessel. With respect to the vertical displacements, no clear angle can be found, so no correction can be applied to the horizontal ones. Nevertheless, they are spread around 0 mm, which was expected for this type of test.

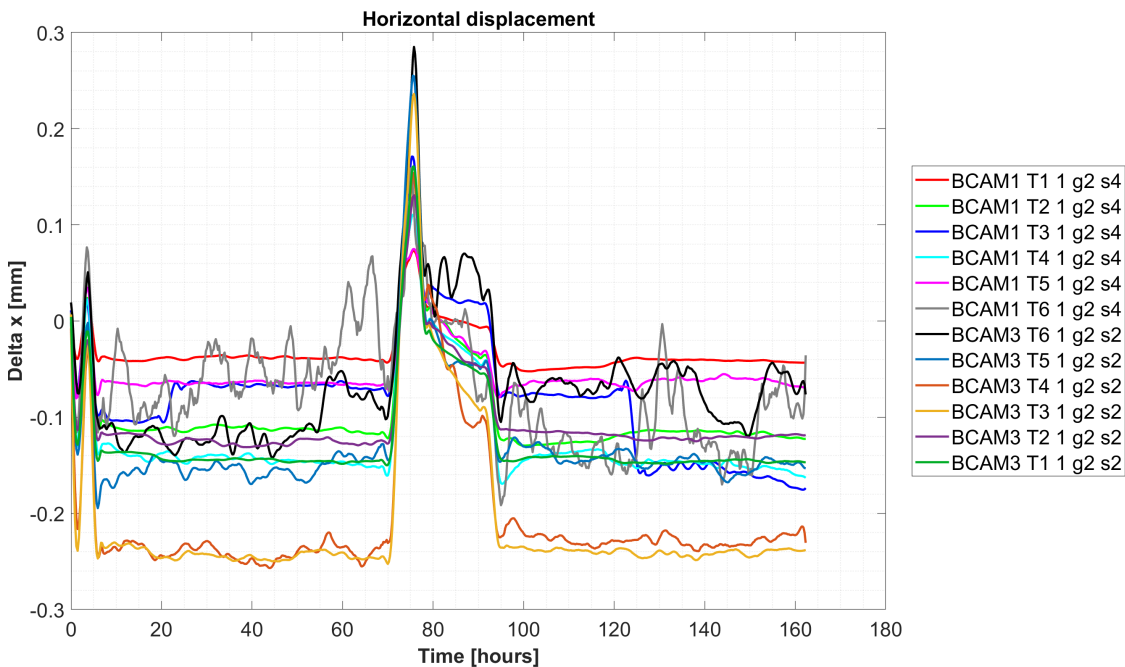
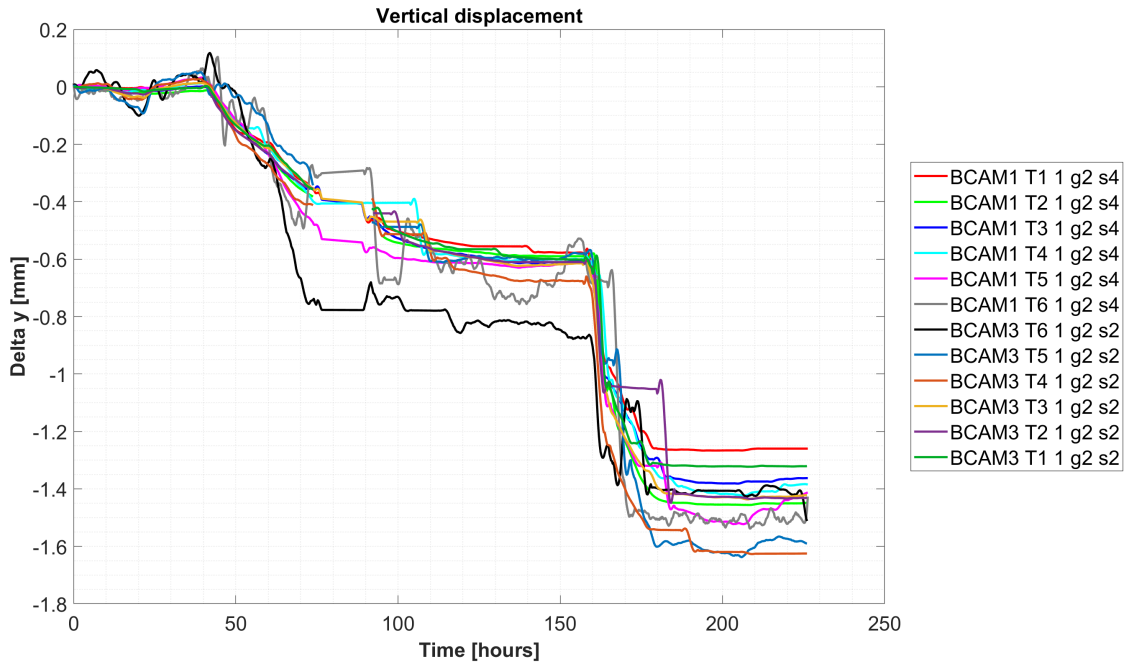


Figure 5.21: BCAM1 first twelve vertical displacement during the pump-down test.

## 5.7 Cooldown Data Acquisition

The next testing phase is the cooldown, where the CM is gradually cooled to nominal working temperatures to make the cavities superconductive. This process takes several days: the helium supply temperature is reduced gradually to limit thermal stresses arising. The H-BCAMs were set to trace the targets position to check the cavities alignment throughout the process. Results are then compared to numerical simulations to verify their reliability. In Figure 5.22, the vertical displacement of the first twelve targets, from upstream to downstream, is reported.



**Figure 5.22:** First twelve targets vertical displacement during the cooldown test.

The cooldown starts around hour 40, and it is clearly visible from the plot how it is a gradual process which is divided into several steps. Indeed, it is possible to state that there is correlation between the vertical displacement and the temperature inside the CM. With respect to the pump-down data acquisition, here vacuum was already created inside, so theoretically the CM end flanges should not be affected by this process. As a result, displacements are much smaller and more realistic, closer to the ones expected.

Firstly, the HTTS is cooled down. As it was for the SSR2 CM, it is placed on the aluminum rings shrink fitted on the support posts. When its temperature starts decreasing, the G10 composite supports start shrinking, which leads to a vertical lowering of the cavity (and targets). This contraction, by looking at the data, is equal to  $\Delta y = 0.600$  mm.

The second phase consists in cooling down the cavities to 2 K using liquid helium. This process starts around hour 160, and goes on until the design temperature is reached. At the end of it, the targets displacement is constant, meaning that steady-state conditions were reached inside the CM. The results are spread around  $-1.400$  mm, where targets BCAM3 T3 has the lower displacement ( $-1.650$  mm), and BCAM1 T1 has the highest one ( $-1.250$  mm). Their relative misalignment is  $\Delta y = 0.400$  mm, under the constraint limit reported in Table 1.1. The full results are available on Table C.1 in the appendix.

While targets displacements show realistic values, H-BCAMs ones showed in Figure 5.23 are conceptually wrong and further investigation is needed to understand why. Indeed, since vacuum was already created inside, the end flanges should not theoretically

move, but instead a displacements as large as  $-1.400$  mm is acquired. No explanation can be given for such a phenomenon, since the end flanges stay at room temperature for the whole process.

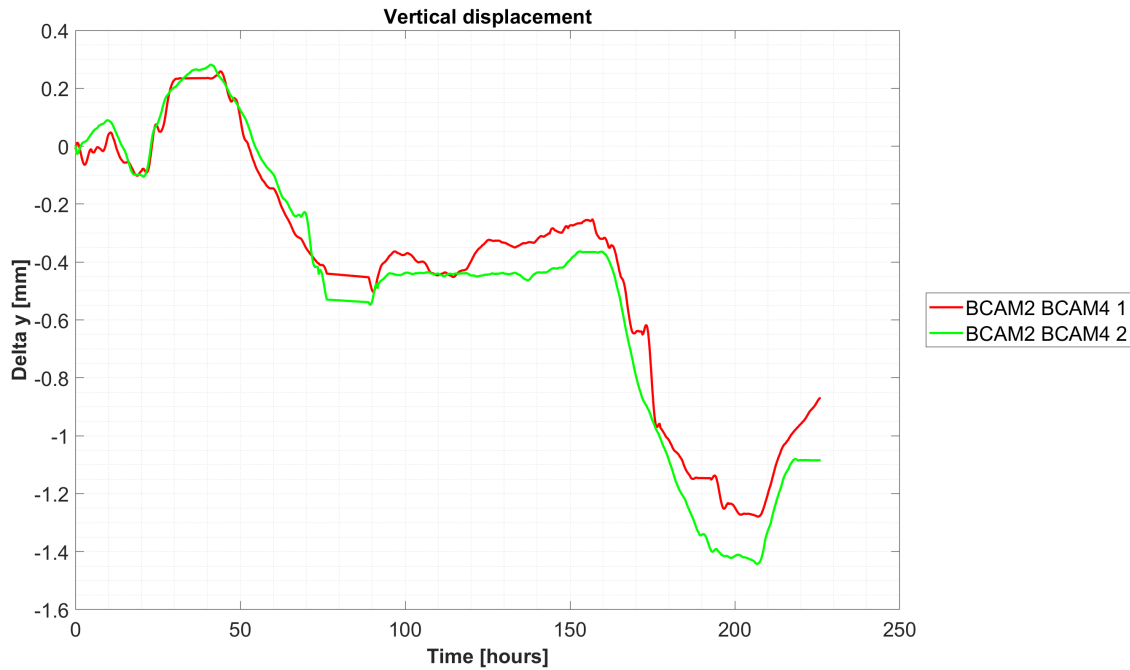


Figure 5.23: BCAM4 vertical displacement during the cooldown test.

As for horizontal displacements, in Figure 5.24 the ones of BCAM4 recorded by BCAM2 are reported. The main effect of the shrinking is the contraction along the vertical direction: as a results, horizontal displacements are much smaller in magnitude. Here, with respect to Figure 5.23, H-BCAMs displacements are spread around 0 mm, which was expected. Small displacements recorded during the test could be explained by saying that the four H-BCAMs are almost ten meters apart, and the cameras accuracy is reduced the further the targets are placed from the camera.

In Figure 5.25, the horizontal displacements of the first twelve targets, from upstream to downstream, are reported. The same comments can be drawn for the correlation between the displacements and the different stages of the cooldown. The final values are negative because the target brackets have a contraction which brings them closer to the cavity center, according to the reference system showed in Figure 5.1.

The results, at the end of the cooldown, are spread around  $-0.500$  mm, where target 3 of BCAM2 has the lowest displacement of  $-0.650$  mm, and target 5 of BCAM2 has the highest one equal to  $-0.350$  mm. A difference of  $\Delta x = 0.300$  mm exists between them. The full results are available in the appendix.

## 5. Prototype High Beta 650 Cryomodule Data Acquisition

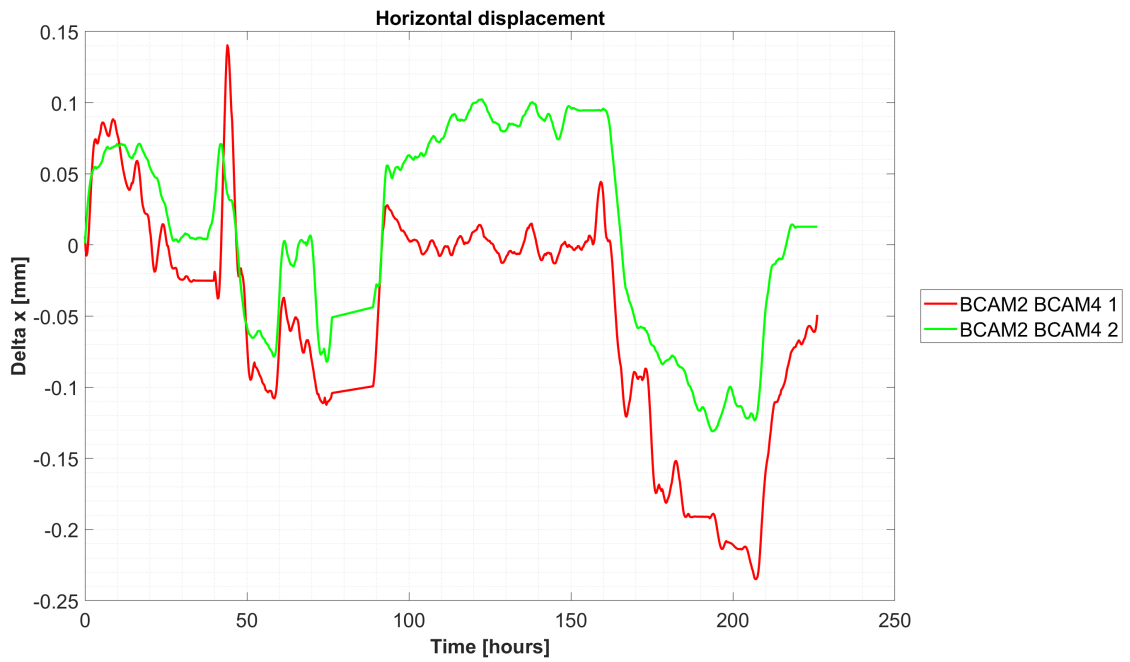


Figure 5.24: BCAM4 horizontal displacement during the cooldown test.

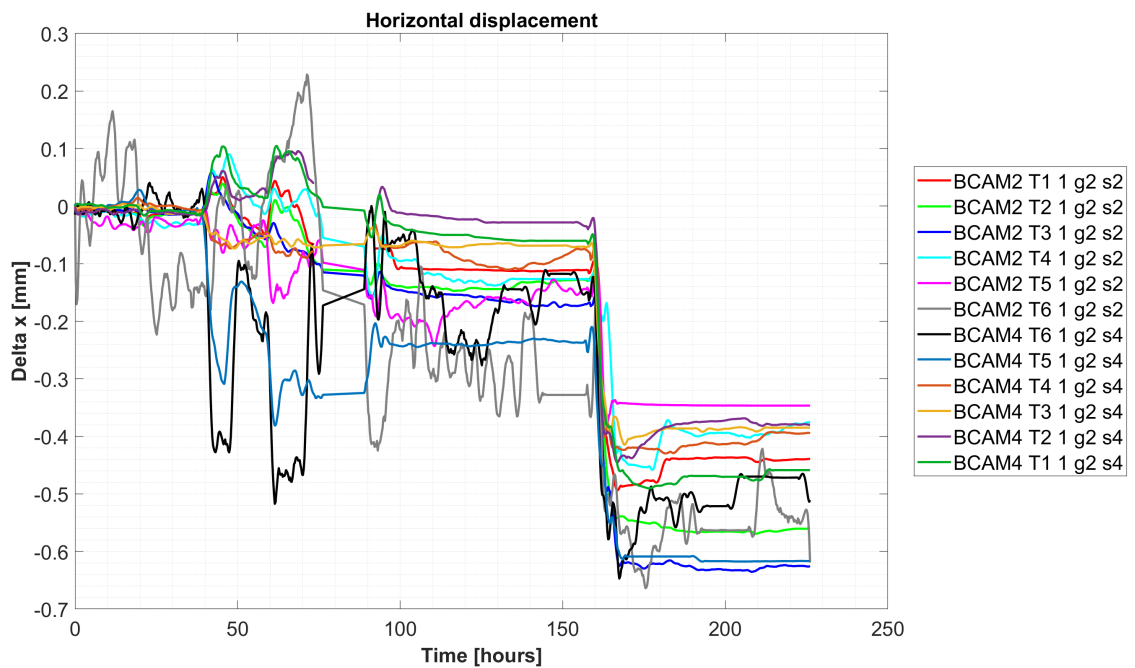


Figure 5.25: First twelve targets horizontal displacement during the cooldown test.

Starting from the vertical and horizontal results showed, it is possible to evaluate the cavities rotation angles, pitch and roll<sup>1</sup>, which must be under design limits. Since each cavity is provided with four targets, it is possible to find a unique plane passing through three of them. The fourth point is used to check whether the cavity is deforming abnormally. In Figure 5.26, it is represented a HB650 cavity, with the reference system, vectors and points used for the analysis.

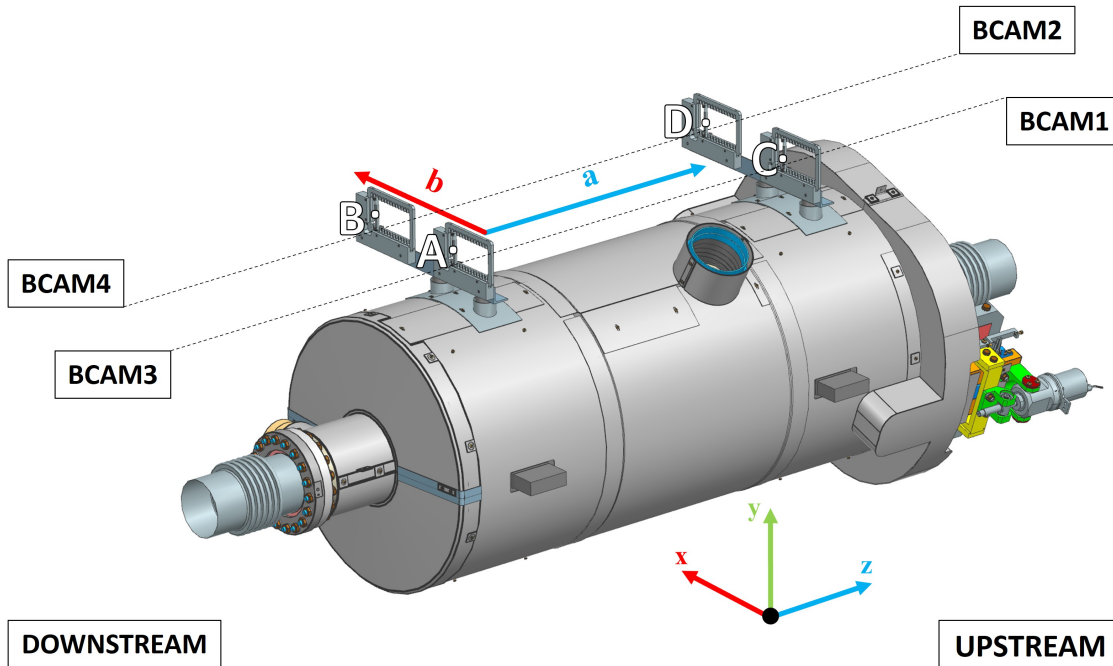


Figure 5.26: Close up of the HB650 cavities.

Three non-planar points define a plane in the space. Starting from point **A**, two vectors can be identified:  $\vec{AB}$ , named  $\vec{a}$ , and vector  $\vec{AC}$ , named  $\vec{b}$ . These two, together with the coordinates of point **A**, identify the unique equation of the plane passing through **A**, **B** and **C**. This procedure is repeated with two sets of coordinates, one at the beginning of the cooldown, and one at the end of it. The former were calculated from the laser tracker acquisition made before the string assembly insertion into the vacuum vessel, assuming point **A** as the origin of the plane, and point **B** and **C** to have its the same height. Finally, to find the rotation angles, equation 5.1 was used, where *start* and *end* refer to the two different timestamps at which  $\vec{a}$  and  $\vec{b}$  are evaluated.. The results are summarized in Table 5.2.

<sup>1</sup>The pitch angle is the rotation about the transversal axis *x*. The roll angle is the rotation about the longitudinal axis *z*.

$$\gamma = \cos^{-1}\left(\frac{a_{start} \cdot a_{end}}{|a_{start}| |a_{end}|}\right) \quad (5.1)$$

*Table 5.2: Main rotation angles of the HB650 cavities, from upstream to downstream.*

	<b>Cavity 1</b>	<b>Cavity 2</b>	<b>Cavity 3</b>	<b>Cavity 4</b>	<b>Cavity 5</b>	<b>Cavity 6</b>
<b>Pitch [°]</b>	-0.018	0.005	-0.016	0.031	0.009	0.012
<b>Roll [°]</b>	0.022	0.018	0.039	0.115	0.012	0.008
<b>D [mm]</b>	0.063	-0.111	-0.028	0.374	-0.042	-0.123

$D$ , in the table, refers to the distance between the point  $\mathbf{D}$ , whose coordinates were evaluated at the end of the cooldown, and the plane built by the vectors  $a_{end}^{\rightarrow}$  and  $b_{end}^{\rightarrow}$ . Considering the convection of the right hand, a positive rotation is anti-clockwise, while a negative one is clockwise.

According to Table 1.1, the rotation angles reported on Table 5.2 are all under design constraints, thus negligible. The maximum distance between the point  $\mathbf{D}$ , and the plane evaluated at the end of the cooldown, belongs to cavity 4, which has also the highest roll angle among all the cavities. As a matter of facts, the results are reasonably close to zero, meaning that the cavities are behaving as expected during the cooldown.

---

## Chapter 6

# Conclusion

The numerical analyses performed were successfully completed. The results obtained are consistent with the expectations, meaning that the models built were set up correctly. Thermal and structural analyses proved to be reliable and realistic, giving an outlook on how the components behave under nominal and off-design conditions.

Regarding the data acquisition, the H-BCAMs proved to be a reliable instrument to monitor the alignment of the coldmass components throughout all the assembling, transportation and testing phases. To exploit their full potential, the cameras need proper installation and calibration; as a result, the hardware used to mount the H-BCAMs needs to be improved, as well as the procedure used to make sure their view field is empty of obstacles.

Firstly, the movable aluminum stand used to support the cameras for the reference acquisition, and for the insertion acquisition, needs to be anchored to the string assembly and to the cryomodule. In this way, its position, relatively to the targets, stays within acceptable misalignment limits. The resulting acquisition are going to be more reliable and more accurate by removing the human error coming from the alignment of the stand based on the laser tracker acquisition.

Moreover, the fixed plates at the two ends of the cryomodule, where H-BCAMs are permanently installed on, must be checked before and after transport to make sure that nothing compromised the cameras alignment. This is crucial to not influence the acquisition of the targets' position by creating dummy displacements due to the H-BCAMs tilting. Cleaning functions could delete this problem, but their reliability and precision need to be proven by correlating their results to an actual experimental acquisition.

Furthermore, to check the end flanges displacements during the pump-down test, a network of H-BCAMs can be introduced. It consists in involving external cameras that, instead of tracing the targets' position, they measure the main four H-BCAMs alignment

## 6. Conclusion

---

during the test. Results of the pump-down acquisition showed that, even a small angle, caused by the bending of the two end flanges, can have a huge impact on the measured displacements by the cameras. If other H-BCAMs were used to effectively detect how the end flanges are moving under the vacuum load inside the CM, these displacements can be compensated by a script to obtain more accurate results. An easier and cheaper alternative solution can involve the use of a movable stand to place next to the end flanges, in this way the H-BCAMs are not directly installed on them. The stand should have the same characteristics of the ones used for the insertion.

Finally, the MLI which wraps around the coldmass assembly has shiny, highly reflective surfaces, which interfere with the targets detection. This problem was particularly difficult to eliminate, since it cannot be taken into account by a script, but simultaneously it is crucial component to reduce the radiative heat transfer coming from room temperature components. A higher attention must be paid to clear the H-BCAMs view field from the MLI, exploring the possibility to change the surfaces color to reduce their reflection coefficient.

---

# Appendix A

# Material Data



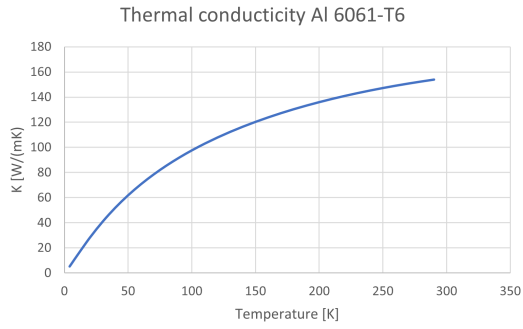
Torque Values for Stainless Steel and Non-Ferrous Fasteners

Bolt Size	18-8 Stainless Steel		316 Stainless Steel		Silicon Bronze	Monel	Brass	2024-T4 Aluminum
	Dry	Lubricated	Dry	Lubricated				
2-56	2.5 in-lbs	2.1 in-lbs	2.6 in-lbs	2.2 in-lbs	2.3 in-lbs	2.5 in-lbs	2.0 in-lbs	1.4 in-lbs
2-64	3	2.6	3.2	2.7	2.8	3.1	2.5	1.7
4-40	5.2	4.4	5.5	4.7	4.8	5.3	4.3	2.9
4-48	6.6	5.6	6.9	5.9	6.1	6.7	5.4	3.6
5-40	7.7	6.5	8.1	6.9	7.1	7.8	6.3	4.2
5-44	9.4	8.0	9.8	8.3	8.7	9.6	7.7	5.1
6-32	9.6	8.2	10.1	8.6	8.9	9.8	7.9	5.3
6-40	12.1	10.3	12.7	10.8	11.2	12.3	9.9	6.6
8-32	19.8	16.8	20.7	17.6	18.4	20.2	16.2	10.8
8-36	22	18.7	23	19.6	20.4	22.4	18.0	12.0
10-24	22.8	19.4	23.8	20.2	21.2	25.9	18.6	13.8
10-32	31.7	26.9	33.1	28.1	29.3	34.9	25.9	19.2
1/4-20	75.2	63.9	78.8	67	68.8	85.3	61.5	45.6
1/4-28	94	80	99	84	87	106	77	57
5/16-18	132	112	138	117	123	149	107	80
5/16-24	142	121	147	125	131	160	116	86
3/8-16	236	201	247	210	219	266	192	143
3/8-24	259	220	271	230	240	294	212	157
7/16-14	376	320	393	334	349	427	317	228
7/16-20	400	340	418	355	371	451	327	242
1/2-13	43 ft-lbs	37 ft-lbs	45 ft-lbs	38 ft-lbs	40 ft-lbs	48.7 ft-lbs	35.2 ft-lbs	26 ft-lbs
1/2-20	45	38	47	40	42	51	37	27
9/16-12	56	48	59	50	53	65	47	34
9/16-18	62	53	65	55	58	71	51	38
5/8-11	92	78	96	82	86	111	76	60
5/8-18	103	88	108	92	96	123	85	67
3/4-10	127	108	131	111	118	153	104	82
3/4-16	124	105	129	110	115	149	102	80
7/8-9	194	165	202	172	178	231	159	124
7/8-14	193	164	201	171	177	230	158	124
1 - 8	286	243	299	254	265	344	235	184
1 - 14	259	220	270	230	240	311	212	166
1-1/8 - 7	413	351	432	367	383	499	337	265
1-1/8 - 12	390	332	408	347	361	470	318	251
1-1/4 - 7	523	445	546	464	485	627	428	336
1 1/4 - 12	480	408	504	428	447	575	394	308
1-1/2 - 6	888	755	930	791	822	1064	727	570
1-1/2 - 12	703	598	732	622	651	840	575	450

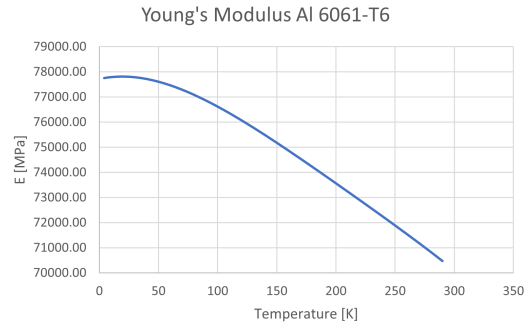
Suggested Maximum Torquing Values - a guide based upon actual lab testing on dry or near dry fasteners wiped clean. While Fastenal has used reliable sources and testing to determine these values, there are many variables that will effect the results and the use of this information is at sole risk of the user.  
 Values through 7/16" diameter are stated in inch-pounds; 1/2" diameter and over are stated in foot-pounds.

Figure A.1: Tightening torque values from F.E.D.S.

## A. Material Data



**Figure A.2:** Thermal conductivity Al 6061-T6.



**Figure A.3:** Young's Modulus Al 6061-T6.

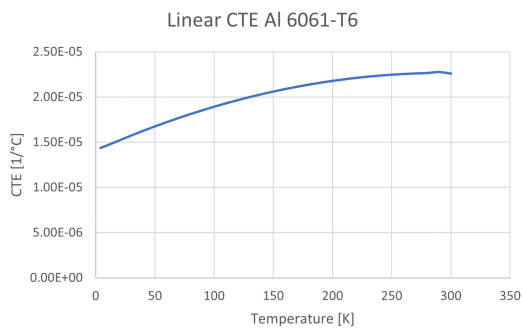


**Figure A.4:** CTE Al 6061-T6.

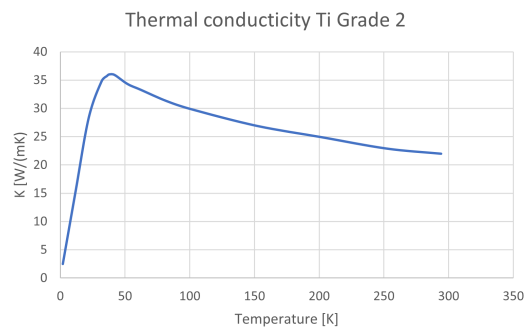


**Figure A.5:** Thermal conductivity Ti Grade 2.

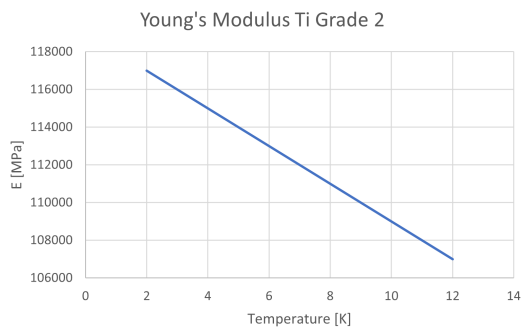


**Figure A.6:** Young's Modulus Ti Grade 2.

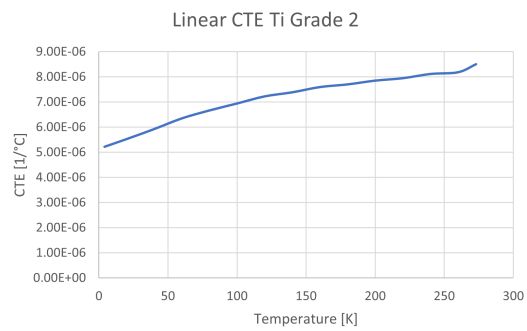


**Figure A.7:** CTE Ti Grade 2.

## A. Material Data

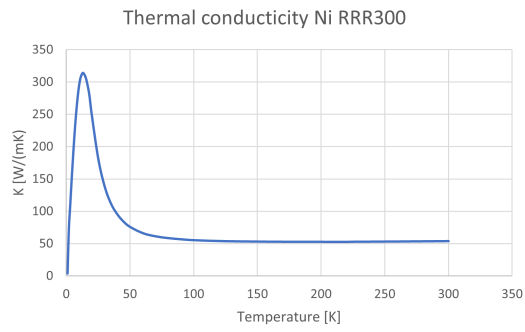


**Figure A.8:** Thermal conductivity Ni RRR300.

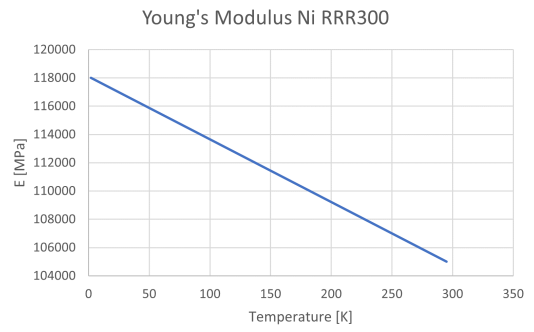


**Figure A.9:** Young's Modulus Ni RRR300.

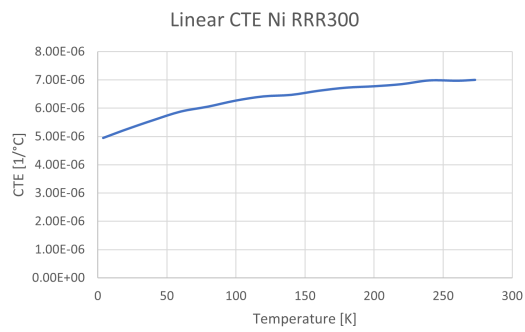


**Figure A.10:** CTE Ni RRR300.

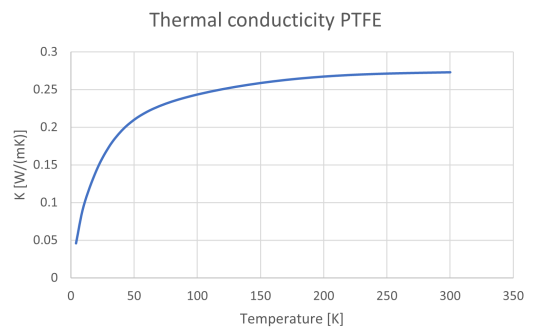


**Figure A.11:** Thermal conductivity PTFE.

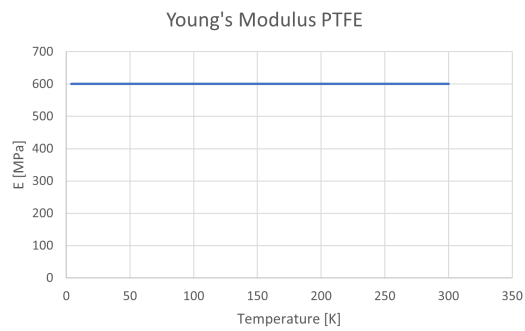


**Figure A.12:** Young's Modulus PTFE.

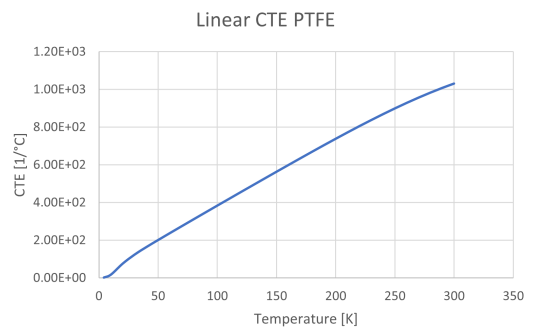


**Figure A.13:** CTE PTFE.

## A. Material Data

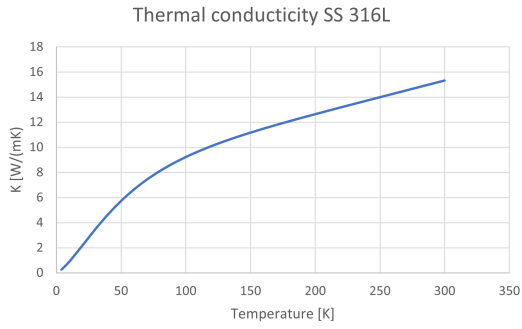


**Figure A.14:** Thermal Conductivity SS 316L.



**Figure A.15:** Young's Modulus SS 316L.

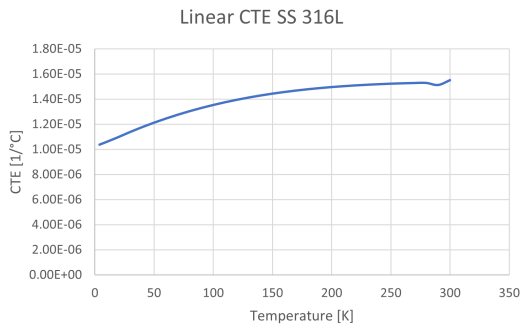


**Figure A.16:** CTE SS 316L.

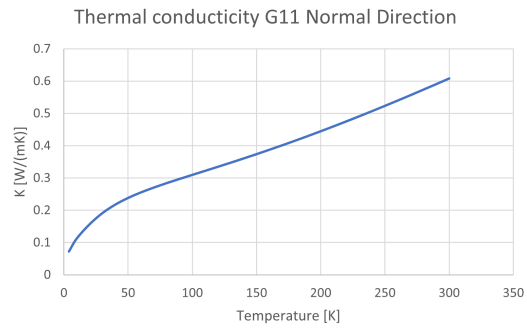


**Figure A.17:** Thermal Conductivity G11.

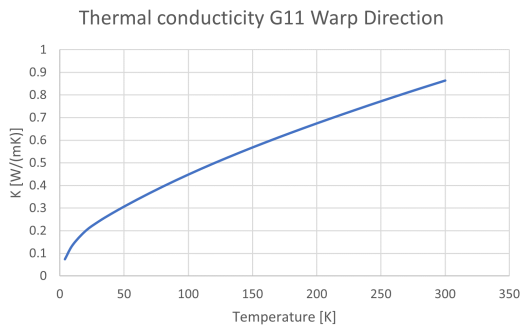


**Figure A.18:** CTE SS 316L

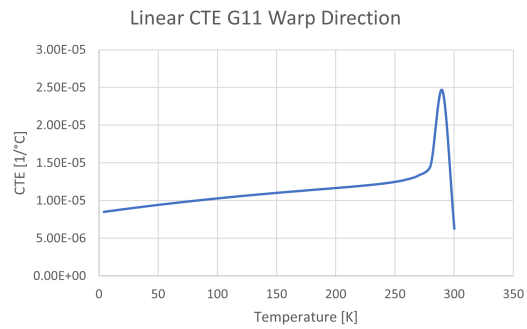


**Figure A.19:** CTE G11.

# Appendix B

## Numerical Results

### B.1 H-BCAMs Stand - STC

**D: Static Structural**  
x displacement  
Type: Directional Deformation(X Axis)  
Unit: mm  
Global Coordinate System  
Time: 2 s  
2/20/2023 8:24 AM

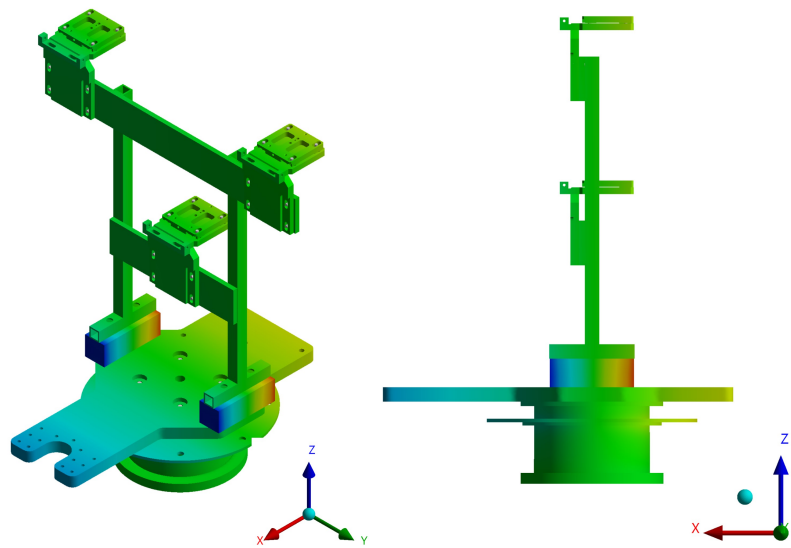
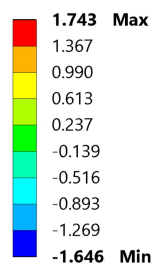


*Figure B.1: Results of the Static Structural Analysis: H-BCAMs stand displacements along x.*

## B. Numerical Results

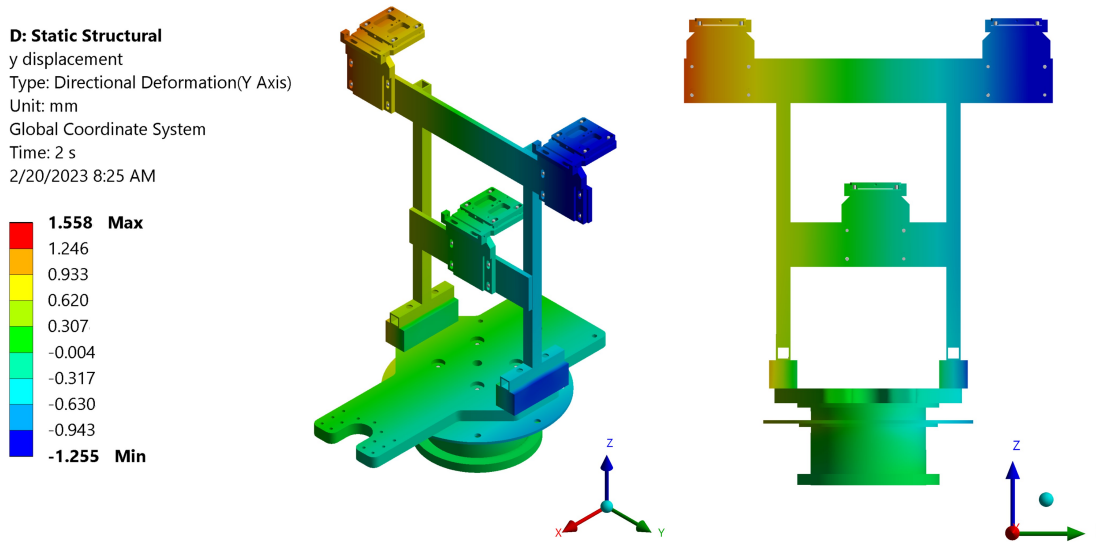


**Figure B.2:** Results of the Static Structural Analysis: H-BCAMs stand displacements along y.

**Table B.1:** Numerical results of the sensitivity analysis.

<b>T [K]</b>	<b>P [W]</b>	<b>z<sub>0</sub> [mm]</b>	<b>z<sub>1</sub> [mm]</b>	<b>z<sub>2</sub> [mm]</b>	<b>T<sub>1</sub> [K]</b>	<b>T<sub>2</sub> [K]</b>
60	15.000	-0.570	-1.273	-1.155	273.700	280.700
	20.000	-0.566	-0.692	-0.753	301.600	311.700
	25.000	-0.563	-0.170	-0.384	324.300	338.000
80	15.000	-0.549	-1.229	-1.113	275.000	282.000
	20.000	-0.546	-0.645	-0.712	302.000	311.000
	25.000	-0.543	-0.128	-0.347	325.000	339.000
100	15.000	-0.527	-1.162	-1.058	277.000	284.200
	20.000	-0.523	-0.582	-0.660	304.150	314.420
	25.000	-0.520	-0.072	-0.289	326.250	340.000

## B.2 SSR2 Cavity - STC

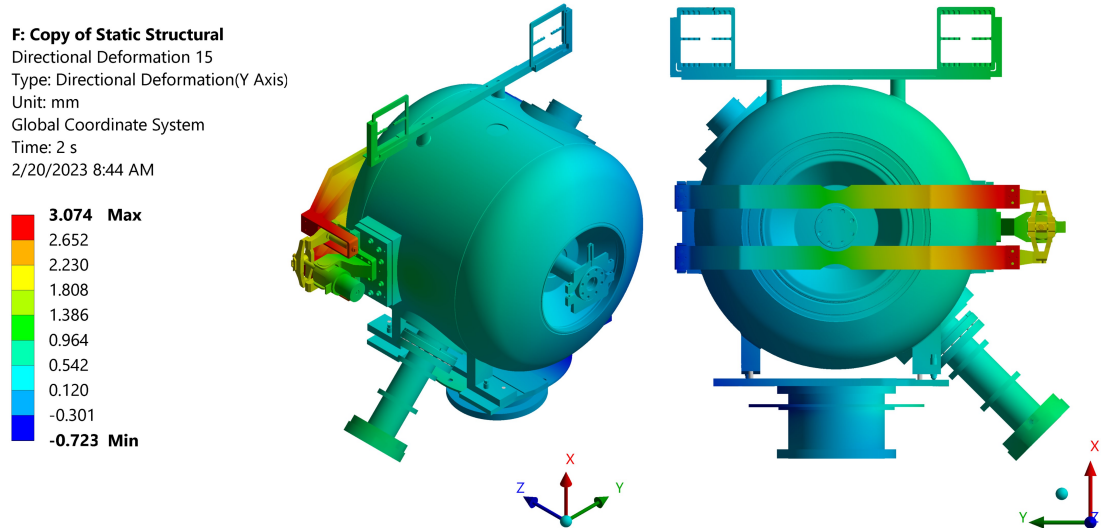


Figure B.3: Results of the Static Structural Analysis: SSR2 cavity displacements along y.

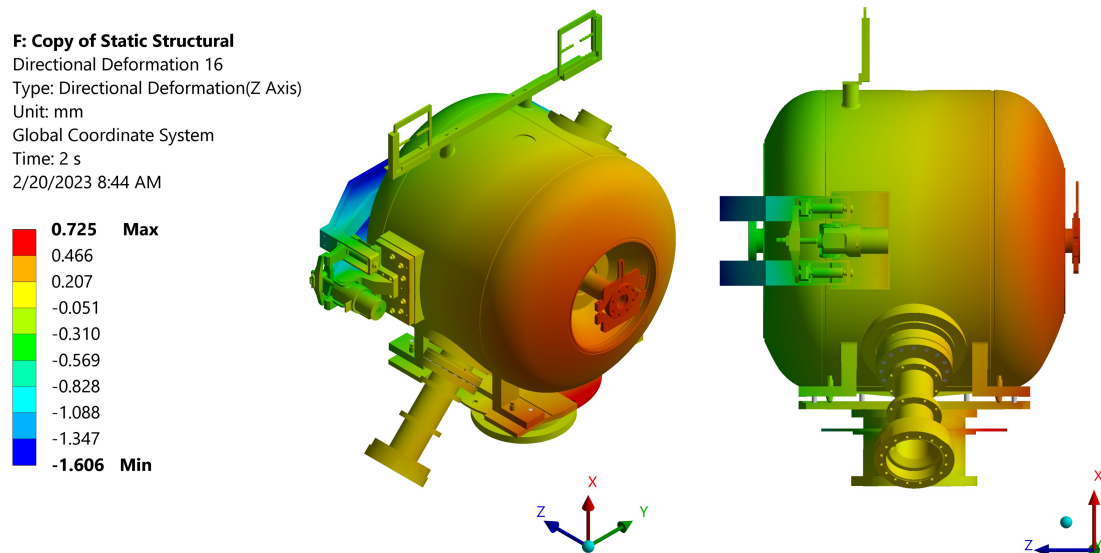


Figure B.4: Results of the Static Structural Analysis: SSR2 cavity displacements along z.

### B.3 SSR2 CM

**M: Copy of Copy of Static Structural**  
Directional Deformation 11  
Type: Directional Deformation(X Axis)  
Unit: mm  
Global Coordinate System  
Time: 2 s  
2/20/2023 9:48 AM

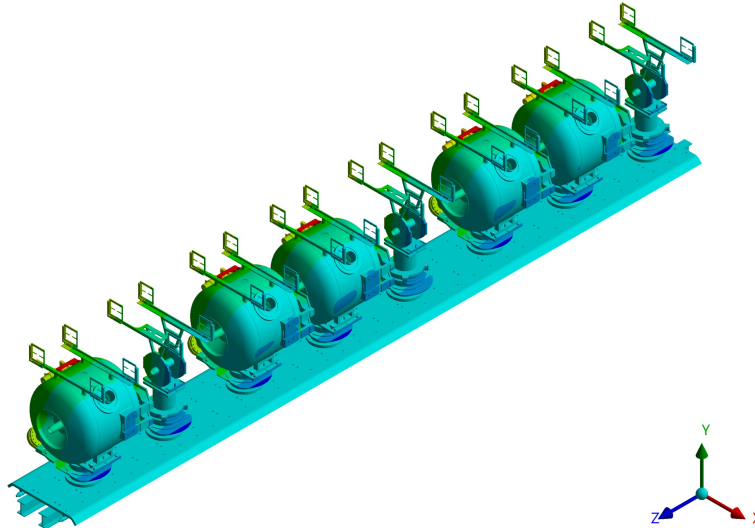
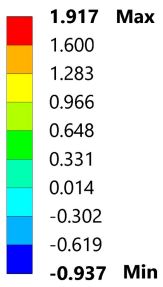


Figure B.5: Results of the Static Structural Analysis: SSR2 displacements along x, isometric view.

**M: Copy of Copy of Static Structural**  
Directional Deformation 11  
Type: Directional Deformation(X Axis)  
Unit: mm  
Global Coordinate System  
Time: 2 s  
2/20/2023 9:48 AM

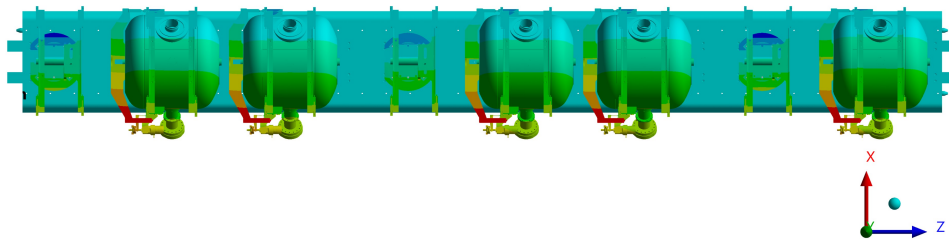
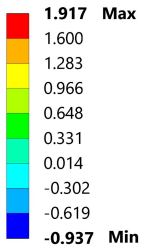


Figure B.6: Results of the Static Structural Analysis: SSR2 displacements along x, top view.

## B. Numerical Results

### M: Copy of Copy of Static Structural

Directional Deformation 13

Type: Directional Deformation(Z Axis)

Unit: mm

Global Coordinate System

Time: 2 s

2/20/2023 9:49 AM

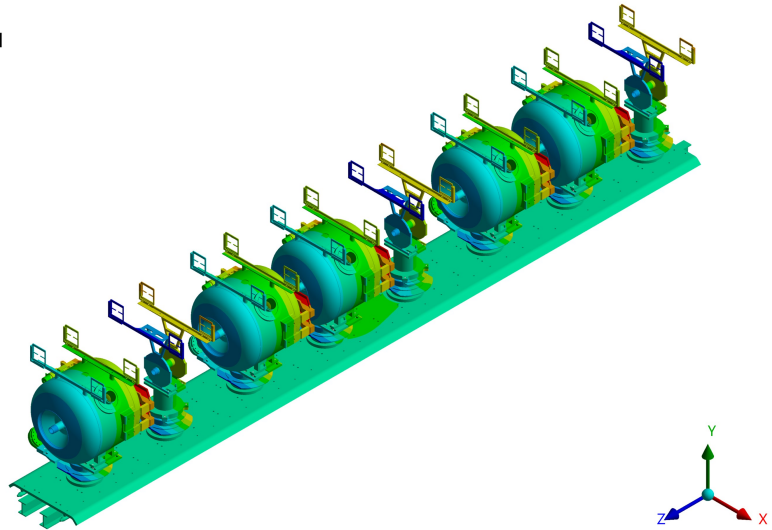
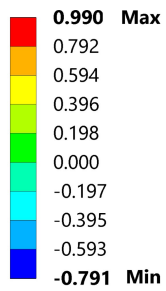


**Figure B.7:** Results of the Static Structural Analysis: SSR2 displacements along z, isometric view.

### M: Copy of Copy of Static Structural

Directional Deformation 13

Type: Directional Deformation(Z Axis)

Unit: mm

Global Coordinate System

Time: 2 s

2/20/2023 9:53 AM

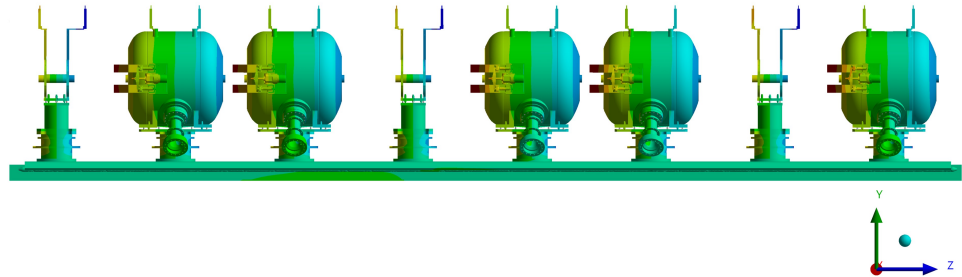
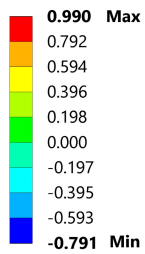


**Figure B.8:** Results of the Static Structural Analysis: SSR2 displacements along z, side view.

## B. Numerical Results

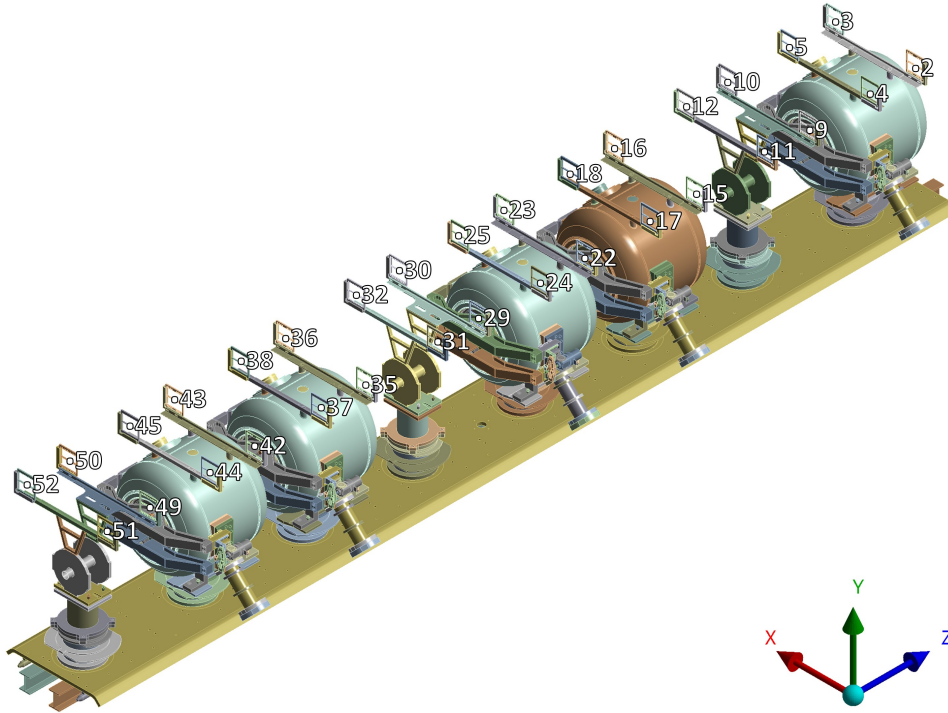


**Figure B.9:** Reference points to evaluate the SSR2 cavity Static Structural analysis results, isometric view.

**Table B.2:** Displacements of the couplers external flange, case study 1.

Point	x [mm]	y [mm]	z [mm]
7	0.691	-1.146	0.002
20	0.671	-1.165	-0.002
27	0.677	-1.160	-0.005
40	0.716	-1.117	0.017
47	0.690	-1.154	0.018

## B. Numerical Results

---

**Table B.3:** Target displacements of the string assembly, case study 1.

<b>Point</b>	<b>x [mm]</b>	<b>y [mm]</b>	<b>z [mm]</b>
2	0.132	-2.285	-0.262
3	-0.683	-2.082	-0.228
4	0.135	-2.294	0.237
5	-0.678	-2.083	0.230
9	0.351	-2.809	-0.691
10	-0.463	-2.746	-0.701
11	0.347	-2.844	0.595
12	-0.468	-2.784	0.582
15	0.132	-2.285	-0.247
16	-0.686	-2.078	-0.225
17	0.126	-2.291	0.250
18	-0.689	-2.073	0.229
22	0.129	-2.279	-0.264
23	-0.689	-2.070	-0.241
24	0.124	-2.290	0.237
25	-0.691	-2.070	0.216
29	0.369	-2.780	-0.727
30	-0.445	-2.720	-0.751
31	0.350	-2.842	0.561
32	-0.464	-2.775	0.534
35	0.115	-2.286	-0.245
36	-0.697	-2.077	-0.237
37	0.111	-2.290	0.253
38	-0.697	-2.076	0.247
42	0.125	-2.289	-0.246
43	-0.691	-2.078	-0.223
44	0.122	-2.295	-0.248
45	-0.690	-2.078	0.230
49	0.327	-2.804	-0.726
50	-0.488	-2.734	-0.706
51	0.336	-2.848	0.562
52	-0.478	-2.777	0.580

## B. Numerical Results

---

**Table B.4:** Beamline displacements of the coldmass assembly, case study 2.

Point	Displacement y [mm]	Point	Displacement y [mm]
1	-1.801	6	-1.823
8	-1.905	13	-1.902
14	-1.808	19	-1.803
21	-1.800	26	-1.805
28	-1.884	33	-1.900
34	-1.796	39	-1.801
41	-1.804	46	-1.802
48	-1.899	53	-1.903

**Table B.5:** Displacements of the couplers external flange, case study 2.

Point	x [mm]	y [mm]	z [mm]
7	0.689	-1.060	0.018
20	0.658	-1.080	-0.004
27	0.677	-1.081	-0.003
40	0.706	-1.032	0.018
47	0.683	-1.064	0.012

## B. Numerical Results

---

**Table B.6:** Target displacements of the string assembly, case study 2.

	<b>x [mm]</b>	<b>y [mm]</b>	<b>z [mm]</b>
2	0.704	-2.322	-0.272
3	-0.112	-2.490	-0.243
4	0.703	-2.340	0.226
5	-0.109	-2.500	0.216
9	0.668	-2.727	-0.696
10	-0.146	-2.993	-0.696
11	0.666	-2.760	0.608
12	-0.148	-3.028	0.590
15	0.681	-2.325	-0.246
16	-0.136	-2.483	-0.221
17	0.667	-2.33	0.251
18	-0.137	-2.478	0.234
22	0.667	-2.323	-0.264
23	-0.151	-2.470	-0.240
24	0.663	-2.334	0.236
25	-0.151	-2.470	0.219
29	0.691	-2.697	-0.734
30	-0.230	-2.968	-0.749
31	0.673	-2.760	0.570
32	-0.141	-3.022	0.538
35	0.664	-2.323	-0.244
36	-0.148	-2.477	-0.245
37	0.660	-2.331	0.243
38	-0.147	-2.481	0.240
42	0.680	-2.326	-0.248
43	-0.135	-2.482	-0.214
44	0.684	-2.330	-0.246
45	-0.128	-2.480	0.240
49	0.652	-2.719	-0.732
50	-0.163	-2.985	-0.703
51	0.663	-2.573	0.573
52	-0.152	-3.027	0.585

# Appendix C

## pHB650 Data Acquisition

### C.1 Insertion

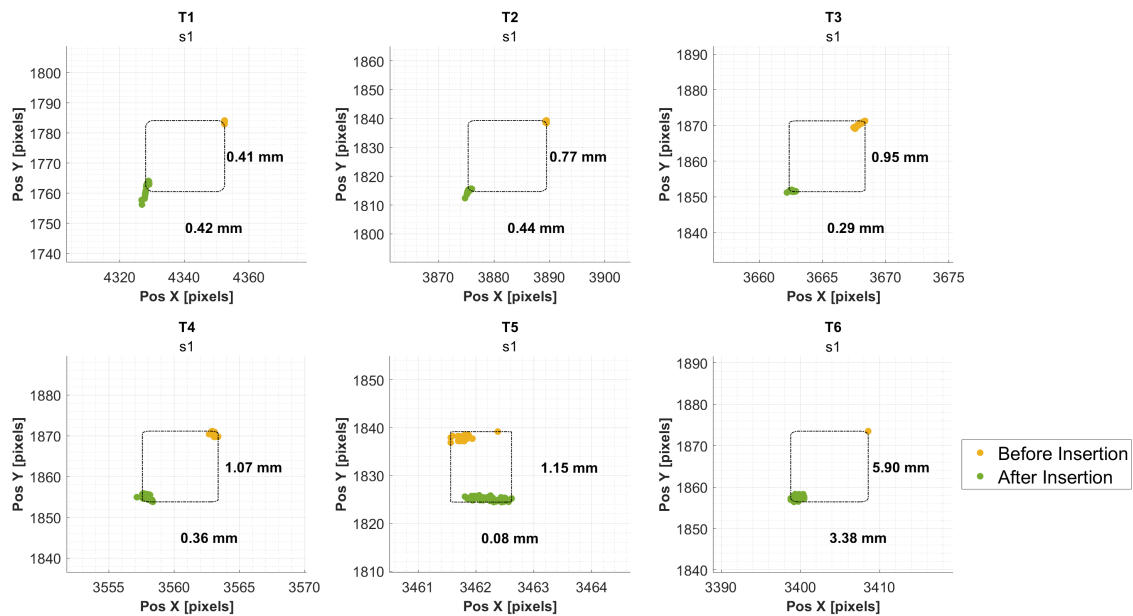
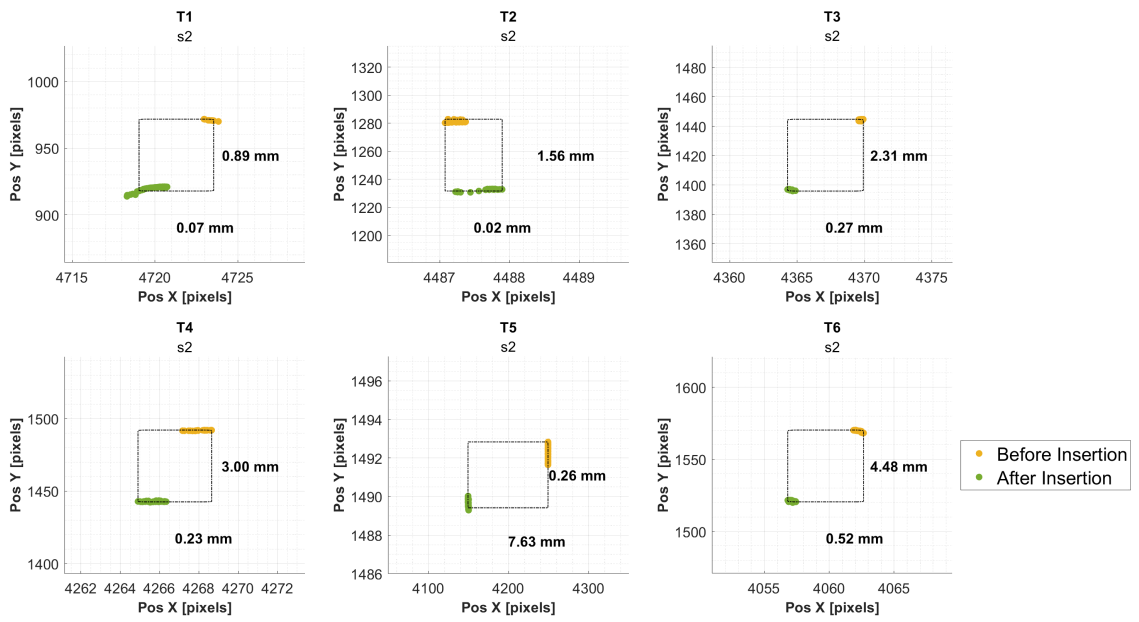
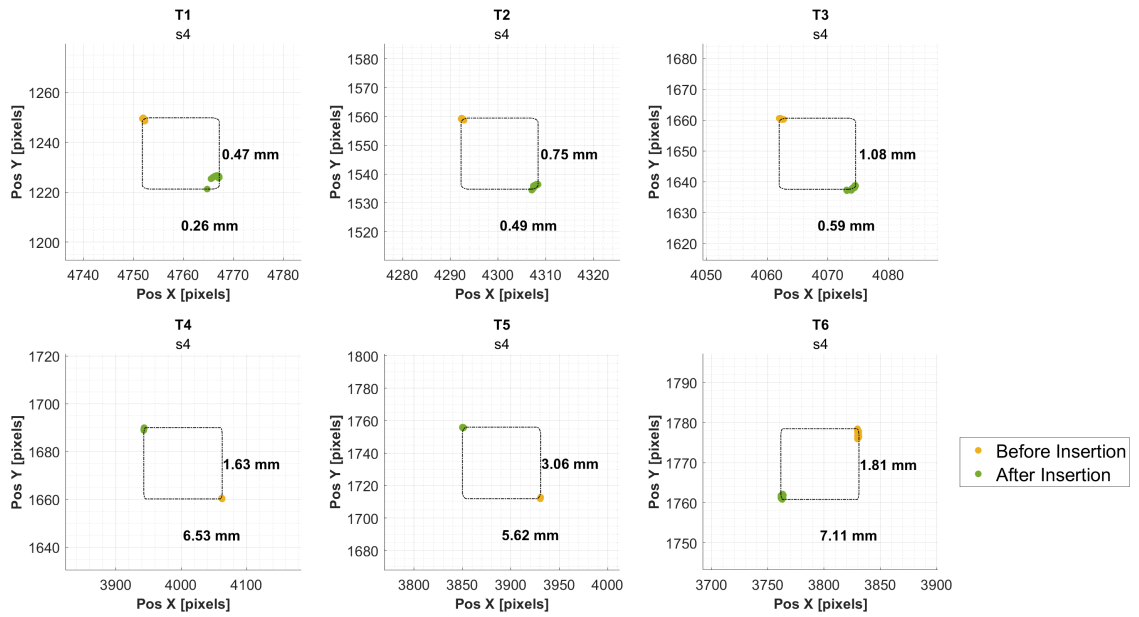


Figure C.1: Insertion: displacement of T1-T6 BCAM2.

## C. pHB650 Data Acquisition



**Figure C.2: Insertion: displacement of T1-T6 BCAM3.**



**Figure C.3: Insertion: displacement of T1-T6 BCAM4.**

## C.2 Transport

### UP-DS BCAM2-BCAM4

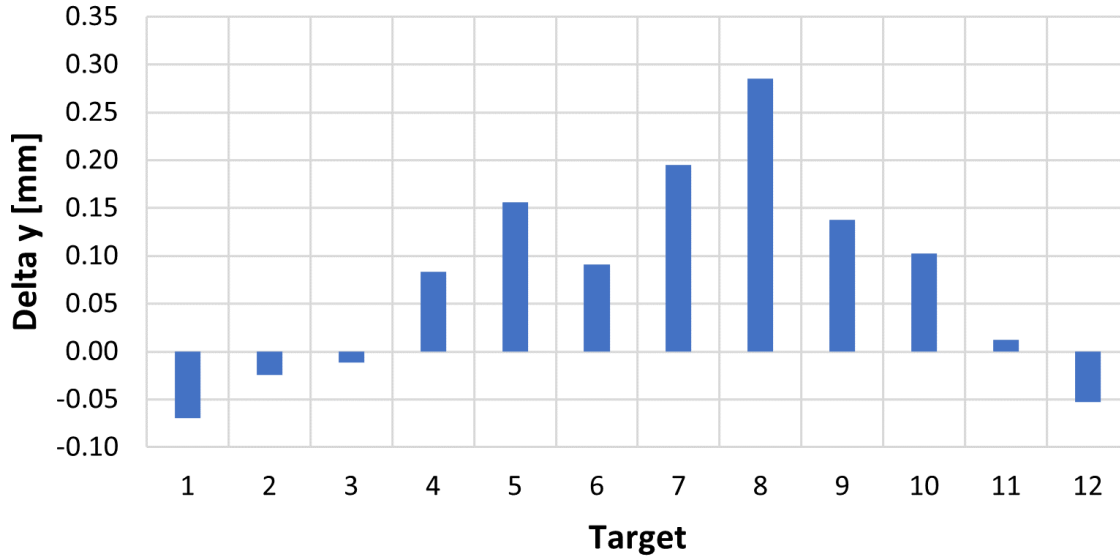


Figure C.4: Transport: corrected vertical displacements.

### UP-DS BCAM2-BCAM4

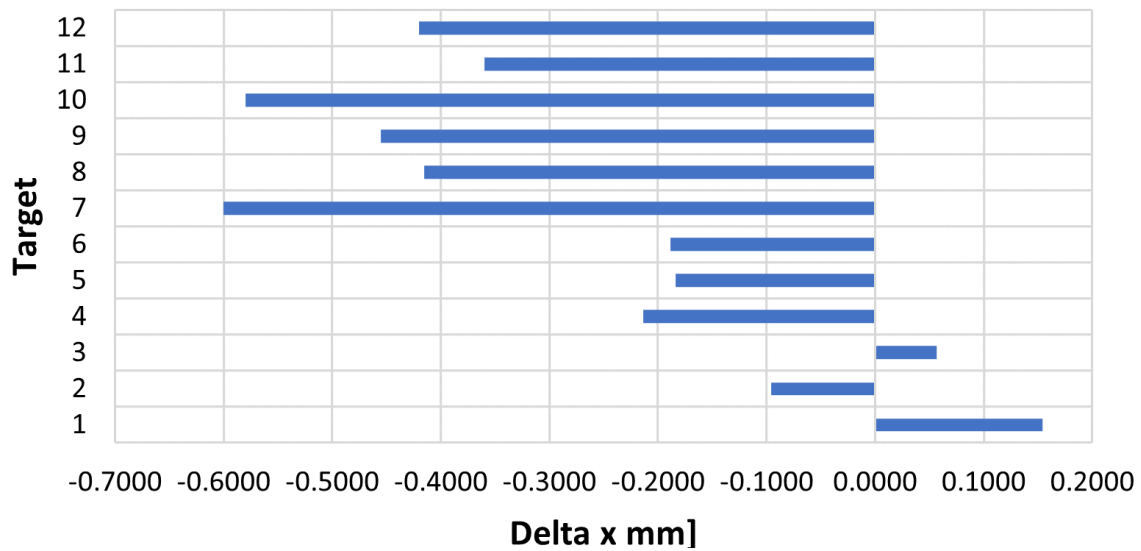


Figure C.5: Transport: corrected horizontal displacements.

### C.3 Pump-Down

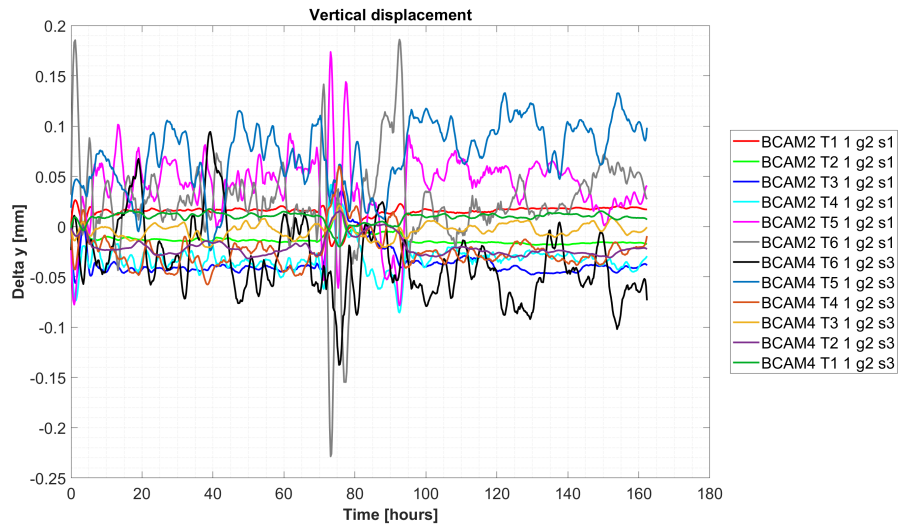


Figure C.6: Pump-down: corrected vertical displacements, from BCAM2 to BCAM4.

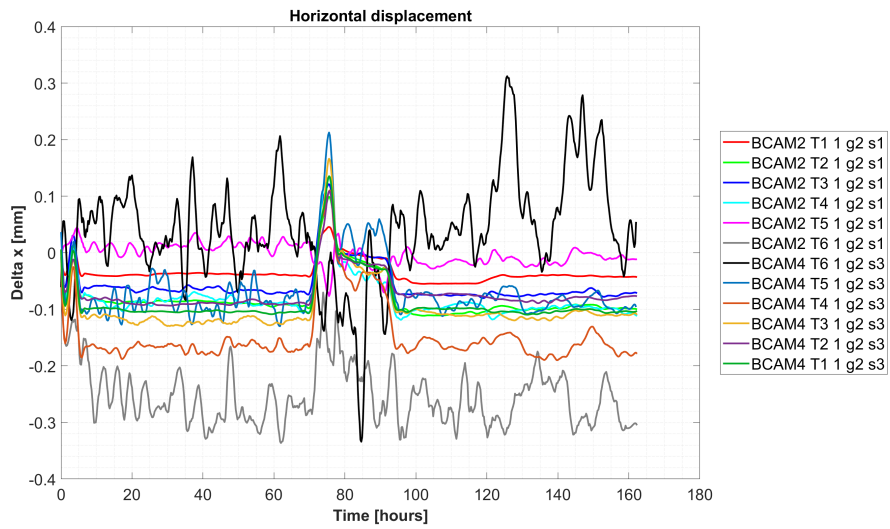


Figure C.7: Pump-down: horizontal displacements, from BCAM2 to BCAM4.

## C.4 Cooldown

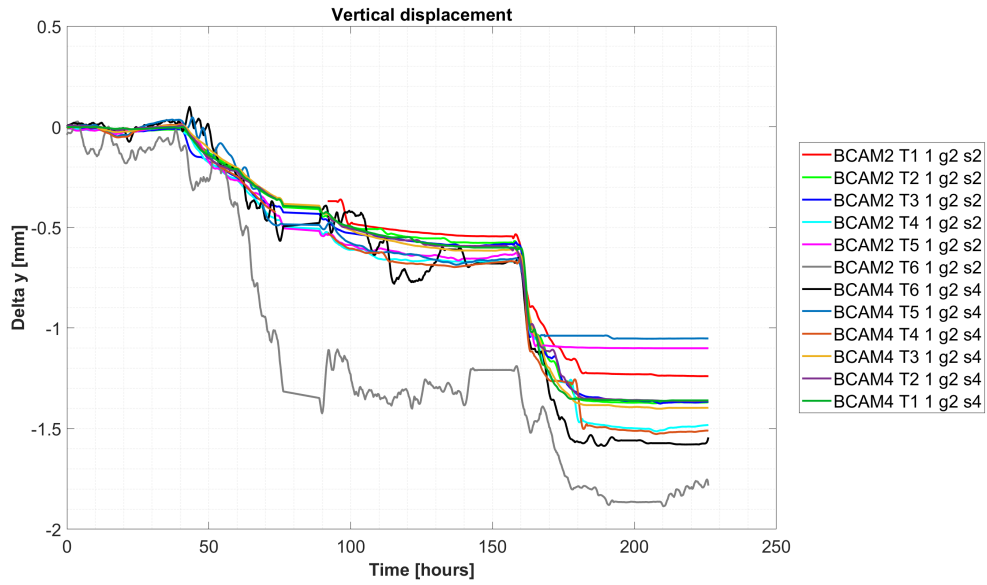


Figure C.8: Cooldown: vertical displacements, from BCAM2 to BCAM4.

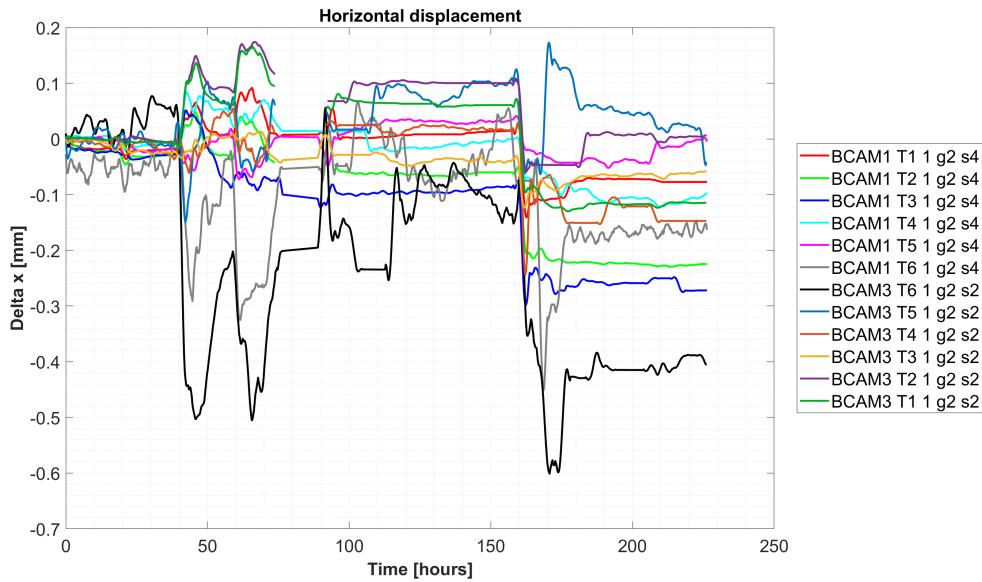


Figure C.9: Cooldown: horizontal displacements, from BCAM1 to BCAM3.

*Table C.1: Numerical results of the cooldown test.*

	<b>BCAM1-BCAM3</b>		<b>BCAM2-BCAM4</b>	
	<b>Vertical [mm]</b>	<b>Horizontal [mm]</b>	<b>Vertical [mm]</b>	<b>Horizontal [mm]</b>
<b>T1</b>	$-1.292 \pm 0.001$	$-0.072 \pm 0.001$	$-1.275 \pm 0.001$	$-0.439 \pm 0.001$
<b>T2</b>	$-1.441 \pm 0.001$	$-0.224 \pm 0.001$	$-1.364 \pm 0.001$	$-0.579 \pm 0.001$
<b>T3</b>	$-1.361 \pm 0.002$	$-0.220 \pm 0.002$	$-1.311 \pm 0.002$	$-0.600 \pm 0.003$
<b>T4</b>	$-1.389 \pm 0.003$	$-0.171 \pm 0.004$	$-1.450 \pm 0.002$	$-0.426 \pm 0.004$
<b>T5</b>	$-1.444 \pm 0.007$	$-0.008 \pm 0.003$	$-1.272 \pm 0.006$	$-0.381 \pm 0.016$
<b>T6</b>	$-1.633 \pm 0.094$	$-0.102 \pm 0.060$	$-1.464 \pm 0.091$	$-0.480 \pm 0.100$
<b>T7</b>	$-1.251 \pm 0.023$	$-0.128 \pm 0.026$	$-1.484 \pm 0.117$	$-0.378 \pm 0.102$
<b>T8</b>	$-1.867 \pm 0.021$	$-0.207 \pm 0.018$	$-1.205 \pm 0.013$	$-0.548 \pm 0.007$
<b>T9</b>	$-1.563 \pm 0.006$	$-0.038 \pm 0.004$	$-1.475 \pm 0.002$	$-0.412 \pm 0.003$
<b>T10</b>	$-1.464 \pm 0.002$	$-0.069 \pm 0.002$	$-1.418 \pm 0.002$	$-0.395 \pm 0.002$
<b>T11</b>	$-1.413 \pm 0.001$	$-0.008 \pm 0.001$	$-1.319 \pm 0.001$	$-0.385 \pm 0.001$
<b>T12</b>	$-1.339 \pm 0.001$	$-0.133 \pm 0.001$	$-1.368 \pm 0.001$	$-0.456 \pm 0.001$



---

# Bibliography

- [1] J. Bernardini, D. Passarelli, S. Zorzetti, *Computer vision techniques used to monitor the alignment of cavities and solenoids in the PIP-II prototype SSR1 cryomodule*, Proceedings of IPAC2021, Campinas, Brazil, 2021, THXX02.
- [2] S. Cheban, D. Passarelli, S. Zorzetti, *Alignment monitor system for the PIP-II cryomodules*, Proceedings of SRF2019, Dresden, Germany, 2019, MOP102.
- [3] A. Sukhanov et al., *STC qualification tests of PIP-II HB650 cavities*, Proceedings of SRF2021, East Lansing, MI, USA, 2022.
- [4] D. Passarelli et al., *SSR1 tuner mechanism: passive and active device*, Proceedings of LINAC2014, Geneva, Switzerland, 2014, TUPP052.
- [5] M. Parise, D. Passarelli et al., *Mechanical design and fabrication aspects of prototype SSR2 jacketed cavities*, Proceedings of SRF2019, Dresden, Germany, 2019.
- [6] P. Berrutti et al., *New design of SSR2 spoke cavity for PIP-II SRF linac*, Proceedings of SRF2019, Dresden, Germany, 2019, pp. 600–604.
- [7] M. Parise et al., *Fabrication experience of the pre-production PIP-II SSR2 cavities at Fermilab*, presented at LINAC2022, TUPOGE17, Liverpool, United Kingdom, Aug-Sep. 2022.
- [8] J. Bernardini et al., *Final design of the pre-production SSR2 cryomodule for PIP-II project at Fermilab*, action SSR2 cryomodule for PIP-II project at Fermilab”, presented at LINAC’22, Liverpool, UK, Aug.-Sep. 2022, paper TUPOGE12.
- [9] V. Roger et al., *Design of the 650 MHz high beta prototype cryomodule for PIP-II at Fermilab*, presented at the SRF’21, East Lansing, MI, USA, Jun.-Jul. 2021, paper WEPTEV015, unpublished.
- [10] V. Roger et al., *Design strategy of the PIP-II cryomodules*, Proceedings of SRF2019, Dresden, Germany, 2019, MOP094.

### *C. Bibliography*

---

- [11] V.Lebedev, *The PIP-II Reference Design Report*, United States: N. p., 2015. Web.  
doi:10.2172/1365571.
- [12] Fermilab, Proton Improvement Plan-II.  
<https://pip2.fnal.gov>
- [13] Open Source Instruments, H-BCAM.  
<https://www.opensourceinstruments.com/HBCAM>